INFORMATION TO USERS

DETAILED STUDY OF THE YARKOVSKY EFFECT ON ASTEROIDS AND
SOLAR SYSTEM IMPLICATIONS

by

Joseph Nicholas Spitale

_____

UMI Number: 3026568

UMI®

THE UNIVERSITY OF ARIZONA ®
GRADUATE COLLEGE

As members of the Final Examination Committee, we certify that we have

read the dissertation prepared by Joseph Nicholas Spitale

entitled Detailed study of the Yarkovsky effect and solar system

implications

_____

_____

_____

and recommend that it be accepted as fulfilling the dissertation

requirement for the Degree of Doctor of Philosophy

Richard Greenberg	8/17/01 Date
Jay Melosh	8/17/01 Date
William Hubbard	8/17/01 Date
Carolyn Porco	8/17/01 Date
Alex Dessler	8/17/01 Date

Final approval and acceptance of this dissertation is contingent upon
the candidate's submission of the final copy of the dissertation to the
Graduate College.

I hereby certify that I have read this dissertation prepared under my
direction and recommend that it be accepted as fulfilling the dissertation
requirement.

_____   Sept. 10, 2001
Dissertation Director   Richard Greenberg   Date
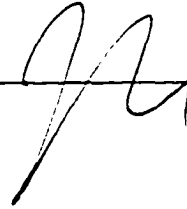
STATEMENT BY AUTHOR

This dissertation has been submitted in partial fulfillment of requirements for an advanced degree at The University of Arizona and is deposited in the University Library to be made available to borrowers under rules of the library.

Brief quotations from this dissertation are allowable without special permission, provided that accurate acknowledgment of source is made. Requests for permission for extended quotation from or reproduction of this manuscript in whole or in part may be granted by the head of the major department or the Dean of the Graduate College when in his or her judgment the proposed use of the material is in the interests of scholarship. In all other instances, however, permission must be obtained from the author.

SIGNED:

ACKNOWLEDGEMENTS

DEDICATION

To "cracker." You died quietly sometime over the weekend.

TABLE OF CONTENTS

ABSTRACT

The Yarkovsky effect is a change in a body's orbit caused by its reaction to the momentum carried away by the thermal photons that it emits. This effect may play a key role in the orbital evolution of asteroids and near-Earth objects. To evaluate the Yarkovsky acceleration under a wide range of conditions, I have developed a three-dimensional finite-difference solution to the heat equation. This approach employs neither the linearized boundary conditions. the plane-parallel heat flow approximation, nor the assumption of fast rotation used in earlier approaches (Rubincam, 1998; Vokrouhlický and Farinella. 1998). Thus it can be used to explore a wide range of orbital elements and physical properties that had not been previously accessible.

I use the finite-difference approach to compute Yarkovsky perturbations for homogeneous, spherical stony bodies with 1-, 10- and 100-m diameters. For a 1-m scale body rotating with a 5-h period, the semimajor axis can change as much as 1 AU in 1 Myr and the eccentricity can change as much as 0.1 in 1 Myr. These rates are much faster than any found previously because those treatments were not valid for very eccentric orbits. For rotation periods expected to be more typical of such small bodies, these rates would be considerably slower. Nevertheless, there is no data concerning rotation rates for small bodies so these fast rates may be relevant.

Yarkovsky drift rates are computed for models of specific near-Earth asteroids, demonstrating that the shape of a body is important in computing its precise Yarkovsky effect. Such calculations may be useful for assessing observable Yarkovsky perturbations and in predicting and mitigating NEA hazards. The approach presented in this dissertation is the only current one with the potential to rigorously treat bodies with arbitrary shapes.

CHAPTER 1

INTRODUCTION

1.1   The original Yarkovsky effect

The Yarkovsky effect is a change in a body's orbit caused by its reaction to the momentum carried away by the thermal photons that it emits. Little is known about its originator, but Öpik (1951) recalled imprecisely a paper (from around 1909) written by a Polish civil engineer named Yarkovsky, published in Russian around the turn of the century. No other explicit reference to this work is known and the paper itself was apparently lost.

(a)   (b)
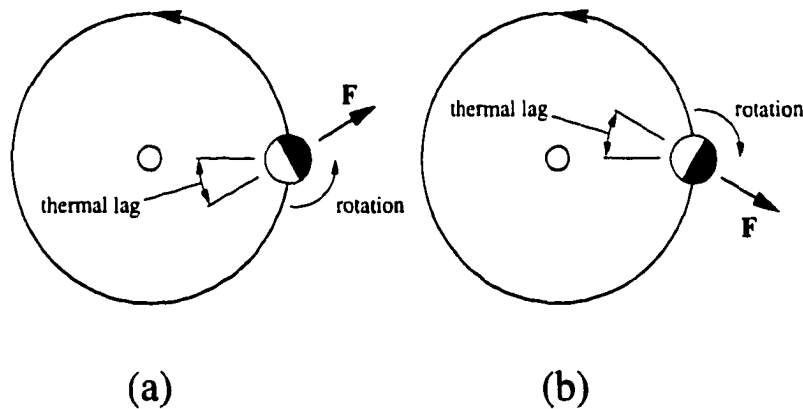
Figure 1.1: A body on a circular orbit with its rotation axis normal to the orbital plane. (a) for prograde rotation, the transverse force component is in the same direction as the orbital motion, causing the semimajor axis to increase. (b) for retrograde rotation, the transverse force component is directed opposite to the direction of orbital motion, resulting in semimajor axis decay.

To understand how the effect proposed by Yarkovsky works, consider a body

on a circular orbit with its rotation axis normal to the orbital plane (Fig. 1.1). Each photon emitted by an element of the body's surface carries with it an amount of momentum that depends on the temperature of that surface element. Therefore. hotter surface elements receive larger impulses and cooler surface elements receive smaller impulses. Integrated over the surface of the body, these thermal impulses produce a net force on the body whose magnitude and direction depend on the body's surface temperature distribution. Because of thermal inertia, this surface temperature distribution lags the heating. In other words, the hottest part of the day occurs during the afternoon instead of exactly at noon. Therefore, the net Yarkovsky force contains a component that is directed parallel to the orbital motion. For prograde rotation (Fig. 1.1a), this transverse force component is in the direction of the orbital motion, causing the orbital semimajor axis a to increase. Conversely. for retrograde rotation (Fig. 1.1b), a decreases. For a slightly eccentric orbit. the eccentricity e also increases for prograde rotation and decreases for retrograde rotation, and the longitude of pericenter ϖ always regresses (Peterson, 1976). This original Yarkovsky effect is strongest when the obliquity ι is 0 or π, and is negligible when $\iota = \pi/2$. Moreover, this effect turns off when the rotation is so fast that the surface temperature distribution is smeared out with no longitudinal variation. This smearing occurs when a body rotates fast enough that the thermal pulse is unable to penetrate significantly.

1.2   The modern Yarkovsky effect

The effect that Yarkovsky originally described is known today to be the special "diurnal" case of a more general effect. While for cases with $\iota = 0$ or π, the effect consists of only Yarkovsky's original diurnal effect, for other obliquities, there is an additional forcing frequency corresponding to the orbital period of the body. Even when the rotation of the body is fast enough that the diurnal contribution is negligible, there may still be a reradiation force, caused by the north/south seasonal temperature asymmetry. This "seasonal" Yarkovsky effect has the greatest effect

on a when the rotation axis lies in the plane of the orbit ($\iota = \pi/2$), and has no effect on a when $\iota = 0$.
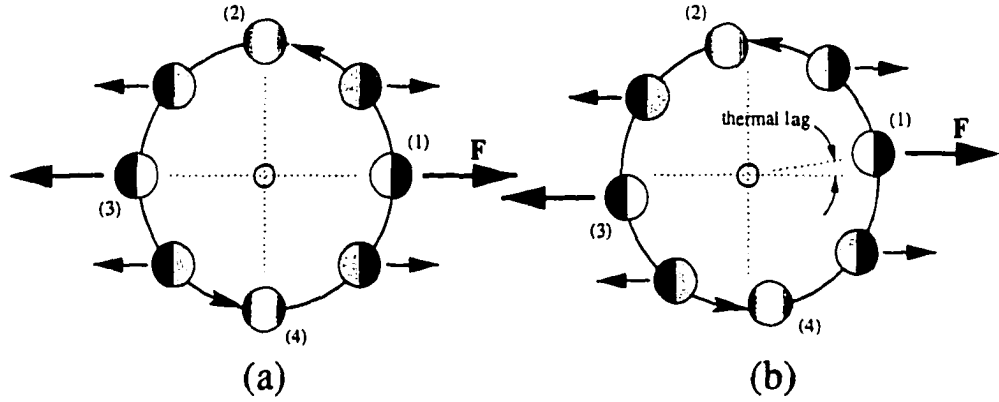
Figure 1.2: A body on a circular orbit with its rotation axis in the orbital plane. The body rotates rapidly so the net force vector is parallel to the spin axis. (a) Without the seasonal lag, the situation is symmetric so instantaneous changes in a caused by transverse force components cancel out over a complete orbit, resulting in no net change in a. (b) With seasonal lag, the symmetry is broken, causing a net semimajor axis decay.

Figure 1.2 shows the orientation of the force vector at various points in a circular orbit for a fast-rotating body with $\iota = \pi/2$. In (a) there is no seasonal lag, that is, surface temperatures respond instantaneously to the heating. At positions (1) and (3), when the rotation axis points directly toward or away from the sun, the surface temperature distribution is highly asymmetric, producing a large radial Yarkovsky force vector oriented parallel to the spin axis. At points (2) and (4), when the rotation axis is perpendicular to the radial direction, there is no surface temperature asymmetry to produce a net force vector. There are two quadrants of the orbit (2-3 and 4-1) in which the transverse force component is in the same direction as the orbital motion (producing an instantaneous increase in a) and two quadrants (1-2 and 3-4) where the transverse force component is directed opposite to the orbital motion (producing an instantaneous decrease in a). With no thermal inertia, the situation is completely symmetric so the instantaneous changes in a

cancel out over an orbit, resulting in no net change.

In Fig. 1.2b, the seasonal lag causes each thermal state to occur a bit later in the orbit. Again, there are two quadrants of the orbit (2-3 and 4-1) in which the transverse force produces an instantaneous increase in a and two quadrants (1-2 and 3-4) where the transverse force produces an instantaneous decrease in a. In this case, however, the largest impulses occur in quadrants 1-2 and 3-4, where the transverse force produces an instantaneous decrease in a. Averaged over an orbit, the forces that increase a do not completely cancel the forces that decrease a, so there is a net decay of the semimajor axis. For this purely "seasonal" (fast rotation) case, Rubincam (1995) showed that, for nearly circular orbits, the rate of semimajor axis decay does not depend on e. He also found that e always decreases and that the orientation of the semimajor axis, ϖ, always regresses. Orbits with larger eccentricities were beyond the scope and validity of Rubincam's approach.

For bodies on nearly circular orbits, the total Yarkovsky effect is usually well approximated by a linear combination of independent seasonal and diurnal effects. Such cases may be treated using a linear theory like the one derived in Chapter 3. However, for less ideal cases, the linear theory is inadequate and a more general theory is required.

1.3   Strength of the Yarkovsky effect

For an estimate of the maximum possible change in semimajor axis (equivalent to a change in orbital energy), consider a body of radius R on a circular orbit of semimajor axis a. If we consider radiation from the hot hemisphere and neglect radiation from the cold hemisphere and assume that it is directed so as to produce the maximum da/dt, then we can obtain an upper bound to the semimajor axis mobility. During a time interval Δt, the hot side radiates an energy of order $\pi R^2 \sigma T^4 \Delta t$, where σ is the Stefan-Boltzmann constant and T is the effective temperature, i.e.,

the equilibrium temperature of a spherical blackbody with infinite thermal conductivity. The orbital energy is $(-\mu/2a)m$, where μ is the gravitational constant times the mass of the sun, $m = \frac{4}{3}\pi R^3 \rho$ is the mass of the body, and ρ is the density of the body. Writing for the effective temperature, $T^4 = L_\odot/16\pi a^2 \sigma$, where $L_\odot$ is the solar luminosity, we obtain an estimate for the maximum rate of semimajor axis change:

$$\frac{\Delta a}{\Delta t} \leq \frac{1}{32}\frac{L_\odot}{\mu\rho R}. \tag{1.1}$$

For a body of radius 1 m and density 3000 kg m^{-3}, (1.1) yields a semimajor axis change as great as 0.1 AU in one year. In reality, such bodies typically rotate fairly rapidly and radiate in many directions, so this simplified calculation greatly overestimates the mobility. Nevertheless, this calculation suggests that the Yarkovsky effect warrants further study.

Expression (1.1) for an upper limit on the Yarkovsky effect does not depend on the semimajor axis. However, the Yarkovsky effect itself must eventually become unimportant as a becomes large. The net Yarkovsky force depends on the temperature difference between the day side and night side, which should decrease with increasing semimajor axis. To understand why this must be so, consider the internal transport of heat within the body. In equilibrium, the internal temperature gradient of the body (basically, the temperature difference across the body) is that which is sufficient to transport the net incoming energy from the day side to the night side where it is radiated back to space. Near the sun, a relatively large amount of energy enters the day side and must be transported to the night side, requiring a steep gradient and thus a large temperature difference. Further from the sun, less energy enters on the day side, so a smaller temperature difference is adequate to transport the heat. Thus, (1.1) becomes a less useful upper bound because it was based on the assumption that radiation from the night side could be neglected.

Expression (1.1) correctly demonstrates that the Yarkovsky effect should become small as the size of the body grows, causing the Yarkovsky effect to be unimportant for planetary-scale bodies. However, because it is an upper limit, one

cannot infer from (1.1) that the Yarkovsky effect should be strong for very small bodies. Again, the problem arises from the assumption that radiation from the cold side can be neglected. In this case, that assumption breaks down when the radius is small enough that the body is nearly isothermal, with very little day-night temperature difference, as discussed below.

For a better estimate of the correct dependence of da/dt on a and R, consider the body of radius R synchronously rotating on a circular orbit of semimajor axis a. In steady state, some of the heat that enters the body on the day side is re-emitted on the day side and some flows down a temperature gradient to the night side, being re-emitted in the other direction. Therefore, we can write

$$
\begin{aligned}
S_\odot &= \sigma T_d^4 + k\nabla T \\
\sigma T_n^4 &= k\nabla T,
\end{aligned}
\tag{1.2}
$$

where T_d and T_n are the day- and night-side temperatures respectively, $S_\odot$ is the incident solar energy per unit area and k is the thermal conductivity. In this simple discussion, we can assume that the temperature gradient ∇T is constant throughout the body, being roughly $\nabla T \sim (T_d - T_n)/2R$. Defining $\Delta T \equiv (T_d - T_n)/2$, expressions (1.2) may be combined to yield

$$
S_\odot = \sigma(T_d^4 - T_n^4) + \frac{k}{R}\Delta T.
\tag{1.3}
$$

Writing $T_d = T_0 + \Delta T$ and $T_n = T_0 - \Delta T$, where T_0 is the central temperature, multiplying out T_d^4 and T_n^4, and neglecting terms of order $(\Delta T)^2$ and higher, we have $T_d^4 - T_n^4 \sim 6T_0^3\Delta T$. Substituting into (1.3) and rearranging, we find

$$
\Delta T \sim \frac{S_\odot}{6\sigma T_0^3 + \frac{k}{R}}.
\tag{1.4}
$$

For large bodies (i.e., $R \gg 6\sigma T_0^3/k$), the temperature difference (1.4) simplifies to $S_\odot/6\sigma T_0^3$. Because $S_\odot = L_\odot/4\pi a^2$ and $T_0^3 = (L_\odot/16\pi a^2)^{3/4}$, ΔT varies as $a^{-1/2}$ in this limit. For small bodies (i.e., $R \ll 6\sigma T_0^3/k$), ΔT simplifies to $S_\odot R/k$, which has a semimajor axis dependence of a^{-2}. Therefore, as explained above, day-night temperature difference, and hence Yarkovsky da/dt, decrease with increasing a.

Also for small bodies, it can be seen that ΔT becomes small as R becomes small. Assuming $k = 2.4$ W m^{-1} K^{-1} and $T_0 = 270$ K, we obtain $6\sigma T_0^3/k \sim 3$ m, so bodies of order centimeters or smaller are indeed nearly isothermal and experience essentially no Yarkovsky effect.

Such small, nearly isothermal bodies are instead influenced by the well-known Poynting-Robertson effect. This effect, which is important only for cm-scale and smaller bodies, produces a net force opposite to the direction of motion caused by the difference in momentum between the blue-shifted forward-emitted photons and the red-shifted backward-emitted photons. Because the Yarkovsky and Poynting-Robertson effects are never significant simultaneously for a given particle, the Poynting-Robertson effect will be neglected in the remainder of this dissertation.

How does the strength of the Yarkovsky effect compare to non-radiative perturbations experienced by asteroids? First, consider the drag experienced by a main-belt asteroid caused by collisions with smaller particles. The drag force F_d on a body of radius R and mass m can be roughly thought of as the amount of momentum swept up by the body per unit time:

$$F_d \simeq \dot{M} \langle v \rangle, \tag{1.5}$$

where $\langle v \rangle$ is the mean dispersion velocity – roughly 5 km/s in the main belt – and $\dot{M}$ is the mass swept up by the body per unit time. Because the body sweeps through a volume $\pi R^2 \langle v \rangle$ in unit time, we can write

$$\dot{M} = \pi R^2 \langle v \rangle \int_0^R \frac{4}{3}\pi r^3 \rho n(r)dr, \tag{1.6}$$

where $n(r)$ is the number of bodies per unit volume with radius between r and $r + dr$ and ρ is the density of each particle. The acceleration f is then

$$f = \frac{F}{m} = \pi \frac{\langle v \rangle^2}{R} \int_0^R r^3 n(r)dr, \tag{1.7}$$

assuming the asteroid in question also has density ρ. Writing

$$n(r) = -\frac{1}{V}\frac{dN}{dr}, \tag{1.8}$$

where

$$N(r) = 3.5 \times 10^5 \left(\frac{r}{1km}\right) \tag{1.9}$$

is the number of main-belt particles with radius larger than r (Farinella et al.. 1994) and V is the volume of the main belt, the integral in (1.7) can be evaluated. Assuming that the main belt extends from $a = 2$ AU to $a = 3$ AU with an inclination dispersion of about 0.1, the acceleration due to particle drag (1.7) becomes

$$f \sim 2.5 \times 10^{-13} \text{ m s}^{-2} \left(\frac{1\text{m}}{R}\right)^{1/2}. \tag{1.10}$$

The semimajor axis change caused by this drag is

$$\left.\frac{da}{dt}\right|_{\text{drag}} \simeq \frac{2f}{n}, \tag{1.11}$$

where n is the mean motion. For a body with $a = 2.5$ AU, we find

$$\left.\frac{da}{dt}\right|_{\text{drag}} \simeq 5 \times 10^{-4} \text{ AU Myr}^{-1} \left(\frac{1\text{m}}{R}\right)^{1/2}. \tag{1.12}$$

Such semimajor axis rates are much slower than the upper bound for the Yarkovsky semimajor mobility (1.1) estimated above. Indeed, even compared to the more realistic Yarkovsky rates computed later in this dissertation, semimajor axis change caused by particle drag, as given by (1.12), is not significant. However. because for large bodies, the Yarkovsky effect varies as R^{-1} while particle drag varies as $R^{-1/2}$. particle drag could dominate over the Yarkovsky effect for large enough bodies. For example, based on the weakest Yarkovsky semimajor axis rates computed in Chapter 5, bodies with radii larger than about 40 km might experience larger drag perturbations than Yarkovsky perturbations. For bodies that large, however, those perturbations are negligible.

Particle drag should also dominate for small enough bodies, because the Yarkovsky effect becomes unimportant for those sizes as well. However. for bodies that small, the Yarkovsky effect is swamped by the Poynting Robertson effect. Therefore, while particle drag may be stronger than the Yarkovsky effect for certain

size ranges, it can be neglected for bodies larger than a few centimeters and smaller than tens of kilometers.

Next, consider gravitational perturbations. A meter-scale body with $a = 2.5$ AU would feel instantaneous accelerations from Jupiter of order 10^{-6} m s^{-2}, whereas the strongest instantaneous Yarkovsky accelerations from chapter 5 are smaller than 10^{-9} m s^{-2}. Nevertheless, for nonresonant orbits, those gravitational perturbations have little long term effect while Yarkovsky semimajor axis perturbations accumulate secularly, producing large effects over long timescales. For resonant orbits however, eccentricities may be enhanced so rapidly that bodies may be removed from the solar system in a few Myr (see Chapter 2). In those cases, the Yarkovsky effect is not important unless it can cause a body to traverse the resonance before it can be removed removed from the solar system, as discussed in chapter 10.

Since Öpik's rediscovery of the Yarkovsky effect, it has been studied by many authors (Radzievskii, 1952; Peterson, 1976; Rubincam, 1995; Rubincam, 1998; Vokrouhlický and Farinella, 1998; Vokrouhlický and Farinella, 1999; Vokrouhlický and Brož, 1999; Farinella et al., 1998; Farinella and Vokrouhlický, 1999). However, due to the various approximations employed by each author, the parameter space accessible to those methods is limited, and the Yarkovsky effect has yet to be thoroughly characterized. Peterson (1976) used a Fourier expansion truncated at 4th order to explore the diurnal Yarkovsky effect. Rubincam (1987) identified the seasonal Yarkovsky effect and studied it by linearizing the radiative boundary condition such that his results are only valid for small eccentricities (Rubincam, 1995; Rubincam, 1998). Vokrouhlický and Farinella (1998) have developed a nonlinearized treatment of the seasonal effect, but it is only valid for large bodies (because of a plane-parallel heat-flow approximation). Vokrouhlický and Farinella (1999) expand their treatment to include smaller bodies, but their approach is still impractical for fairly large eccentricities. In addition, other effects that might be important in

determining the surface temperature distribution have not been fully addressed in previous work. These effects include insulation by regoliths (recently modeled by Vokrouhlický and Brož (1999) for circular orbits), nonspherical shapes (addressed for large ellipsoidal bodies in Vokrouhlický and Farinella (1998)), fractures in the rock, the temperature dependence of thermal conductivity and heat capacity, and the mixing of the diurnal and seasonal effects in the true nonlinear problem.

In order to address the above problems and to obtain more general solutions, I have developed a three-dimensional finite-difference calculation that solves the heat equation throughout an orbiting body with solar insolation boundary conditions. For a given set of fixed orbital elements, perturbations to the elements are computed by numerically averaging Gauss' perturbation equations over a single orbit. This calculation addresses the full nonlinear problem. It is valid, in principle, for any set of orbital elements and for any spin state. It can treat bodies with realistic physical structures and properties. Currently, this approach can treat ellipsoidal bodies, and it could be easily adapted to bodies with arbitrary shapes.

In this dissertation, I use my numerical approach to compute changes in orbital elements caused by the *general* Yarkovsky effect, by which I mean any case that is neither purely seasonal nor purely diurnal, for conditions under which the Yarkovsky effect has never before been studied.

CHAPTER 2

BACKGROUND

2.1 Delivery scenarios

One reason for studying the Yarkovsky effect on asteroids is that a number of discrepancies in models regarding the delivery of asteroidal material from main-belt orbits to the surface of the Earth may potentially be resolved by properly incorporating it.

The first step toward establishing a link between meteorites and asteroids was taken by Ernst Chladni, who proposed over 200 years ago that meteorites originate beyond the Earth's atmosphere. This idea implies a population of bodies whose orbits cross those of the inner planets. Such a population was eventually revealed by telescopic observations, but bodies on such orbits are subject to perturbations by and collisions with the terrestrial planets, as well as disruption by main-belt projectiles (if their aphelion takes them that far) so their lifetimes are less than 10 Myr (Gladman et al., 1997), short compared to the 4.5 Gyr age of the solar system. Therefore these bodies cannot have formed in such orbits; there must be a source of continuous replenishment.

The main asteroid belt is a likely source of inner-planet crossers, but a number of other small-body reservoirs are known to exist in the solar system. The Trojan asteroids with orbits similar to that of Jupiter, the Kuiper belt beyond the orbit of Neptune, and the distant Oort cloud may all supply small bodies to the inner solar system. However these sources can be ruled out as major contributers to the population of inner-planet crossers, both because of their greater distance

from the inner solar system compared to the main belt, and because bodies from these sources would be strongly influenced by the giant planets, causing them to have cometary orbits (orbits with very high eccentricities and large aphelion distances) by the time they become terrestrial-planet-crossers. Such orbits have short dynamical lifetimes (shorter than 1 Myr) (Levison and Duncan, 1994; Morbidelli, 1997). Therefore, most inner-planet crossers probably originated in the main belt and somehow evolved onto their current orbits.

In 1866, Kirkwood noticed that the asteroid belt contains a number of gaps, that is, regions in orbital-element space that appear to be depleted in asteroids. These Kirkwood gaps are roughly centered around semimajor axes that correspond to the 3:1, 5:2, and 2:1 mean-motion commensurabilities with Jupiter. Furthermore, the upper boundary of the asteroid belt in the semimajor axis vs. orbital inclination plane is relatively sharp and corresponds to the ν_6 secular resonance with Saturn. It was suggested that some resonant mechanism associated with these commensurabilities removes asteroids whose orbital elements are just right and places them on orbits that intersect those of the inner planets.

2.1.1 The classical delivery scenario

Speculation concerning the connection between strong main-belt resonances and planet-crossing asteroids was impossible to justify quantitatively until the development of an analytical theory of secular perturbations on asteroids by Williams (1969). Williams showed that, in the vicinity of the ν_6 resonance, orbital eccentricity is forced to oscillate with amplitudes large enough that a body can cross the orbit of Mars at the peak of the oscillation. Wisdom (1982) showed that chaotic dynamics in the vicinity of the 3:1 resonance could cause similar eccentricity oscillations at roughly constant a. Subsequent studies confirmed that these strong main-belt resonances can enhance eccentricities to even Earth-crossing values in a few million years. This improved understanding of resonances led to the "classical" delivery

scenario. According to the classical scenario, a main-belt disruption event can impart a fragment with a velocity as much as 100 m/s relative to that of the parent body, allowing some material to be directly injected into the ν_6 or 3:1 resonances, if the parent body was close enough to begin with. This assumption is supported by the observation that a number of asteroid families, which are presumably remnants of past disruption events, are seen near the boundaries of those resonances and the dispersion in the orbital elements of the family members is consistent with Δv's of about 100 m/s. Fragments injected into the resonances would have their eccentricities pumped to Mars- or Earth-crossing values within a few Myr. It was shown (Meninchella et al., 1996) that the collision frequency in the main belt was high enough to account for the observed numbers of NEAs and meteoroids. Once a body's orbit crosses that of Mars or Earth, its eccentricity and semimajor axis can be rapidly changed by a close encounter with one of those planets, with the possibility of removing the body from the resonance. If the body is removed as a Mars-crosser, further close encounters with Mars could cause its semimajor axis and eccentricity to change stochastically until it becomes an Earth-crosser on timescales of about 100 Myr. If it is removed from the resonance while it is an Earth-crosser, it could become a Venus- or Jupiter-crosser in 1 to 10 Myr. Jupiter-crossers are likely to be ejected from the Solar system quickly while Venus-crossers diffuse throughout the inner solar system through close encounters with Earth and Venus, eventually to be removed by a collision with a planet. Median lifetimes for bodies delivered to the Earth through this classical mechanism were predicted to be a few tens of Myr (Arnold, 1965; Wetherill, 1988).

2.1.2 Problems with the classical delivery scenario

The classical scenario fails to explain the discrepancy between cosmic ray exposure ages of stony and metallic meteorites. Stony bodies record on average a few tens of millions of years of cosmic ray exposure while irons tend to record hundreds of millions of years. Because cosmic rays penetrate only about 1 m into a body,

that observation implies that iron material must on average spend about 10 times longer than stony material within about 1 m of the surface of a body before being collected on Earth. The collisional lifetime of meter-scale stony bodies is much shorter than that of similar metallic bodies, but longer than the typical resonance transfer time. Therefore, if, upon being liberated from a large body, meter-scale material is injected directly into the strong main-belt resonances, then stones and irons should show similar exposure ages. Because this is not observed, asteroids must spend much of their collisional lifetime in non-resonant main-belt orbits before entering the classical escape routes. This conclusion contradicts the classical view, which assumes that material is injected directly into the strong resonances at the time that it is liberated and begins to accumulate cosmic ray exposure.

The classical scenario also does not adequately explain why most main-belt asteroids are C (spectrally similar to carbonaceous chondrites) types while most meteorites are ordinary chondrites, although it has been argued that the carbonaceous chondrites are more susceptible to disruption upon impact or atmospheric entry and so are less likely to be found on the Earth's surface (Greenberg and Chapman, 1983).

More recently, Farinella et al. (1994) showed that asteroids starting in ν_6, 3:1, and 5:2 resonances would have their eccentricities enhanced so quickly that most would be removed by impacting the sun or encountering Jupiter on timescales of a few Myr. Also, laboratory and numerical studies of disruption events (Asphaug, 1997) yield much lower ejection velocities than assumed in the classical scenario, making it much more difficult to deliver material directly into the strong main-belt resonances. Finally, the dynamics of resonances has been found to be more complicated than had been assumed, thanks to major improvements in orbital integration techniques.

2.1.3 A new method of orbital integration

A key development in orbital integration was the introduction of the mixed-variable symplectic integrator by Wisdom and Holman (1991). This method of orbital integration was based on the earlier symplectic mapping technique used by Wisdom (1982) to demonstrate the chaoticity of the 3:1 resonance. Both methods were based on a Hamiltonian (often referred to as the "surrogate" Hamiltonian) that differed slightly from the exact Hamiltonian of the problem, but which could be solved exactly at each timestep. Hence, the numerical solution remained on a given energy surface for all time (except for rounding errors), instead of drifting across energy surfaces as with non-symplectic orbital integrators. Therefore the solution remains valid (i.e.. it corresponds closely to the behavior of a particle evolving under the surrogate Hamiltonian) over long integration times. It is assumed that the symplectic solution represents plausible orbital behavior, but for chaotic problems, despite the fact that the actual Hamiltonian and the surrogate Hamiltonian are similar, the symplectic solution most likely diverges rapidly from the real solution. For a detailed discussion of symplectic integrators, see Appendix A.

The mapping technique of Wisdom (1982) is extremely fast because it explicitly includes the terms from the disturbing function that are relevant to the specific resonance or resonances that one is interested in. In other words, that approach is problem-specific, not general. The mixed-variable version of the integrator (Wisdom and Holman, 1991) is not as fast, although it is generally faster than other orbital integrators because it assumes that the solution at each timestep is nearly the same as that for a Keplerian orbit. Its primary advantage over the mapping technique is that it closely approximates the complete disturbing Hamiltonian (except for very high-frequency terms, which are assumed to average away with negligible long-term effect), so it is quite general. Because it is symplectic, it is applicable over long integration times. Using the mixed-variable symplectic integrator, it is possible to directly investigate the complete gravitational structure of the asteroid belt (and the rest of the solar system for that matter) over times as

long as the age of the solar system.

The mixed-variable symplectic integrator of Wisdom and Holman (1991) was a great step forward, but it contains a shortcoming that severely limits its usefulness in the investigation of delivery scenarios. Because it assumes that the problem is nearly a Kepler problem with the sun as the primary mass, it is not applicable in situations where the sun is not the primary perturber. In other words, the solution poorly approximates the behavior of an asteroid during a close encounter with a planet. Since planetary close encounters are central to the classical delivery scenario, the Wisdom and Holman (1991) integrator cannot, without modification, effectively be used to study asteroid delivery scenarios.

Levison and Duncan (1994) introduced an orbital integrator (actually a family of integrators) known as "SWIFT". SWIFT is based on the Wisdom and Holman (1991) method, but it accounts for close encounters. Whenever an asteroid is within the Hill sphere of a planet, its trajectory is integrated using that planet as the primary instead of the Sun. Obviously, SWIFT is only piecewise-symplectic. Every time a Hill sphere is entered or exited, the solution jumps to a slightly different energy surface. However, there is no reason to expect that its solutions do not represent plausible orbital behavior.

The greater speed and long-term accuracy of the SWIFT integrator compared to other orbital integrators (probably no more than about a factor of ten faster than, say, a Burlisch-Stoer integrator), combined with exponentially increasing computer speeds, made it possible, in the mid-nineties to contemplate thorough statistical investigations of the chaotic structure of the main asteroid belt over long timescales.

With the new orbital integration algorithms and faster computers came more problems for the classical delivery scenario. Meninchella et al. (1996) and Zappalà et al. (1998) found that direct injection into resonances cannot supply enough large NEAs to account for the observed numbers. Morbidelli and Gladman

(1998) showed that the typical time that a particle spends in a strong resonance before impacting the Earth is considerably shorter than typical chondrite cosmic ray exposure ages, so the chondrites must have acquired most of their exposure while still in the main belt after being liberated from a larger body, but prior to entering the resonance. Both of these results strongly suggest that there is a problem with the direct-injection mechanism of the classical scenario.

2.1.4 Development of a new delivery scenario

Gladman et al. (1997) confirmed and generalized the result by Farinella et al. (1994) that the strong resonances rapidly remove bodies from the solar system. Gladman showed, in fact, that Earth and Mars encounters are not efficient at removing bodies from the strong main-belt resonances. Most particles extracted from resonance by Mars encounters are quickly recaptured into a resonance. Many particles extracted by Earth or Venus quickly become Jupiter crossers and are ejected from the solar system. Others are reinjected into resonances and impact the sun. A body that obtains a semimajor axis less than 1.8 AU can survive and may ultimately impact a planet if its semimajor axis is not driven back above 1.8 AU by further close encounters with Earth and Venus. The median lifetime of particles placed initially in the 3:1, 5:2, and ν_6 resonances was about 2 Myr, with about 10% of the particles surviving longer than 10 Myr.

Moreover, Gladman et al. (1997) found that the efficiency with which the strong resonances deliver material to regions with semimajor axis $a < 1.8$ AU decreases rapidly with increasing heliocentric distance in the main belt. The secular resonance ν_6, being closest, is most efficient at providing such bodies, followed by the mean-motion resonances 3:1, 5:1, and 2:1, respectively. This result may explain why NEAs and meteorites are predominantly chondritic, even though most main-belt asteroids are C types. The C-type asteroids have mostly $a > 2.5$ AU, so they are more likely to be ejected from the solar system than to reach $a < 1.8$ AU. Most

NEAs and meteorites come from the inner part of the belt, which is dominated by S-type asteroids, which are spectrally somewhat similar to ordinary chondrites.

Migliorini et al. (1998) showed that many asteroids in the Main belt are driven towards Mars-crossing orbits as their orbital eccentricity is stochastically increased by numerous weak mean motion resonances. Once a body becomes a Mars-crosser, it typically becomes an Earth-crosser within about 20 Myr through close encounters with Mars. This mechanism qualitatively accounts for the observed numbers of large NEAs and Mars-crossing asteroids, while the meteorites likely come from the strong resonances.

The above developments do not explain how fragments can spend most of their time drifting in the main belt before being injected into resonances, as they must, according to cosmic ray exposure data. A potential solution to this problem had been known for nearly a century.

2.1.5   The role of the Yarkovsky effect

The Yarkovsky effect provides a natural means of transporting bodies to the strong main-belt resonances slowly enough that they can accumulate substantial cosmic-ray exposure on the way. After a fragment is liberated from its parent body, it undergoes a steady inward drift due to the seasonal Yarkovsky effect, accompanied by a random walk in semimajor axis caused by the diurnal Yarkovsky effect. An asteroid family evolving under the Yarkovsky effect would thus be expected to drift inward while increasing its dispersion with time. Hence, the observed dispersions in the orbital elements of asteroid family members may be much greater than their initial dispersions so initial velocities along the lines of those predicted by Asphaug (1997) may indeed be plausible.

A Yarkovsky-assisted injection scenario is also consistent with the substantially different CRE ages measured in iron meteorites versus stones (Farinella et al., 1998). Metallic bodies are much denser than stony bodies, so even if metals and

stones of a given size experienced the same Yarkovsky forces, a metallic body would experience smaller accelerations and hence a much slower Yarkovsky drift than a stony body (note the dependence on $1/\rho$ in Eq. 1.1). Moreover, the Yarkovsky force on a metallic body is generally much smaller than that on a stony body of similar size because metallic bodies have much higher thermal conductivity. Instead of remaining near the surface and causing large temperature excursions, heat is rapidly conducted into the interior of a metallic body. Temperatures on the surface of a metallic body are less extreme than on the surface of a stony body so the net Yarkovsky force is smaller. Therefore, a metallic body of a given size will evolve much more slowly under the Yarkovsky effect than a stony body of the same size, spending considerably more time accumulating cosmic rays before entering a resonance.

In addition to assisting in the injection process, results in this dissertation suggest that the Yarkovsky effect may remove certain bodies from some strong main-belt resonances once their eccentricities become large, increasing their chances of colliding with one of the inner planets.

2.2 Short-term Yarkovsky effects

Yarkovsky effect may also be important over timescales much shorter than the millions of years associated with meteorite delivery from the main belt. For example, Vokrouhlický et al. (2000) showed that, for some NEAs, the Yarkovsky effect may cause the orbital semimajor axis to evolve quickly enough that displacements could be detected over intervals of decades using radar astrometry (see Chapter 8). Therefore, the ability to compute Yarkovsky perturbations for specific asteroids may be necessary in order to generate precise asteroid ephemerides. Without such precise ephemerides, it may not be possible to take advantage of expected improvements in the precision of radar observations. Moreover, such precise knowledge of asteroid orbits and their future evolution is necessary for the assessment of NEA hazards as

far into the future as possible. Indeed, in Chapter 9, I show that the Yarkovsky effect may even be useful in mitigating such hazards.

CHAPTER 3

LINEAR THEORY OF THE YARKOVSKY EFFECT

In this chapter, I derive a formulation for Yarkovsky orbital perturbations for a simplified case. I consider a homogeneous spherical body on a circular orbit, and assume that temperature variations are small enough to treat linearly. This formulation closely resembles that of Vokrouhlický (1999). There are two reasons for reproducing such a theory here: (1) in order to display all of the intermediate steps that are not shown in that paper and (2) to supplement the qualitative discussions throughout this dissertation.
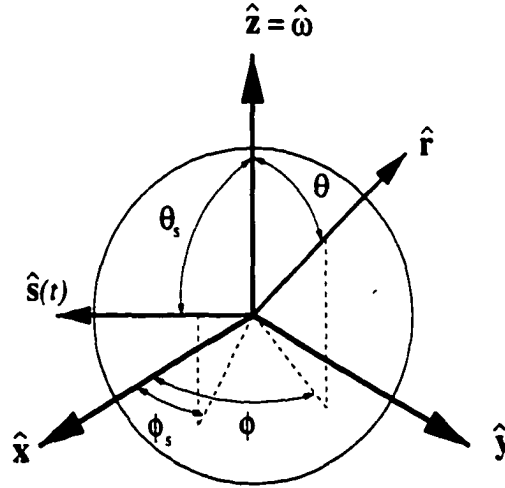
Figure 3.3: Body-fixed coordinate system used in the linearized theory. The vectors $\hat{x}$, $\hat{y}$, and $\hat{z}$ form an orthogonal coordinate system that rotates with the body about the $\hat{z}$ axis with angular speed ω. $\hat{s}(t)$ points toward the sun; its spherical coordinates in the body-fixed system are (θ_s, ϕ_s). $\hat{r}$ defines a point on the surface of the body; its spherical coordinates in the body-fixed system are (θ, ϕ).

Consider the heat diffusion equation,

$$\frac{\partial T}{\partial t} = \kappa \nabla^2 T, \qquad (3.13)$$

where $T(r, \theta, \phi, t)$ is the temperature at time t at a point in the body whose spherical coordinates are (r, θ, ϕ) (see Fig. 3.3 for the coordinate system), and κ is the thermal diffusivity, which is assumed in this case to be uniform throughout the body. A boundary condition for this equation can be found at the surface of the body. There, incident sunlight is balanced by thermal radiation and conduction into the interior:

$$k \left. \frac{\partial T}{\partial r} \right|_{r=R} - \epsilon \sigma T|_{r=R}^4 = (1 - \Lambda) S_\odot, \qquad (3.14)$$

where k is the thermal conductivity, R is the radius of the body, ϵ is the emissivity, σ is the Stefan-Boltzmann constant, Λ is the bond albedo, and $S_\odot(\theta, \phi, t)$ is the solar insolation at any point on the surface at time t. Equations (3.13) and (3.14) uniquely determine the temperature at any point in the body at any time.

3.1 Linearization

The radiative term $\epsilon \sigma T|_{r=R}^4$ in boundary condition (3.14) makes this problem non-linear. To overcome this difficulty, we assume that the temperatures in the body are never much different than some "mean" temperature T_0, allowing us to write

$$T(r, \theta, \phi, t) = T_0 + \Delta T(r, \theta, \phi, t), \qquad (3.15)$$

where $\Delta T / T_0$ is a small quantity. Multiplying,

$$T^4 = (T_0 + \Delta T)^4 = T_0^4 + 4T_0^3 \Delta T + 6T_0^2 (\Delta T)^2 + 4T_0 (\Delta T)^3 + (\Delta T)^4, \qquad (3.16)$$

so to first order in ΔT,

$$T^4 \simeq T_0^4 + 4T_0^3 \Delta T. \qquad (3.17)$$

Using (3.15) and (3.17), we can now rewrite (3.13) and (3.14) in terms of ΔT:

$$\frac{\partial \Delta T}{\partial t} = \kappa \nabla^2 \Delta T, \qquad (3.18)$$

and

$$k \left. \frac{\partial \Delta T}{\partial r} \right|_{r=R} - \epsilon\sigma(T_0^4 + 4T_0^3 \Delta T|_{r=R}) = (1 - \Lambda)S_{\odot}. \tag{3.19}$$

This problem is linear in ΔT.

3.2 General solutions of the linear problem

General solutions to (3.18) may be found using the well-known method of separation of variables. Begin by assuming that ΔT can be written as a product of independent functions of each variable:

$$\Delta T(r, \theta, \phi, t) = \mathcal{R}(r)\mathcal{H}(\theta)\mathcal{G}(\phi)\mathcal{T}(t). \tag{3.20}$$

Inserting (3.20) into (3.18) and rearranging,

$$\frac{1}{\mathcal{T}} \frac{d\mathcal{T}}{dt} = \frac{\kappa}{\mathcal{R}\mathcal{H}\mathcal{F}} \nabla^2 (\mathcal{R}\mathcal{H}\mathcal{F}). \tag{3.21}$$

In order that the left-hand side of (3.21), which depends only on t, be equal to the right-hand side, which does not depend on t, both sides must be constant. If we call this separation constant η, then the left-hand side simplifies to

$$\frac{d\mathcal{T}}{dt} - \eta\mathcal{T} = 0 \tag{3.22}$$

and the right-hand side simplifies to

$$\kappa\nabla^2(\mathcal{R}\mathcal{H}\mathcal{F}) - \eta\mathcal{R}\mathcal{H}\mathcal{F} = 0. \tag{3.23}$$

If we let $\eta = -in\beta$, where n is an integer, then the solution to (3.22) can be written as a Fourier series:

$$\mathcal{T}(t) = \sum_{n=-\infty}^{\infty} a_n e^{-in\beta t}. \tag{3.24}$$

In a manner similar to the above, the remaining equation, (3.23), can be separated. I omit the details, but the general procedure is to write the Laplacian in spherical

coordinates, separating out first the r-dependence, then the θ-dependence. Written in their well-known forms, the separated equations are:

$$u^2\frac{d^2\mathcal{R}}{du^2} + 2u\frac{d\mathcal{R}}{du} + [u^2 - l(l+1)]\mathcal{R} = 0 \; ; \quad u = r\sqrt{in\beta/\kappa} \quad (3.25)$$

$$(1-x^2)\frac{d^2\mathcal{H}}{dx^2} - 2x\frac{d\mathcal{H}}{dx} + \left[l(l+1) - \frac{m^2}{1-x^2}\right]\mathcal{H} = 0 \; ; \quad x = \cos\theta \quad (3.26)$$

$$\frac{d^2\mathcal{G}}{d\phi^2} + m^2\mathcal{G} = 0, \quad (3.27)$$

where m^2 and $l(l+1)$ are separation constants. Solutions to (3.25) that are defined at $r = 0$ are the spherical Bessel functions

$$\mathcal{R}_l(r) = j_l(r\sqrt{in\beta/\kappa}). \quad (3.28)$$

The sign of the square root in (3.25) is irrelevant, so we choose the positive root. Solutions to (3.26) that are defined everywhere on the unit sphere are the Legendre functions

$$\mathcal{H}_{lm}(\theta) = P_l^m(\cos\theta). \quad (3.29)$$

In order to satisfy Legendre's equation, l is required to be a non-negative integer and m must range between $-l$ and l. Solutions to (3.27) are complex exponentials

$$\mathcal{G}_m(\phi) = e^{im\phi}. \quad (3.30)$$

The requirement that $\mathcal{G}_m(\phi)$ be single valued forces m to be an integer. The relevant general solution for (3.18) is now

$$\Delta T(r,\theta,\phi,t) = \sum_{n=-\infty}^{\infty} \sum_{l=0}^{\infty} \sum_{m=-l}^{l} \gamma_{nlm} j_l(r\sqrt{in\beta/\kappa}) Y_l^m(\theta,\phi) e^{-in\beta t}, \quad (3.31)$$

where $Y_l^m(\theta,\phi) \propto P_l^m(\cos\theta)e^{im\phi}$ are the spherical harmonics and the coefficients γ_{nlm} remain to be determined. The completeness of the basis functions guarantees that the solution (3.31) is unique.

For this simple treatment, we will use only terms with $l = 1$. To demonstrate that this is reasonable, we examine the representation term-by-term. In terms

of standard functions, the spherical harmonics with $l \leq 1$ are:

$$Y_0^0(\theta, \phi) = \left(\frac{1}{4\pi}\right)^{1/2}$$

$$Y_1^0(\theta, \phi) = \frac{1}{2}\left(\frac{3}{\pi}\right)^{1/2} \cos\theta$$

$$Y_1^{\pm 1}(\theta, \phi) = \mp\frac{1}{2}\left(\frac{3}{2\pi}\right)^{1/2} \sin\theta e^{\pm i\phi}. \tag{3.32}$$

Because Y_0^0 is isotropic, the $l = 0$ term will not contribute to a net reradiation force. Therefore, we can neglect that term. Y_1^0 corresponds to a north-south temperature asymmetry, analogous to a diurnally-averaged northern summer/southern winter surface temperature distribution. That seasonal temperature asymmetry will produce a Yarkovsky force component parallel to the spin axis. $Y_1^{\pm 1}$ corresponds to an azimuthal temperature asymmetry (represented by $e^{\pm i\phi}$) with an equator-to-pole temperature variation (represented by $\sin\theta$). That diurnal temperature asymmetry will contribute a force component in the equatorial plane. For this simple treatment, these spherical harmonics provide an adequate heuristic representation of the relevant thermal behavior at the surface of a rotating spherical body orbiting a single radiation source. so no other terms will be included in the temperature solution (3.31).

3.3 Insolation term

Referring to Fig. 3.3, the solar insolation term $S_\odot$ can be written

$$S_\odot(\theta, \phi, t) = S_0 \begin{cases} \hat{\mathbf{r}} \cdot \hat{\mathbf{s}}(t) & : \hat{\mathbf{r}} \cdot \hat{\mathbf{s}}(t) > 0 \\ 0 & : \text{otherwise} \end{cases}, \tag{3.33}$$

where the angular dependence on the right-hand side is contained in $\hat{\mathbf{r}}$. S_0 is the flux at the subsolar point. As the temperature solution is written as a linear combination of spherical harmonics, we seek an analogous representation for the insolation function,

$$S_\odot(\theta, \phi, t) = \sum_{l=0}^{\infty} \sum_{m=-l}^{l} s_{lm}(t) Y_l^m(\theta, \phi), \tag{3.34}$$

so that the boundary condition can be satisfied term-by-term. To determine the time-dependent coefficients $s_{lm}(t)$, we proceed in the standard way by equating (3.33) and (3.34), multiplying both sides by complex-conjugate spherical harmonics, and integrating:

$$\sum_{l=0}^{\infty} \sum_{m=-l}^{l} s_{lm} \int d\Omega \, Y_l^m Y_p^{*q} = \int d\Omega \, Y_p^{*q} \begin{cases} \hat{\mathbf{r}} \cdot \hat{\mathbf{s}} & : \hat{\mathbf{r}} \cdot \hat{\mathbf{s}} > 0 \\ 0 & : \text{otherwise} \end{cases}, \qquad (3.35)$$

where $\int d\Omega$ indicates that the integral is taken over all directions. The orthogonality of the spherical harmonics,

$$\int d\Omega \, Y_l^m Y_p^{*q} = \delta_{lp} \delta_{mq}, \qquad (3.36)$$

where δ_{ij} is the Kroenecker delta, allows us to write

$$s_{pq}(t) = \int d\Omega \, Y_p^{*q}(\theta, \phi) \begin{cases} \hat{\mathbf{r}} \cdot \hat{\mathbf{s}}(t) & : \hat{\mathbf{r}} \cdot \hat{\mathbf{s}}(t) > 0 \\ 0 & : \text{otherwise} \end{cases}. \qquad (3.37)$$

For the case with arbitrary obliquity, this integral is extremely difficult to evaluate. Therefore, we simplify the integral by neglecting the piecewise nature of the integrand:

$$s_{pq}(t) = \int d\Omega \, Y_p^{*q}(\theta, \phi)(\hat{\mathbf{r}} \cdot \hat{\mathbf{s}}(t)). \qquad (3.38)$$

This simplification, which is used in all of the relevant analytical theories[1], is rather drastic, but it will be seen later (in comparison with numerical modeling) that that the results of those theories are reasonably accurate in the limited circumstances under which they are intended to apply.

Anticipating a term-by-term correspondence when the boundary condition is applied, we compute only the $l = 1$ coefficients. Writing

$$\hat{\mathbf{r}} \cdot \hat{\mathbf{s}} = \sin\theta \sin\theta_s \cos\phi \cos\phi_s + \sin\theta \sin\theta_s \sin\phi \sin\phi_s + \cos\theta \cos\theta_s, \qquad (3.39)$$

---

[1]This simplification is not, however, used by Peterson (1976), but that theory assumes $\iota = 0$, greatly simplifying the problem.

where (θ_s, ϕ_s) are the polar coordinates of the subsolar point, and using expressions (3.32), integral (3.38) may be written in terms of simple integrals and evaluated, yielding

$$s_{10}(t) = \sqrt{\frac{\pi}{3}} S_0 \cos \theta_s(t)$$

$$s_{1\pm1}(t) = \mp \frac{1}{2} \sqrt{\frac{\pi}{6}} S_0 \sin \theta_s(t) e^{\mp i \phi_s(t)}. \qquad (3.40)$$
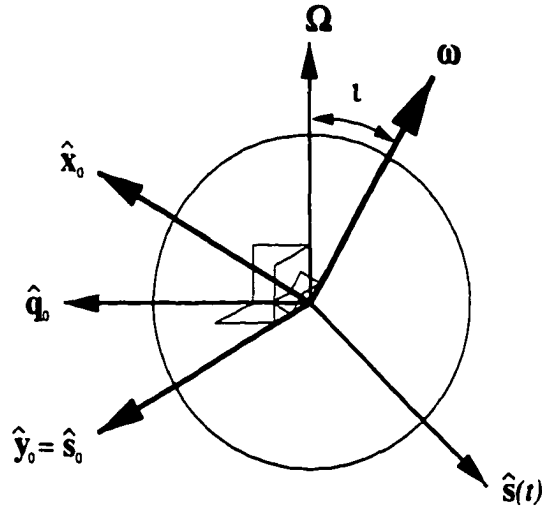
Figure 3.4: Initial geometry relevant to the determination of $\hat{s}(t)$ in the body-fixed frame. The bold vectors ($\hat{x}_0$, $\hat{y}_0$, and $\hat{\omega}$) are the rotating body-fixed axes. Ω is the orbital angular velocity vector, $\hat{s}_0 = \hat{s}(t = 0)$, and $\hat{q}_0 = \hat{s}_0 \times \hat{\Omega}$ is introduced to simplify the notation.

The angles $\theta_s(t)$ and $\phi_s(t)$ must now be determined explicitly as functions of time. The initial configuration (i.e., at time $t = 0$) is shown in Fig. 3.4. Ω is the body's angular velocity in orbit about the sun and ω is the body's angular velocity about its spin axis. The obliquity ι is the angle between Ω and ω. $\hat{s}_0 = \hat{s}(t = 0)$, the vector pointing from the body to the sun at time $t = 0$, is chosen such that it is normal to ω. $\hat{q}_0 = \hat{s}_0 \times \hat{\Omega}$ is introduced to simplify the notation. Together with $\hat{\omega}$, $\hat{x}_0$ and $\hat{y}_0$ form the initial body-fixed coordinate system oriented such that $\hat{y}_0 = \hat{s}_0$. Note that with these assumptions, the vectors $\hat{q}_0$, $\hat{x}_0$, Ω, and ω are coplanar.

To determine $\theta_s(t)$ and $\phi_s(t)$, we must find $\hat{s}(t)$ and project it along the axes of the body-fixed coordinate system $(\hat{x}(t), \hat{y}(t), \hat{\omega})$. This coordinate system rotates with angular speed ω about the spin axis $\hat{\omega}$ starting from the inital configuration given in Fig. 3.4.

Since the orbit is assumed to be circular, $\hat{s}(t)$ simply rotates with constant angular speed Ω about the orbit normal $\hat{\Omega}$. Therefore, by inspection of Fig. 3.4,

$$\hat{s}(t) = \hat{s}_0 \cos \Omega t - \hat{q}_0 \sin \Omega t. \tag{3.41}$$

Similarly, the body-fixed axes, which rotate at constant angular speed ω about $\hat{\omega}$ are

$$\hat{x}(t) = \hat{x}_0 \cos \omega t + \hat{y}_0 \sin \omega t, \tag{3.42}$$

and

$$\hat{y}(t) = \hat{y}_0 \cos \omega t - \hat{x}_0 \sin \omega t. \tag{3.43}$$

Now $\cos \theta_s(t)$ can be determined. It is the projection of $\hat{s}(t)$ on the spin axis $\hat{\omega}$:

$$\begin{aligned} \cos \theta_s(t) &= \hat{\omega} \cdot \hat{s}(t) \\ &= (\hat{\omega} \cdot \hat{s}_0) \cos \Omega t + (\hat{\omega} \cdot \hat{q}_0) \sin \Omega t \\ &= -\sin \iota \sin \Omega t, \end{aligned} \tag{3.44}$$

since, from inspection of Fig. 3.4, $\hat{\omega} \cdot \hat{q}_0 = \cos(\pi/2 + \iota) = -\sin \iota$. Converting $\sin \Omega t$ to exponential, form we obtain

$$\cos \theta_s(t) = \frac{i}{2} \sin \iota (e^{i\Omega t} - e^{-i\Omega t}). \tag{3.45}$$

The needed functions of the solar azimuth are

$$\sin \phi_s(t) = \frac{s_y}{\sqrt{s_x^2 + s_y^2}} \quad \text{and} \quad \cos \phi_s(t) = \frac{s_x}{\sqrt{s_x^2 + s_y^2}}, \tag{3.46}$$

where s_x and s_y are the projections of $\hat{s}(t)$ along the rotating body-fixed axes $\hat{x}(t)$ and $\hat{y}(t)$. From inspection of Fig. 3.4, $\sqrt{s_x^2 + s_y^2} = \sin \theta_s(t)$, so

$$\sin \phi_s(t) = \frac{s_y}{\sin \theta_s(t)} \quad \text{and} \quad \cos \phi_s(t) = \frac{s_x}{\sin \theta_s(t)}. \tag{3.47}$$

Therefore,

$$\sin\theta_s(t)e^{\pm i\phi_s(t)} = \sin\theta_s(t)(\cos\phi_s(t) \pm i\sin\phi_s(t))$$
$$= s_x \pm is_y. \tag{3.48}$$

The projections s_x and s_y are

$$s_x = \hat{\mathbf{x}}(t)\cdot\hat{\mathbf{s}}(t)$$
$$= (\hat{\mathbf{s}}_0\cdot\hat{\mathbf{x}}_0)\cos\Omega t\cos\omega t + (\hat{\mathbf{s}}_0\cdot\hat{\mathbf{y}}_0)\cos\Omega t\sin\omega t$$
$$-(\hat{\mathbf{q}}_0\cdot\hat{\mathbf{x}}_0)\sin\Omega t\cos\omega t - (\hat{\mathbf{q}}_0\cdot\hat{\mathbf{y}}_0)\sin\Omega t\sin\omega t, \tag{3.49}$$

and

$$s_y = \hat{\mathbf{y}}(t)\cdot\hat{\mathbf{s}}(t)$$
$$= (\hat{\mathbf{s}}_0\cdot\hat{\mathbf{y}}_0)\cos\Omega t\cos\omega t - (\hat{\mathbf{s}}_0\cdot\hat{\mathbf{x}}_0)\cos\Omega t\sin\omega t$$
$$-(\hat{\mathbf{q}}_0\cdot\hat{\mathbf{y}}_0)\sin\Omega t\cos\omega t + (\hat{\mathbf{q}}_0\cdot\hat{\mathbf{x}}_0)\sin\Omega t\sin\omega t. \tag{3.50}$$

By inspection of Fig. 3.4,

$$\hat{\mathbf{s}}_0\cdot\hat{\mathbf{x}}_0 = 0$$
$$\hat{\mathbf{s}}_0\cdot\hat{\mathbf{y}}_0 = 1$$
$$\hat{\mathbf{q}}_0\cdot\hat{\mathbf{x}}_0 = \cos\iota$$
$$\hat{\mathbf{q}}_0\cdot\hat{\mathbf{y}}_0 = 0, \tag{3.51}$$

so

$$s_x = \cos\Omega t\sin\omega t - \cos\iota\sin\Omega t\cos\omega t$$
$$s_y = \cos\Omega t\cos\omega t + \cos\iota\sin\Omega t\sin\omega t. \tag{3.52}$$

Therefore,

$$\sin\theta_s(t)e^{\pm i\phi_s(t)} = s_x \pm is_y$$
$$= \cos\Omega t\sin\omega t - \cos\iota\sin\Omega t\cos\omega t$$
$$\pm i(\cos\Omega t\cos\omega t + \cos\iota\sin\Omega t\sin\omega t)$$

$$
\begin{aligned}
&= \cos \Omega t (\sin \omega t \pm i \cos \omega t) + \\
&\quad \cos \iota \sin \Omega t (-\cos \omega t \pm i \sin \omega t) \\
&= e^{\mp i \omega t} (\pm i \cos \Omega t - \cos \iota \sin \Omega t).
\end{aligned} \tag{3.53}
$$

Rewriting $\sin \Omega t$ and $\cos \Omega t$ in exponential form and using a half-angle identity to rewrite $\cos \iota$ as $2 \cos^2(\iota/2) - 1$,

$$
\sin \theta_s(t) e^{\pm i \phi_s(t)} = \frac{i}{2} e^{\pm i \omega t} \left[\pm \left(e^{i \Omega t} + e^{-i \Omega t} \right) + \left(2 \cos^2 \frac{\iota}{2} - 1 \right) \left(e^{i \Omega t} - e^{-i \Omega t} \right) \right]. \tag{3.54}
$$

Multiplying out all of the terms and rearranging we obtain

$$
\sin \theta_s(t) e^{\pm i \phi_s(t)} = \pm i \sin^2 \frac{\iota}{2} e^{\mp i(\omega + \Omega) t} \pm i \cos^2 \frac{\iota}{2} e^{\mp i(\omega - \Omega) t}. \tag{3.55}
$$

Thus, substituting into (3.40), the coefficients for the insolation term are:

$$
\begin{aligned}
s_{10}(t) &= \frac{i}{2} \sqrt{\frac{\pi}{3}} S_0 \sin \iota (e^{i \Omega t} - e^{-i \Omega t}) \\
s_{1 \pm 1}(t) &= -\frac{i}{2} \sqrt{\frac{\pi}{6}} S_0 \left[\sin^2 \frac{\iota}{2} e^{\mp i(\omega + \Omega) t} + \cos^2 \frac{\iota}{2} e^{\mp i(\omega - \Omega) t} \right].
\end{aligned} \tag{3.56}
$$

3.4 Surface temperature solution

Having expressed the linear solution $\Delta T(r, \theta, \phi, t)$ and the insolation term $S_\odot(\theta, \phi, t)$ as linear combinations of spherical harmonics and exponentials, we are now ready to complete the solution by using the boundary condition (3.19) to determine the coefficients γ_{nlm} in (3.31).

Writing the linear solution and the insolation term explicitly, keeping only the terms with $l = 1$, we have

$$
\Delta T(r, \theta, \phi, t) = \tag{3.57}
$$
$$
\sum_{n=-\infty}^{\infty} j_1(r \sqrt{in\beta/\kappa}) e^{-in\beta t} \left[\gamma_{n10} Y_1^0(\theta, \phi) + \gamma_{n11} Y_1^1(\theta, \phi) + \gamma_{n1-1} Y_1^{-1}(\theta, \phi) \right]
$$
$$
S_\odot(\theta, \phi, t) = s_{10}(t) Y_1^0(\theta, \phi) + s_{11}(t) Y_1^1(\theta, \phi) + s_{1-1}(t) Y_1^{-1}(\theta, \phi). \tag{3.58}
$$

We also need the radial derivative:

$$\frac{\partial \Delta T}{\partial r} = \sum_{n=-\infty}^{\infty} k\sqrt{\frac{in\beta}{\kappa}}\frac{dj_1}{dr}(r\sqrt{in\beta/\kappa}) \tag{3.59}$$

$$e^{-in\beta t}\left[\gamma_{n10}Y_1^0(\theta,\phi) + \gamma_{n11}Y_1^1(\theta,\phi) + \gamma_{n1-1}Y_1^{-1}(\theta,\phi)\right]. \tag{3.60}$$

Inserting (3.58) and (3.60) into the boundary condition (3.19),

$$\sum_{n=-\infty}^{\infty}\left[k\sqrt{\frac{in\beta}{\kappa}}\left.\frac{dj_1}{dr}\right|_{R\sqrt{in\beta/\kappa}} - 4\epsilon\sigma T_0^3 j_1(R\sqrt{in\beta/\kappa})\right]$$

$$e^{-in\beta t}\left[\gamma_{n10}Y_1^0(\theta,\phi) + \gamma_{n11}Y_1^1(\theta,\phi) + \gamma_{n1-1}Y_1^{-1}(\theta,\phi)\right] - \epsilon\sigma T_0^4$$

$$= (1-\Lambda)[s_{10}(t)Y_1^0(\theta,\phi) + s_{11}(t)Y_1^1(\theta,\phi) + s_{1-1}(t)Y_1^{-1}(\theta,\phi)]. \tag{3.61}$$

Since the spherical harmonics are linearly independent, the boundary condition may only be satisfied by equating the coefficients of each harmonic.

3.4.1 Seasonal term

The term proportional to $Y_1^0(\theta,\phi)$ has no ϕ-dependence (see (3.32)) and is associated with only the orbital period. This term represents the diurnally-averaged seasonal temperature distribution. Matching terms with $m = 0$ in (3.61),

$$\sum_{n=-\infty}^{\infty}\gamma_{n10}\left[k\sqrt{\frac{in\beta}{\kappa}}\left.\frac{dj_1}{dr}\right|_{R\sqrt{in\beta/\kappa}} - 4\epsilon\sigma T_0^3 j_1(R\sqrt{in\beta/\kappa})\right]e^{-in\beta t} = (1-\Lambda)s_{10}(t). \tag{3.62}$$

Substituting for $s_{10}(t)$ from (3.56) and defining

$$\xi_n \equiv k\sqrt{\frac{in\beta}{\kappa}}\left.\frac{dj_1}{dr}\right|_{R\sqrt{in\beta/\kappa}} - 4\epsilon\sigma T_0^3 j_1(R\sqrt{in\beta/\kappa}), \tag{3.63}$$

we have

$$\sum_{n=-\infty}^{\infty}\gamma_{n10}\xi_n e^{-in\beta t} = \frac{i}{2}\sqrt{\frac{\pi}{3}}S_0(1-\Lambda)\sin\iota(e^{i\Omega t} - e^{-i\Omega t}). \tag{3.64}$$

The linear independence of the eigenvalues $e^{i\Omega t}$ and $e^{-i\Omega t}$ implies that $\beta = \Omega$ and the only nonzero coefficients γ_{n10} are γ_{110} and γ_{-110}. Therefore,

$$\gamma_{110}\xi_1 e^{-i\Omega t} + \gamma_{-110}\xi_{-1}e^{i\Omega t} = \frac{i}{2}\sqrt{\frac{\pi}{3}}S_0(1-\Lambda)\sin\iota(e^{i\Omega t} - e^{-i\Omega t}). \tag{3.65}$$

Matching terms, we obtain

$$\gamma_{\pm 110} = \mp \frac{i}{2} \sqrt{\frac{\pi}{3}} \frac{S_0 (1 - \Lambda) \sin \iota}{\xi_{\pm 1}}.$$

(3.66)

Substituting (3.66) into the temperature solution (3.58), the seasonal term at any point within the body is

$$\Delta T_{\text{seasonal}}(r, \theta, t) = \frac{i}{4} S_0 (1 - \Lambda) \sin \iota \left[\frac{j_1(r\sqrt{-i\Omega/\kappa})}{\xi_{-1}} e^{i\Omega t} - \frac{j_1(r\sqrt{i\Omega/\kappa})}{\xi_1} e^{-i\Omega t} \right] \cos \theta.$$

(3.67)

As the Yarkovsky force is evaluated at $r = R$, we require only the surface form of the seasonal term:

$$\Delta T_{\text{seasonal}}(R, \theta, t) = \frac{i}{4} S_0 (1 - \Lambda) \sin \iota \left[\frac{j_1(R\sqrt{-i\Omega/\kappa})}{\xi_{-1}} e^{i\Omega t} - \frac{j_1(R\sqrt{i\Omega/\kappa})}{\xi_1} e^{-i\Omega t} \right] \cos \theta.$$

(3.68)

Defining

$$\Psi(z) \equiv z \frac{j_1'(z)}{j_1(z)},$$

(3.69)

where the prime indicates differentiation with respect to the argument, the coefficients of the complex exponentials in (3.68) may be written

$$\frac{j_1(R\sqrt{\pm i\Omega/\kappa})}{\xi_{\pm 1}} = \left[\frac{k}{R} \Psi \left(R\sqrt{\pm i\Omega/\kappa} \right) - 4\epsilon\sigma T_0^3 \right]^{-1}.$$

(3.70)

Since these coefficients are simply complex conjugates of one another, we may write[2]

$$\left[\frac{k}{R} \Psi \left(R\sqrt{\pm i\Omega/\kappa} \right) - 4\epsilon\sigma T_0^3 \right]^{-1} = \chi_S \pm i\psi_S = A' e^{\pm i\epsilon}.$$

(3.71)

Therefore, using (3.63), (3.68) may be rewritten

$$\Delta T_{\text{seasonal}}(R, \theta, t) = \frac{i}{4} S_0 (1 - \Lambda) \sin \iota \left[A' e^{i(\Omega t - \epsilon)} - A' e^{-i(\Omega t - \epsilon)} \right] \cos \theta$$

$$= -\frac{1}{2} A' S_0 (1 - \Lambda) \sin \iota \sin(\Omega t - \epsilon) \cos \theta,$$

(3.72)

with surface seasonal lag

$$\epsilon = \tan^{-1} \frac{\psi_S}{\chi_S},$$

(3.73)

and surface amplitude,

$$A' = \sqrt{\chi_S^2 + \psi_S^2}.$$

(3.74)

---

[2]See Appendix B for a representation in terms of ordinary functions.

3.4.2 Diurnal terms

Terms in (3.58) with $m = \pm 1$ contain the rotation frequency as well as the orbital frequency. These terms represent the diurnal temperature distribution. Matching terms with $m = \pm 1$ in (3.61) and substituting for $s_{1\pm 1}(t)$ from (3.56), we have

$$\sum_{n=-\infty}^{\infty} \gamma_{n1\pm 1} \xi_n e^{-in\Omega t} = -\frac{i}{2}\sqrt{\frac{\pi}{6}} S_0(1-\Lambda) \left[\sin^2\frac{\iota}{2} e^{\mp i(\omega+\Omega)t} + \cos^2\frac{\iota}{2} e^{\mp i(\omega-\Omega)t}\right]. \quad (3.75)$$

In order to satisfy the above condition for arbitrary ω, the Fourier series on the left-hand side must contain an infinite number of frequencies, the coefficients $\gamma_{n1\pm 1}$ being related to the Fourier transforms of $e^{\mp i(\omega+\Omega)t}$ and $e^{\mp i(\omega-\Omega)t}$. However, if we simplify the treatment with the assumption that the quantity $\omega/\Omega \equiv h$ is an integer, we can write

$$\sum_{n=-\infty}^{\infty} \gamma_{n1\pm 1} \xi_n e^{-in\Omega t} = -\frac{i}{2}\sqrt{\frac{\pi}{6}} S_0(1-\Lambda) \left[\sin^2\frac{\iota}{2} e^{\mp i(h+1)\Omega t} + \cos^2\frac{\iota}{2} e^{\mp i(h-1)\Omega t}\right]. \quad (3.76)$$

As in the previous section, the linear independence of the eigenvalues $e^{in\Omega t}$ and $e^{-in\Omega t}$ implies that the only nonzero coefficients are $\gamma_{(h+1)11}$, $\gamma_{-(h+1)1-1}$, $\gamma_{(h-1)11}$, and $\gamma_{-(h-1)1-1}$. Matching terms, we obtain

$$\gamma_{\pm(h+1)1\pm 1} = -\frac{i}{2}\sqrt{\frac{\pi}{6}} \frac{S_0(1-\Lambda)\sin^2\iota}{\xi_{\pm(h+1)}}$$

$$\gamma_{\pm(h-1)1\pm 1} = -\frac{i}{2}\sqrt{\frac{\pi}{6}} \frac{S_0(1-\Lambda)\cos^2\iota}{\xi_{\pm(h-1)}}. \quad (3.77)$$

Therefore, substituting (3.77) into the temperature solution (3.58), the diurnal part of the temperature solution at any point on the surface of the body is

$$\begin{aligned}
\Delta T_{\text{diurnal}}(r,\theta,\phi;t) = \frac{iS_0(1-\Lambda)}{8} &\left[\left(\frac{j_1(R\sqrt{i(h+1)\Omega/\kappa})}{\xi_{h+1}} e^{-i[(h+1)\Omega t-\phi]}\right.\right. \\
&\left.- \frac{j_1(R\sqrt{-i(h+1)\Omega/\kappa})}{\xi_{-(h+1)}} e^{i[(h+1)\Omega t-\phi]}\right) \sin^2\frac{\iota}{2} \\
&+ \left(\frac{j_1(R\sqrt{i(h-1)\Omega/\kappa})}{\xi_{h-1}} e^{-i[(h-1)\Omega t-\phi]}\right.
\end{aligned}$$

$$-\frac{j_1(R\sqrt{-i(h-1)\Omega/\kappa})}{\xi_{-(h-1)}}e^{i[(h-1)\Omega t-\phi]}\Bigg)\cos^2\frac{\iota}{2}\Bigg]\sin\theta.$$

$$(3.78)$$

Proceeding as in the previous section, we define

$$B'_{\pm}e^{\pm i\delta_{\pm}} = \frac{j_1(R\sqrt{\pm i(h\pm1)\Omega/\kappa})}{\xi_{\pm(h\pm1)}} = \left[\frac{k}{R}\Psi\left(R\sqrt{\pm i(h\pm1)\Omega/\kappa}\right) - 4\epsilon\sigma T_0^3\right]^{-1}$$

$$\equiv \chi_{D\pm}\pm i\psi_{D\pm} \qquad (3.79)$$

allowing (3.78) to be rewritten

$$\Delta T_{\text{diurnal}}(R,\theta,\phi,t) = \frac{1}{4}S_0(1-\Lambda)\left\{B'_{+}\sin[(\omega+\Omega)t-\phi-\delta_{+}]\sin^2\frac{\iota}{2}\right.$$

$$\left.+ B'_{-}\sin[(\omega-\Omega)t-\phi-\delta_{-}]\cos^2\frac{\iota}{2}\right\}\sin\theta, \quad (3.80)$$

with surface diurnal lags

$$\delta_{\pm} = \tan^{-1}\frac{\psi_{D\pm}}{\chi_{D\pm}}, \qquad (3.81)$$

and surface amplitudes,

$$B'_{\pm} = \sqrt{\chi_{D\pm}^2 + \psi_{D\pm}^2}. \qquad (3.82)$$

3.5 Yarkovsky acceleration

The Yarkovsky force contributed by each surface element is the vector sum of the momenta of all of the photons emitted by that surface element during unit time. Assuming a Lambert emission law, such that the power emitted into unit solid angle is proportional to $\cos\zeta$, where ζ is the zenith angle, it is not difficult to show that the contribution from a surface element of area $R^2\sin\theta d\theta d\phi$ is

$$d\mathbf{F}(\theta,\phi,t) = -\frac{2}{3}\frac{\epsilon\sigma T^4(\theta,\phi,t)}{c}R^2\sin\theta d\theta d\phi\hat{\mathbf{r}}(\theta,\phi). \qquad (3.83)$$

The factor of 2/3 comes from the Lambert emission law, and reflects the fact that the photons are emitted in all directions rather than purely radially. The net Yarkovsky force is obtained by integrating over the entire surface:

$$\mathbf{F}(t) = -\frac{2}{3}\frac{\epsilon\sigma R^2}{c}\int_0^{2\pi}d\phi\int_0^{\pi}\sin\theta d\theta T^4(\theta,\phi,t)\hat{\mathbf{r}}(\theta,\phi). \qquad (3.84)$$

Writing the linearized form of the temperature, $T(R, \theta, \phi, t) = T_0 + 4T_0^3 \Delta T(R, \theta, \phi, t)$, and realizing that the isotropic portion, T_0, will not contribute a net force, we have

$$
\begin{aligned}
\mathbf{F}(t) &= -\frac{8}{3} \frac{\epsilon \sigma T_0^3 R^2}{c} \int_0^{2\pi} d\phi \int_0^\pi \sin\theta d\theta \Delta T(R, \theta, \phi, t) \hat{\mathbf{r}}(\theta, \phi) \\
&= -\frac{8}{3} \frac{\epsilon \sigma T_0^3 R^2}{c} \int_0^{2\pi} d\phi \int_0^\pi \sin\theta d\theta (\Delta T_{\text{seasonal}}(R, \theta, t) + \Delta T_{\text{diurnal}}(R, \theta, \phi, t)) \hat{\mathbf{r}}(\theta, \phi) \\
&\equiv \mathbf{F}_{\text{seasonal}}(t) + \mathbf{F}_{\text{diurnal}}(t).
\end{aligned}
\tag{3.85}
$$

Substituting

$$
\hat{\mathbf{r}}(\theta, \phi) = \hat{\mathbf{x}} \sin\theta \cos\phi + \hat{\mathbf{y}} \sin\theta \sin\phi + \hat{\mathbf{z}} \cos\theta,
\tag{3.86}
$$

we obtain three simple integrals for each force term $\mathbf{F}_{\text{seasonal}}(t)$ and $\mathbf{F}_{\text{diurnal}}(t)$. The resulting accelerations are

$$
\frac{\mathbf{F}_{\text{seasonal}}(t)}{m} = -\frac{3\epsilon\sigma T_0^3 S_0(1 - \Lambda)}{2c\rho R} A' \sin\iota \sin(\Omega t - \varepsilon)\hat{\mathbf{z}} \equiv \mathbf{a}_{\text{seasonal}}(t)
\tag{3.87}
$$

and

$$
\begin{aligned}
\frac{\mathbf{F}_{\text{diurnal}}(t)}{m} = \frac{2\epsilon\sigma T_0^3 S_0(1 - \Lambda)}{3c\rho R} &\left\{ \left(B'_+ \sin^2\frac{\iota}{2} \sin[(\omega + \Omega)t - \delta_+] \right. \right. \\
&+ \left. B'_- \cos^2\frac{\iota}{2} \sin[(\omega - \Omega)t - \delta_-] \right) \hat{\mathbf{x}} \\
&+ \left(B'_+ \sin^2\frac{\iota}{2} \cos[(\omega + \Omega)t - \delta_+] \right. \\
&+ \left. \left. B'_- \cos^2\frac{\iota}{2} \cos[(\omega - \Omega)t - \delta_-] \right) \hat{\mathbf{y}} \right\} \\
&\equiv \mathbf{a}_{\text{diurnal}}(t),
\end{aligned}
\tag{3.88}
$$

where $m = \frac{4}{3}\pi R^3 \rho$ is the mass of the body. As expected, the seasonal acceleration is directed along the rotation axis and the diurnal acceleration lies in the equatorial plane. Defining

$$
A \equiv \frac{3\epsilon\sigma T_0^3 S_0(1 - \Lambda)}{2c\rho R} A'
\tag{3.89}
$$

and

$$
B_\pm \equiv \frac{2\epsilon\sigma T_0^3 S_0(1 - \Lambda)}{3c\rho R} B'_\pm,
\tag{3.90}
$$

the total acceleration is

$$
\begin{aligned}
\mathbf{a}(t) &= \mathbf{a}_{\text{seasonal}}(t) + \mathbf{a}_{\text{diurnal}}(t) \\
&= \left(B_+ \sin^2 \frac{\iota}{2} \sin[(\omega + \Omega)t - \delta_+] \right. \\
&\quad \left. + B_- \cos^2 \frac{\iota}{2} \sin[(\omega - \Omega)t - \delta_-] \right) \hat{\mathbf{x}} \\
&\quad + \left(B_+ \sin^2 \frac{\iota}{2} \cos[(\omega + \Omega)t - \delta_+] \right. \\
&\quad \left. + B_- \cos^2 \frac{\iota}{2} \cos[(\omega - \Omega)t - \delta_-] \right) \hat{\mathbf{y}} - A \sin \iota \sin(\Omega t - \varepsilon)\hat{\mathbf{z}}. \quad (3.91)
\end{aligned}
$$

The algebra in the next section is simplified if we use (3.42) and (3.43) to rewrite the acceleration in terms of basis vectors that are fixed in the inertial frame:

$$
\begin{aligned}
\mathbf{a}(t) &= B_+ \sin^2 \frac{\iota}{2}[\hat{\mathbf{x}}_0 \sin(\Omega t - \delta_+) + \hat{\mathbf{y}}_0 \cos(\Omega t - \delta_+)] \\
&\quad + B_- \cos^2 \frac{\iota}{2}[\hat{\mathbf{y}}_0 \cos(\Omega t + \delta_-) - \hat{\mathbf{x}}_0 \sin(\Omega t + \delta_-)] \\
&\quad - A \sin \iota \sin(\Omega t - \varepsilon)\hat{\mathbf{z}}. \quad (3.92)
\end{aligned}
$$

3.6 Semimajor axis perturbation

To determine orbital element perturbations, it is necessary to insert the Yarkovsky acceleration into Gauss' perturbation equations. For the purposes of this simple demonstration, it will be sufficient to compute only the strongest effect, da/dt. The equation for da/dt is

$$
\frac{da}{dt} = \frac{2}{\Omega\sqrt{1 - e^2}} \left[F_r e \sin f + \frac{a(1 - e^2)F_t}{r} \right], \quad (3.93)
$$

where F_r and F_t are the radial and tangential acceleration components respectively. Because here we assume $e = 0$, we can write $r = a$, yielding the simplified form

$$
\frac{da}{dt} = \frac{2}{\Omega} F_t. \quad (3.94)
$$

Referring to Fig. 3.4, the tangential acceleration is

$$
F_t = \mathbf{a}(t) \cdot [\hat{\mathbf{s}}(t) \times \hat{\mathbf{\Omega}}]. \quad (3.95)
$$

Substituting (3.41) and (3.92) for $\hat{s}(t)$ and the acceleration respectively, and noticing in Fig. 3.4 that $\hat{z} \cdot \hat{s}_0 = 0$ and $\hat{z} \cdot \hat{q}_0 = -\sin \iota$, we obtain

$$
\begin{aligned}
F_t =\ & A \sin \Omega t \cos(\Omega t - \varepsilon) \sin^2 \iota \\
& - B_+ \sin^2 \frac{\iota}{2} [\sin(\Omega t - \delta_+) \cos \Omega t \cos \iota + \cos(\Omega t - \delta_+) \sin \Omega t] \\
& - B_- \cos^2 \frac{\iota}{2} [\cos(\Omega t + \delta_-) \sin \Omega t - \sin(\Omega t + \delta_-) \cos \Omega t \cos \iota].
\end{aligned}
\tag{3.96}
$$

As a check, for zero obliquity, this tangential acceleration becomes

$$
\begin{aligned}
F_t &= -B_- \frac{\iota}{2} [\cos(\Omega t + \delta_-) \sin \Omega t - \sin(\Omega t + \delta_-) \cos \Omega t] \\
&= B_- \sin \delta_- = \text{constant},
\end{aligned}
\tag{3.97}
$$

which makes sense because for this obliquity the surface temperature distribution should be stationary in a frame rotating at the orbital period.

Averaging over an orbit and using (3.94) and (3.96),

$$
\begin{aligned}
\left\langle \frac{da}{dt} \right\rangle &= \frac{\Omega}{2\pi} \int_0^{\frac{\Omega}{2\pi}} \frac{da}{dt} dt \\
&= \frac{1}{\pi} \int_0^{\frac{\Omega}{2\pi}} F_t \, dt \\
&= A \sin \varepsilon \sin^2 \iota + B_+ \sin \delta_+ \sin^2 \frac{\iota}{2} (\cos \iota - 1) + B_- \sin \delta_- \cos^2 \frac{\iota}{2} (\cos \iota + 1).
\end{aligned}
\tag{3.98}
$$

Using the identity $\cos \iota = 2 \cos^2 \frac{\iota}{2} - 1 = 1 - 2 \sin^2 \frac{\iota}{2}$, (3.98) becomes

$$
\begin{aligned}
\left\langle \frac{da}{dt} \right\rangle &= A \sin^2 \iota \sin \varepsilon + B_- \cos^4 \frac{\iota}{2} \sin \delta_- - B_+ \sin^4 \frac{\iota}{2} \sin \delta_+ \\
&= \left\langle \frac{da}{dt} \right\rangle_{\text{seasonal}} + \left\langle \frac{da}{dt} \right\rangle_{\text{diurnal}},
\end{aligned}
\tag{3.99}
$$

where

$$
\begin{aligned}
\left\langle \frac{da}{dt} \right\rangle_{\text{seasonal}} &= A \sin \varepsilon \sin^2 \iota \\
\left\langle \frac{da}{dt} \right\rangle_{\text{diurnal}} &= B_- \cos^4 \frac{\iota}{2} \sin \delta_- - B_+ \sin^4 \frac{\iota}{2} \sin \delta_+.
\end{aligned}
\tag{3.100}
$$

3.6.1 Pure seasonal and pure diurnal limits

In this section, I discuss the seasonal and diurnal limits in terms of the analytical results. First, consider the case with zero obliquity, for any rotation frequency. In this case, $\langle da/dt \rangle_{\text{seasonal}}$ is zero so the Yarkovsky effect is purely diurnal as expected. Next, consider the behavior of (3.100) for any obliquity as $\omega \to \infty$. As ω becomes large compared to Ω, $(h \pm 1)\Omega \to \omega$ so B_- and B_+ converge to a value B while δ_- and δ_+ converge to a value δ. In this limit $\langle da/dt \rangle_{\text{diurnal}}$ becomes

$$\left\langle \frac{da}{dt} \right\rangle_{\text{diurnal}} = B \sin \delta \left(\cos^4 \frac{\iota}{2} - \sin^4 \frac{\iota}{2} \right)$$

$$= B \sin \delta \cos \iota,$$

(3.101)

confirming the well-known result (Öpik, 1951) that the diurnal component of the Yarkovsky effect scales roughly with $\cos \iota$. We also see that this result applies only to the case where the rotation frequency is much faster than the orbital frequency. As ω is increased further, B eventually approaches zero (see Appendix B) and the diurnal component is eliminated, as expected. Meanwhile, $\langle da/dt \rangle_{\text{seasonal}}$ is unaffected because it does not depend on ω. Therefore, in the case of extremely fast rotation, a purely seasonal Yarkovsky effect remains, which is also not surprising.

However, evaluating (3.100) for the case where the spin axis lies in the orbit plane (i.e., $\iota = \pi/2$), we obtain

$$\left\langle \frac{da}{dt} \right\rangle_{\text{diurnal}} = B_- \cos^4 \frac{\pi}{4} \sin \delta_- - B_+ \sin^4 \frac{\pi}{4} \sin \delta_+.$$

$$= \frac{1}{4}(B_- \sin \delta_- - B_+ \sin \delta_+).$$

(3.102)

Therefore, there is actually a small diurnal component even when the spin axis lies in the orbit plane (to my knowledge, this fact was first pointed out by Vokrouhlický and Farinella (1998)). This component remains because the body's heliocentric motion prevents surface temperatures from smearing along lines of precisely constant

latitude. If, as is typical for asteroids, the rotation frequency is fast compared to the orbital frequency, then this effect is negligible and Öpik's $\cos \iota$ scaling is appropriate as seen above.

3.7 Limitations of the linear theory

The above analytical theory is made tractable by assuming that temperature excursions ΔT are always small relative to some mean temperature T_0. Because the theory is truncated at second order in $\Delta T/T_0$, temperature excursions of, say, 25% relative to the mean cause terms of order $(\Delta T/T_0)^2 \simeq 6\%$ to be neglected. Therefore, for cases where temperature excursions are moderate, the linear theory should provide a reasonable approximation to the true temperature solution. For cases with larger temperature excursions, the validity of linear theory rapidly deteriorates because the radiative term in the boundary condition (3.19) is badly underestimated for large ΔT. In this regime, the resulting thermal balance is skewed such that temperatures tend to be overestimated and Yarkovsky forces underestimated.

Another effect that should become important as nonlinear effects emerge is nonlinear mixing of the diurnal and seasonal Yarkovsky components. I have shown (e.g. Eq. 3.99) that in the linear theory the diurnal and seasonal components simply add together to produce the total Yarkovsky effect. In reality, however, those contributions cannot be truly separated unless one or the other vanishes. This effect is investigated further in Chapter 5.

Therefore, the linear theories, even those that do not exclude noncircular orbits, are not useful for bodies on high-eccentricity orbits because the drastic difference in solar insolation between periapse and apoapse causes large temperature excursions. Moreover, the linear theory may be questionable for cases where the surface thermal conductivity is extremely low, because heat deposited at the surface remains near the surface, resulting in large temperature excursions. This is the case for asteroids with highly-insulating regolith layers. For those cases, even if the

linear theory is applicable for noncircular orbits, it should break down at a much smaller eccentricity than for bodies with higher surface thermal conductivities.

Another simplification in the theory presented in this chapter is the treatment of the insolation function as continuous over the surface of a body rather than piecewise as is the case in reality. While this simplification represents the phase of the insolation accurately, it exaggerates the extremes of the diurnal and seasonal heating cycles, and should therefore cause the magnitude of the Yarkovsky force to be significantly overestimated.

On the other hand, surface temperatures resulting from the simplified insolation function are distributed such that the along-track component of the resulting force is smaller than in reality. To understand this, consider the daily temperature variation on the equator of an asteroid with zero obliquity. In the simplified case, morning heating and evening cooling are roughly symmetric because the positive insolation during the day is identical to the negative insolation during the night. In reality, however, evening cooling is much more gradual than morning heating because the insolation function remains at zero during the evening instead of swinging negative as in the simplified case. Therefore, although the hottest point on the body occurs at roughly the same phase for both cases, the warmer evening temperatures in the real case cause a larger component of the Yarkovsky force vector to be directed along the orbit. Thus, the simplification of the insolation function used in the linear theory presented here causes two errors: 1) an overestimate of the Yarkovsky force magnitude, which alone would produce an overestimate of da/dt, and 2) an underestimate of the thermal lag, which alone would cause an underestimate of da/dt.

In the next chapter, I describe a purely numerical approach for computing Yarkovsky orbital perturbations and use it to validate results of simplified analytical theories similar to that presented in this chapter.

CHAPTER 4

A NUMERICAL APPROACH

In this chapter, I describe a general numerical method that I have developed for computing Yarkovsky orbital element perturbations. In contrast to the earlier approaches discussed in Chapter 3, this calculation is valid for bodies with virtually any orbital elements, any spin axis direction or rotation period, and arbitrary internal distribution of thermal properties. While it currently assumes spherical or ellipsoidal shapes, it may be readily generalized to treat bodies of arbitrary shape (see Chapter 11). All of the original Yarkovsky calculations presented in this dissertation were computed using this numerical approach.

4.1 Spherical calculation

To determine the thermal state of an asteroid, the heat equation is solved using a finite-difference scheme. A body is divided into discrete cells, throughout each of which the material properties and temperature are assumed uniform. The solar insolation boundary condition is computed at each timestep using an orbital integrator. First, I consider the case of a spherical body. Later in the chapter, I describe the extension to ellipsoidal bodies.

The body is represented by a collection of cells, each with uniform thermal properties. The geometry is shown in Fig. 4.5a. The center of the body is occupied by a single spherical cell. Outside the central cell, the cell spacing is uniform in longitude and latitude. In the radial direction, cells are very thin near the surface in order to adequately resolve the temperature profile.

(a)   (b)
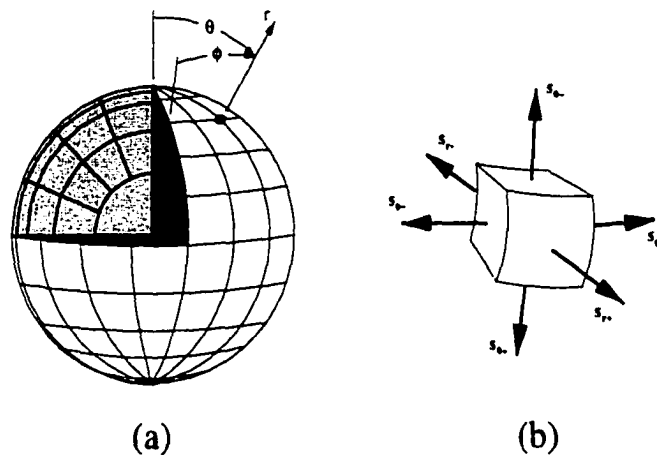
Figure 4.5: (a) Schematic of the mesh used to solve the heat equation throughout the spherical body. Cells are uniformly spaced in longitude, ϕ, and latitude, θ. In the radial direction, the spacing varies, becoming very small at the surface. The center of the body is occupied by a single spherical cell. (b) Geometry of a typical (non-central) cell. The normal vector for each face is identified by two subscripts. The first specifies which spherical coordinate (r, θ, or ϕ) is constant on the face. The second distinguishes between the two faces that bound the cell in that direction.

A typical noncentral cell is illustrated in Fig. 4.5b. $\hat{s}_{ij}$ denotes the surface unit normal to each cell face. The first subscript refers to the spherical coordinate that is constant on the cell face and the second subscript ($j = +$ or $-$) distinguishes between the two faces that bound the cell in that direction. For example, $\hat{s}_{r+}$ is the normal to the surface of a cell nearest the surface of the body. The central cell is bounded only in the radial direction, of course.

The temperature, T, in each cell of the body at time $t_0 + \Delta t$ is computed from the temperature at time t_0 in timesteps Δt using a first-order Euler scheme:

$$T(t_0 + \Delta t) = T(t_0) + \Delta t \left. \frac{\partial T}{\partial t} \right|_{t_0} + O(\Delta t^2). \tag{4.103}$$

The size of Δt is limited by the smallest cell dimension in the mesh, because in a given time interval a thermal perturbation propagates a distance

$$l \sim \sqrt{\frac{k \Delta t}{\rho c_p}}, \tag{4.104}$$

where k is the thermal conductivity, ρ is the density and c_p is the heat capacity. If the timestep were so large that l exceeded the cell size, the integration would become unrealistic because cells communicate only with their immediate neighbors. This effect could be alleviated somewhat by using a higher-order scheme to evaluate spatial derivatives. Instead, the timestep is simply limited so as to be short enough (less than 100 s) to avoid this problem. A second-order (in Δt) scheme was tested and, to several significant figures, the results were found to be identical to the those of the first-order scheme for the timestep we used.

The heat equation follows from conservation of energy. In a cell of volume V, the change in internal energy must equal the total heat flow through the cell boundary, yielding a formula for the temperature derivative, $\partial T/\partial t$ in (4.103):

$$\rho V c_p \frac{\partial T}{\partial t} = \oint \mathbf{J}(t) \cdot d\mathbf{s}, \tag{4.105}$$

where the integral is evaluated over the surface of each cell, $\mathbf{J}$ is the heat flux, and $d\mathbf{s}$ is the vector element of surface area. We assume that the cell size is small enough that the heat flux can be approximated as uniform over a given face, such that the total heat flow is calculated as

$$\begin{aligned}
\oint \mathbf{J}(t_0) \cdot d\mathbf{s} &= J_{r+}A_{r+} + J_{r-}A_{r-} \\
&\quad + J_{\theta+}A_{\theta+} + J_{\theta-}A_{\theta-} \\
&\quad + J_{\phi+}A_{\phi+} + J_{\phi-}A_{\phi-},
\end{aligned} \tag{4.106}$$

where A_{ij} and J_{ij} are the area and the heat flux on face (i,j), respectively. For any interior cell face, not exposed to the surface of the asteroid, the heat flux is conductive, so

$$J_{ij} = k(\nabla T)_{ij} \cdot \hat{\mathbf{s}}_{ij}. \tag{4.107}$$

The temperature gradient, $(\nabla T)_{ij}$, across face (i,j) of a cell centered at coordinates (r, θ, ϕ) is computed using a difference approximation of the directional derivative of the temperature field in the direction normal to the face, for example,

$$(\nabla T)_{r+} = \frac{T(r + \Delta r, \theta, \phi) - T(r, \theta, \phi)}{\Delta r}. \tag{4.108}$$

For surface cell faces, the heat flux (J_{r+}) is the difference between solar insolation inward and thermal radiation outward:

$$J_{surface} = (1 - \Lambda)S_\odot(\hat{n} \cdot \hat{r}) - \epsilon\sigma T^4, \tag{4.109}$$

where Λ is the bond albedo, $S_\odot$ is the solar flux impinging on the asteroid, $\hat{n}$ is the surface unit normal vector, and $\hat{r}$ is the unit position vector of the sun with respect to the body. Of course, on the night side, the solar insolation is zero, leaving only the last term.

After the thermal state of the body is evaluated for a given timestep, the net radiative reaction force, $\mathbf{F}$, is evaluated by summing the vector thermal radiation forces on each exterior surface element,

$$\mathbf{F} = \sum_{i=1}^{n} \mathbf{f}_i A_i, \tag{4.110}$$

where $\mathbf{f}_i$ is the force per unit area due to the emission of radiation from surface cell i. The forces due to incident and reflected sunlight are neglected because they are purely radial (with respect to the Sun) and have the same form as solar gravity, resulting only in a slight modification to the heliocentric motion with no secular variations. We assume that the emitted radiation (from any surface element) follows Lambert's law, such that the power radiated into unit solid angle is

$$I(\zeta) = \beta\cos(\zeta), \tag{4.111}$$

where ζ is the zenith angle. More sophisticated emission laws have been investigated (Vokrouhlický and Bottke, 2001), but the final results have not been shown to be sensitive to this assumption. β is a normalization factor such that

$$\int I(\zeta)d\Omega = \epsilon_i\sigma T_i^4 A_i, \tag{4.112}$$

where the integral is taken over the outward hemisphere, ϵ_i is the emissivity of the surface element, and σ is the Stefan-Boltzmann constant. Thus, the net Yarkovsky force becomes

$$\mathbf{F} = \sum_{i=1}^{n}\frac{2}{3}\frac{\epsilon_i\sigma T_i^4}{c}\hat{n}_i A_i. \tag{4.113}$$

The rates of change of the orbital elements are computed at each timestep by decomposing the Yarkovsky force vector and using the Gaussian form of the perturbation equations (Danby, 1992). To obtain the net orbital element time derivatives, the perturbations are averaged over a single orbit (while holding the orbital elements constant).

A limiting problem with this simple calculation is that for fast rotation, an impractically short timestep is required in order to adequately sample a single rotation. Periods of one hour or less require a reduction in timestep which makes a broad exploration of the parameter space impractical with the available computing resources. According to Harris (1979), typical rotation periods for well-consolidated, stony bodies with sizes of 1- 10- and 100 m may be around a minute, several minutes, and a few hours, respectively. (Farinella et al., 1998) suggest even shorter periods. Observations of bodies with diameters of tens of meters also suggest much shorter rotation periods (Pravec et al., 2000). Thus, even for the largest bodies studied in this dissertation, it is probably not practical to simulate realistic rotation rates using the current method. However, although the results for finite rotation rate can differ substantially from those for which "fast" rotation is assumed to hold, in many cases of interest, there is a fast rotation regime, in which the results are insensitive to the rotation rate (see Sec. 4.2.2 below).

4.2 Validation

4.2.1 Convergence

In order for this calculation to be meaningful, the results must be independent of the timestep and the cell size. Based on initial experiments, the largest Δt and cell size that appeared to reasonably satisfy this requirement were selected. About 5% of the cases evaluated in Chapter 5 were selected at random and recomputed using approximately twice the number of cells and a shorter timestep (10 s). In most

cases, the high- and low-resolution results differed by less than 5%. In one case, the difference was about 9% (see Fig. 5.12).

Moreover, these results are only useful if the body is in a steady state such that the thermal state of the body, and hence the net Yarkovsky force vector, are periodic functions of the true anomaly. In order to achieve this thermal condition, the simulation must run during an adequate warmup period. Based on experiments, it was found that a single orbit was sufficient to warm up the calculation when the body's initial temperature was uniform at the appropriate effective temperature. About 5% of the cases in Chapter 5 were chosen at random and recomputed using a warmup period of two orbits. In all cases, the long- and short-warmup results differ by 1% or less.

4.2.2 Comparison with other approaches

Pure Diurnal Effect, Circular Orbit

Peterson (1976) developed an analytical theory of the pure diurnal ($\iota = 0$ or π) Yarkovsky effect with various assumptions discussed in Chapter 2. In Fig. 4.6, I compare the finite-difference calculations with Peterson's analytical results for a 1-m body spinning with a 5-h period. The input parameters are exactly analogous to Peterson's. The properties of the body are identical to those used by Peterson for stony material: $\rho = 2500$ kg m^{-3}, $k = 1.5$ W m^{-1} K^{-1}, $c_p = 1000$ J kg^{-1} K^{-1}, $\epsilon = 1$, $\Lambda = 0$. The general calculation produces semimajor axis decay that is systematically slower than Peterson's by about 10%, but the overall trend is in reasonable agreement for this case, in which his assumptions are applicable.

Pure Seasonal Effect, Circular Orbit

The pure seasonal Yarkovsky effect was evaluated analytically by Rubincam (1995, Rubincam (1998) by linearizing the radiative term in the boundary condition, as
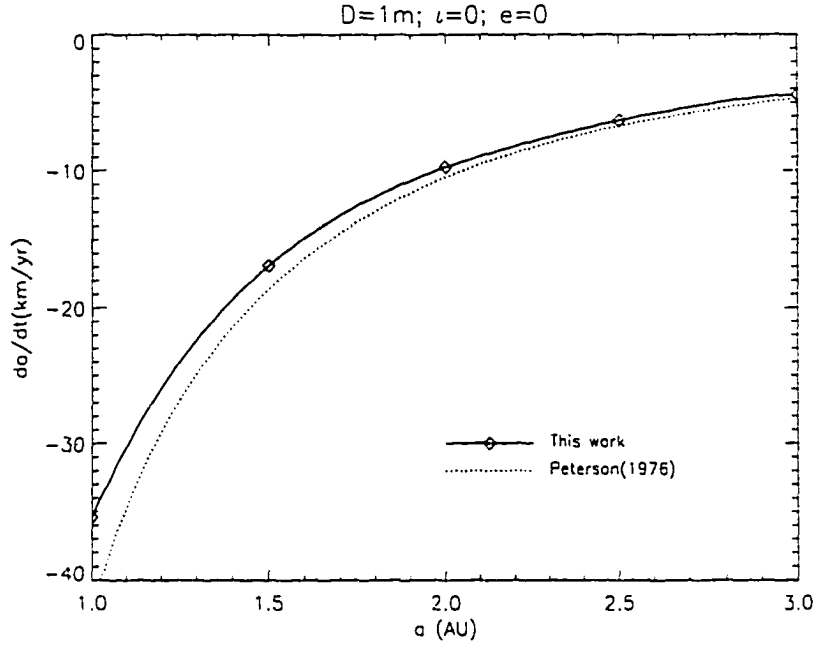
Figure 4.6: Comparison between results from the finite-difference calculation and those of Peterson (1976) for da/dt for a 1-m stony body with a 5-hr rotation period for the case $\iota = \pi$, resulting in a pure diurnal Yarkovsky effect. Diamonds indicate the numerical results, interpolated by the solid lines. The dotted curve is Peterson's result.

described in Chapter 3. Rubincam pointed out that his approach leads to an underestimate of the surface temperature asymmetry and an overestimate of the thermal lag angle so he applied an estimated correction factor of 0.75 to da/dt in order to correct for these effects. The finite-difference method was used to calculate da/dt for the case evaluated by Rubincam. The bodies studied had the same physical properties as used by Rubincam (1998) for stony material: $\rho = 3500$ kg m^{-3}, $k = 2.4$ W m^{-1} K^{-1}, $c_p = 750$ J kg^{-1} K^{-1}, $\epsilon = 1$, $\Lambda = 0$. However, while Rubincam assumed infinitely-fast rotation (in order to eliminate diurnal effects and show the pure seasonal effect), the numerical calculations are restricted to a finite rotation rate.

To test his results numerically, I considered various rotation periods to
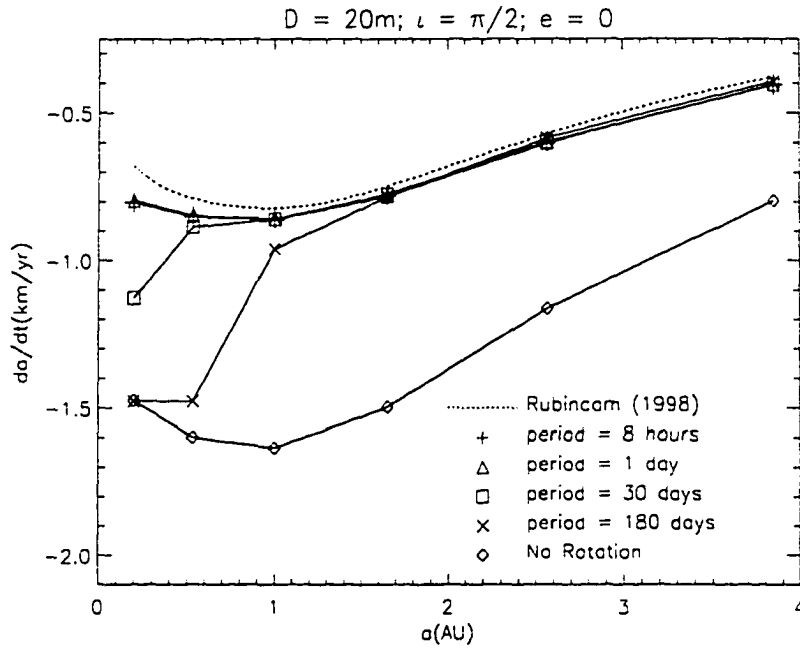
Figure 4.7: Rate of change of a as a function of rotation period for a 1-m stony body. For periods of about a day or faster, da/dt does not depend on the rotation period, permitting a comparison between the finite-rotation rate results and the infinite-rotation rate (pure seasonal) results of Rubincam (1998). Symbols indicate the computed results, connected by solid lines. The dotted curve is Rubincam's result.

see whether the results trend toward Rubincam's as the rotation rate is increased. Results for the case $\iota = \pi/2$, $e = 0$, $D = 20$m, were compared using various rotation periods. As shown in Fig. 4.7, within the range for a used here, the finite-difference results are independent of rotation rate for $a > 1$ AU for rotation periods less than about a day. In such a fast-rotation regime, those results differ from Rubincam's by about 5- to 10%, well within the expected margin of error for Rubincam's approach. Even for $A < 1$ AU, the trend with decreasing period is toward Rubincam's result.

In Fig. 4.8, the finite-difference calculation is compared with that of Rubincam (1998) for 1-, 10-, and 100 m bodies with $\iota = \pi/2$, $e = 0$, and $p = 5$hr. The finite-difference calculation produces semimajor axis decay that is faster than
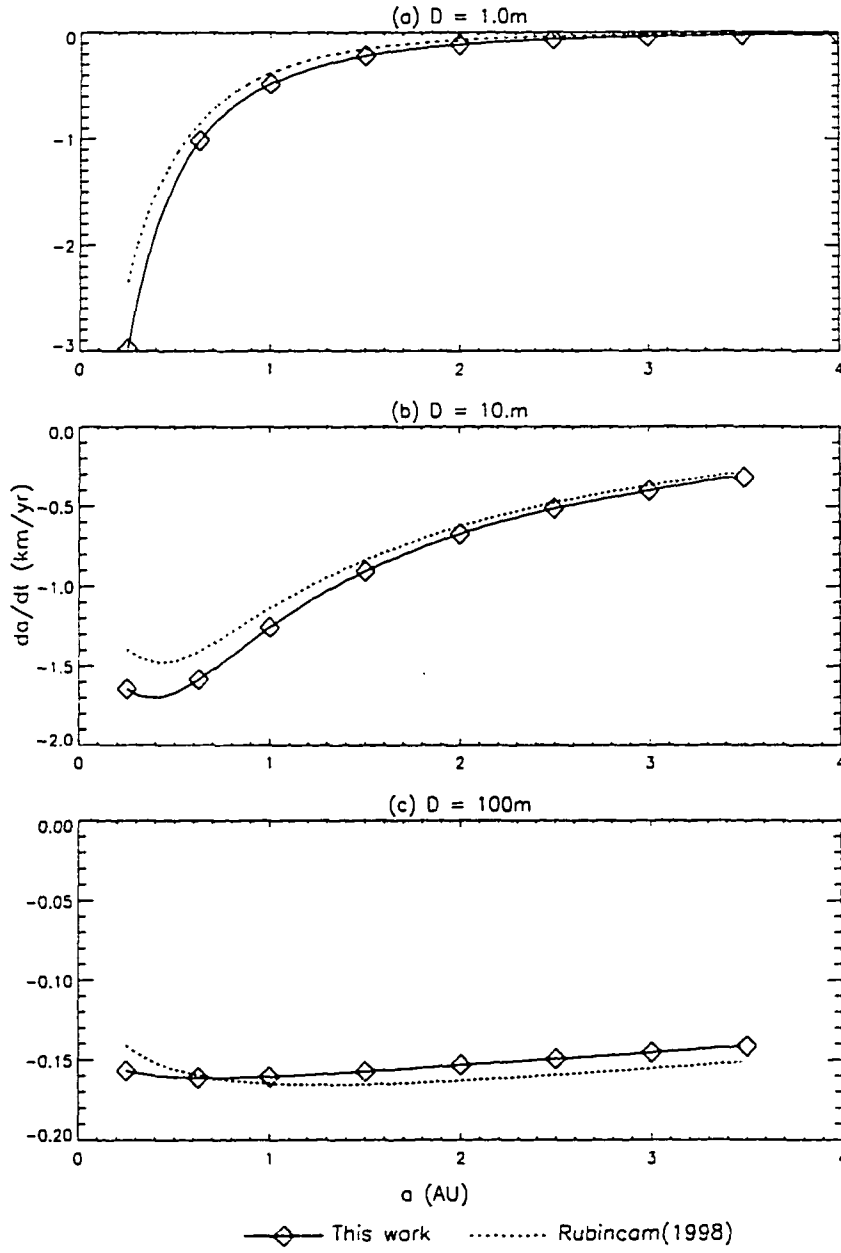
Figure 4.8: Comparison between the finite-rotation-rate (period = 5 h) results and the infinite rotation-rate (pure seasonal) results of Rubincam (1998) for da/dt for 1- 10- and 100-m stony bodies for the case $\iota = \pi/2$. Diamonds indicate the computational results, interpolated by the solid lines. The dotted curve is Rubincam's result.

Rubincam's by 20 – 40% for the 1-m body and around 10% for the 10-m body. For the 100-m body, the finite-difference calculation produces semimajor axis decay that is generally a few percent slower than Rubincam's, but the curves cross at about 0.6 AU. Based on a plane-parallel heat-flow approximation, Vokrouhlický and Farinella (1998) also reported that for 100-m bodies, Rubincam's formula yields faster semimajor axis decay than their nonlinearized theory, and they confirmed that his theory tends to underestimate the surface temperature asymmetry and overestimate the thermal lag angle. In all cases, the trends are in agreement between the finite-difference results and Rubincam's results. The qualitative differences probably reflect the acknowledged approximations involved in Rubincam's analytical approach. The magnitude of the disagreement is not significant for application to solar system problems.

4.3 Experiments with a modified algorithm

In order to treat additional cases with more realistic rotation rates, an attempt was made to reduce execution times by modifying the above scheme such that full rotation periods are sampled only occasionally throughout an orbit, assuming that the thermal state of the asteroid varies sufficiently gradually. In this modified scheme, the full heat equation was not solved at every single orbital timestep. Instead, the full procedure was performed for several rotations of the body and those results were used to extrapolate the thermal state to a somewhat later time. For conditions typical of the studies presented in this dissertation, the modified procedure was about five times faster than the original method. Averaged over all of the runs (high-eccentricity calculations tended to be less efficient) in the survey, the modified procedure was about twice as fast as the original method. The results of the modified calculation agreed with the original method to within about 10%. However, to avoid the possibility that the modified calculation would introduce artificial trends (e.g. rates of change as a function of eccentricity and semimajor axis) the results in this dissertation were computed using the slower original approach.

4.4 Generalization to ellipsoidal bodies

The ellipsoidal mesh is zoned similarly to the spherical mesh except that the central cell is allowed to be an ellipsoid and cell boundaries in the radial direction are nested ellipsoids. At the surface, the axes of these ellipsoids are uniformly spaced (i.e., all three axes of the first interior ellipsoid are exactly, say, 1 cm shorter than those of the ellipsoid that defines the surface) so that the surface cell thicknesses are as uniform as possible.

In the modified calculation, all of the assumptions regarding the shape of the body are confined to the zoning portion of the problem (i.e., where the body is divided into discrete cells). The thermal physics portion of the model was generalized so as to be portable eventually to arbitrary shape models. Toward that end, the following generalizations to the thermal physics were made:
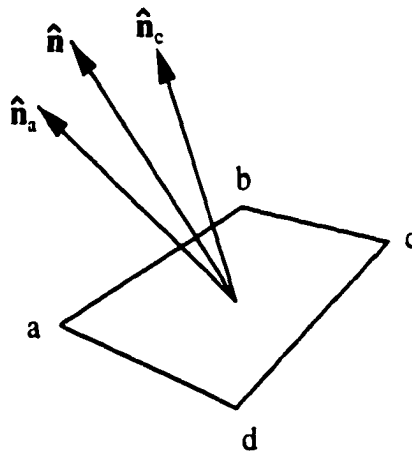
Figure 4.9: Geometry for the calculation of the normal vector on a surface cell of a non-spherical body

1) Surface normal vectors are computed numerically. In the original calculation, surface normals were assumed to be parallel to the position vector of the cell center, an assumption that is valid only for spherical bodies. In the modified calculation, because each surface cell has four vertices (two of which sometimes coincide), two

candidate surface normals are computed. To compute a candidate surface normal vector, a vertex is chosen, say vertex "a" in Fig. 4.9. The candidate surface normal $\mathbf{n}_a$ is computed as the cross product

$$\mathbf{n}_a = \vec{ab} \times \vec{ad}, \qquad (4.114)$$

where, for example, $\vec{ab}$ is the vector from vertex "a" to vertex "b". The other candidate surface normal is computed using the vertex that is opposite that used to compute the first candidate, in this case

$$\mathbf{n}_c = \vec{cb} \times \vec{cd}. \qquad (4.115)$$

To obtain a unique surface normal vector $\hat{n}$, the two candidate normal vectors, $\mathbf{n}_a$ and $\mathbf{n}_c$, are averaged and the result is normalized. This approach is adequate even for polar cells where two of the vertices coincide because one of the candidate surface normals will be the zero vector so the average will be parallel to the non-zero candidate vector.

2) In the spherical model, it was assumed that the heat flux $\mathbf{J}$ was normal to each cell face. That assumption was approximately correct for the discrete case and rigorously correct in the limit of infinitesimal cell dimensions. In order to allow for cells with more general shapes, this assumption has been removed. Instead the dot product in (4.107) is evaluated using cell face normals calculated using the same algorithm discussed above for computing surface normals.

3) In the spherical calculation, cell volumes were computed as differential spherical volume elements:

$$V = r^2 \Delta r \Delta \theta \Delta \phi. \qquad (4.116)$$

In the generalized thermal model, cell volumes are computed by dividing a cell into five tetrahedra and using the following formula (Uspensky, 1948) to find the volume

of each tetrahedron:

$$V_{\text{tetrahedron}} = \frac{1}{288} \begin{vmatrix} 0 & d_{12}^2 & d_{13}^2 & d_{14}^2 & 1 \\ d_{12}^2 & 0 & d_{23}^2 & d_{24}^2 & 1 \\ d_{13}^2 & d_{23}^2 & 0 & d_{34}^2 & 1 \\ d_{14}^2 & d_{24}^2 & d_{34}^2 & 0 & 1 \\ 1 & 1 & 1 & 1 & 0 \end{vmatrix}, \qquad (4.117)$$

where d_{ij} is the distance between vertex i and vertex j.

The ellipsoidal calculation has been validated to some extent by verifying that the results converge smoothly to those generated by the spherical calculation as the shape of a test body approaches that of a sphere.

Regarding the computational performance of the ellipsoidal code as compared to the spherical code, all of the additional computation performed in ellipsoidal calculation is performed once when the code initializes and the results are saved for use throughout the calculation. Therefore, for similar input data, the ellipsoidal code produces a somewhat larger memory image than the spherical code, but they consume essentially the same amount of processor time.

CHAPTER 5

SEMIMAJOR AXIS PERTURBATIONS

In this chapter, results are presented for the rates of change of semimajor axis caused by the general Yarkovsky effect in a survey of a parameter space spanning ranges of values for radius R, semimajor axis a, and eccentricity e, all with orbital inclination $i = 0$ and a 5-h rotation period. Note that this rotation period may be atypically slow (see Sec. 10), however shorter rotation periods require the timestep to be reduced and were considered too computationally expensive for this work. In this chapter, test bodies are assumed to be spherical and the thermal properties are identical to those used by Rubincam (1998) for stony material: density $\rho = 3500$ kg m^{-3}, thermal conductivity $k = 2.4$ W m^{-1} K^{-1}, heat capacity $c_p = 750$ J kg^{-1} K^{-1}, emissivity $\epsilon = 1$, bond albedo $\Lambda = 0$.

5.1 Pure Diurnal Effect, Noncircular Orbit

In this section, the pure diurnal effect ($\iota = 0$ or π) is investigated by varying the size, rotational sense (prograde/retrograde), semimajor axis, and eccentricity of test bodies rotating with a 5-h period. Figure 5.11 summarizes the results for da/dt for this wide range of cases.

Note in Fig. 5.11 that, for large values of e, da/dt is quite large, and a steep function of e. For example, for any size body, at 1 AU, the semimajor axis of an orbit with $e = 0.9$ evolves about 10 times more rapidly than for a nearly circular ($e = 0.1$) orbit, while at 3 AU this factor is closer to 50. The faster orbital evolution is probably the result of the stronger force that the body experiences near
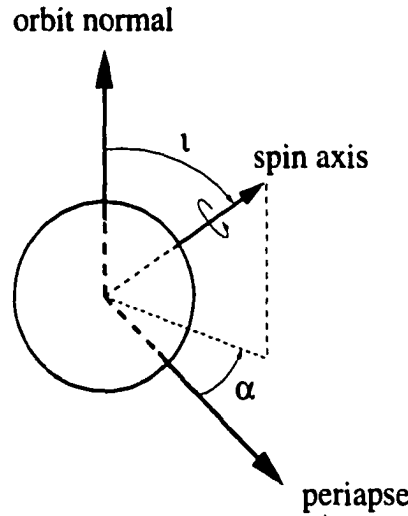
Figure 5.10: The spin axis orientation relative to the orbit is specified by two angles: ι and α. ι is the obliquity of the spin axis relative to the orbit normal and α is the angle between the periapse direction and the projection of the spin axis on the orbital plane.

pericenter, relative to the circular orbit. This effect competes with, but dominates, the fact that most of the orbital period is spent at heliocentric distances larger than a, where the force is weaker relative to the circular orbit.

This observation can be supported heuristically (at least for moderate eccentricities) by considering Peterson's form for the diurnal Yarkovsky force as a function of heliocentric distance (Peterson, 1976), which can be written

$$F(r) \simeq \psi \left(\frac{r}{a}\right)^{-7/2} , \qquad (5.118)$$

where ψ does not depend on r. This result was based on the assumption that the temperature distribution throughout the body at any heliocentric distance is that obtained in a body on a circular orbit of radius r. Actually, for a noncircular orbit, the true temperature distribution contains transients that are not accounted for by this simplification, so this assumption is probably only useful for small or moderate eccentricities. If the rotation period is much shorter than the orbital period, then for this case ($\iota = 0$ or π), the thermal lag angle, δ, can be considered
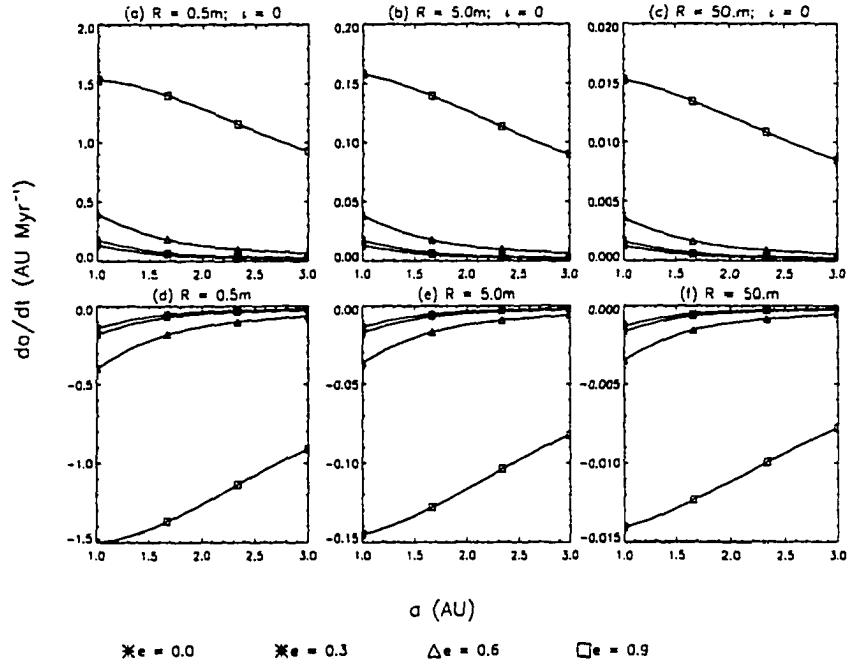
Figure 5.11: da/dt vs. a for $\iota = 0$ or π, $e = 0.1 - 0.9$, rotation period = 5 h. Symbols indicate the computed results, solid curves are interpolated. This configuration gives rise to the pure "diurnal" Yarkovsky effect. As expected, the da/dt curves for retrograde rotation ($\iota = \pi$) are nearly identical to those for prograde rotation ($\iota = 0$) except for a change in sign. The $1/R$ dependence of da/dt is obvious. Also, da/dt is quite large for orbits with large e.

to be roughly independent of the true anomaly, allowing the Yarkovsky force (5.118) to be decomposed (into radial and transverse components) as

$$R(r) \simeq \psi \cos \delta \left(\frac{r}{a}\right)^{-7/2} \tag{5.119}$$

$$B(r) \simeq \psi \sin \delta \left(\frac{r}{a}\right)^{-7/2},$$

The semimajor axis changes at a rate (Danby, 1992)

$$\frac{da}{dt} = \frac{2}{n}\left[R(r)\frac{e}{\sqrt{1-e^2}}\sin f + B(r)\frac{a\sqrt{1-e^2}}{r}\right], \tag{5.120}$$

where n is the mean motion and f is the true anomaly. Over an orbit, $R(r)\sin f$

averages to zero for any eccentricity and $|\langle B(r)/r \rangle|$ can be shown to increase monotonically at an increasing rate with e (see Appendix). From (5.120),

$$\left| \left\langle \frac{da}{dt} \right\rangle \right| = \frac{2a}{n} \sqrt{1 - e^2} \left| \left\langle \frac{B(r)}{r} \right\rangle \right|. \qquad (5.121)$$

For moderate e, this function increases monotonically with e in a manner qualitatively similar to the observed e-dependence in Fig. 5.11. If the r-dependence in Eq. 5.118 were considerably weaker ($F(r) \propto (r/a)^{-1/2}$, for example), then the increased force near periapse would not be strong enough to cause a net increase in $|\langle da/dt \rangle|$ during the relatively short time spent at heliocentric distances smaller than a. In that case, $|\langle da/dt \rangle|$ would decrease with increasing e. For larger e, this heuristic analysis is inadequate.

Other features of Fig. 5.11 can be interpreted physically:

1) When the body's rotation is reversed, da/dt has nearly identical values except that the sign is reversed. This near-antisymmetry exists because, for prograde/retrograde rotation, the angular motion of the sun in the sky, as seen from a fixed point on the surface of the body, is the sum/difference of the body rotation rate and the orbital rotation rate. Since the rotation period is much shorter than the orbital period (except near periapse on high eccentricity orbits) the acceleration vectors for each case should nearly be reflections of one another about the radial line.

2) For fixed e, a, and ι, da/dt roughly scales inversely with the radius of the body. This behavior is consistent with all of the test bodies being in the same thermal regime (corresponding to the plane-parallel approximation). In this case, the rotation is fast enough that even the smallest body is affected only in a relatively thin surface layer. As a result, the surface temperature distribution, $T(\theta, \phi)$, is roughly the same for all sizes in the experiment. It is easy to show that, under this assumption, the Yarkovsky accelerations, and ultimately da/dt, must vary inversely with the radius of the body simply because of the size dependences of surface area and

volume. Any deviation from this size dependence is a reflection of the slight size dependence of the surface temperature distribution.

5.2 Cases of the General Yarkovsky Effect: $e \neq 0$, $\iota = \pi/2$

In this section, asteroid diameter D, semimajor axis a, eccentricity e and orientation α (see Fig. 5.10) are varied for test bodies with obliquity $\iota = \pi/2$, rotating with a 5-h period, whose properties are the same as those in the previous section. When e is small, the general calculation essentially reproduces the pure seasonal effect. However, for orbits with higher eccentricity, more general effects are observed which are not necessarily due to purely seasonal forcing, because of the finite rotation rate used here. Figure 5.12 summarizes the results for da/dt. Four orientations for α - 0, $\pi/4$, $\pi/2$, $3\pi/4$ - were investigated. Four other orientations correspond to reversing the rotation rates and it is expected that the results will be identical except that the inclination changes, which are caused by the diurnal forcing (and not presented in this chapter), will be opposite.

A number of interesting features in Fig. 5.12 call for some discussion:

1) In plots (j), (k), and (l) of Fig. 5.12, da/dt changes sign, becoming large and positive for orbits with large e and small a. This behavior is associated with the finite (as opposed to infinite) rotation rate used in the calculation. Near periapse, the angular motion of the sun in the sky becomes comparable to the rotation rate. Relative to the infinitely fast rotation case, the incident energy is redistributed such that, instead of being spread uniformly over lines of constant latitude, it is concentrated somewhat on the day side. This "hot spot" causes the force vectors to be more radial near periapse. Very close to periapse, this reduces whatever prograde or retrograde components may be present. Further from periapse, force vectors become more retrograde as the body approaches periapse and more prograde as the body recedes from periapse. The net effect on da/dt depends on a and e in a complicated way, but for this case, in which $\alpha = 3\pi/4$, the strongest retrograde

$$\iota = \pi/2$$

$$a \ (AU)$$
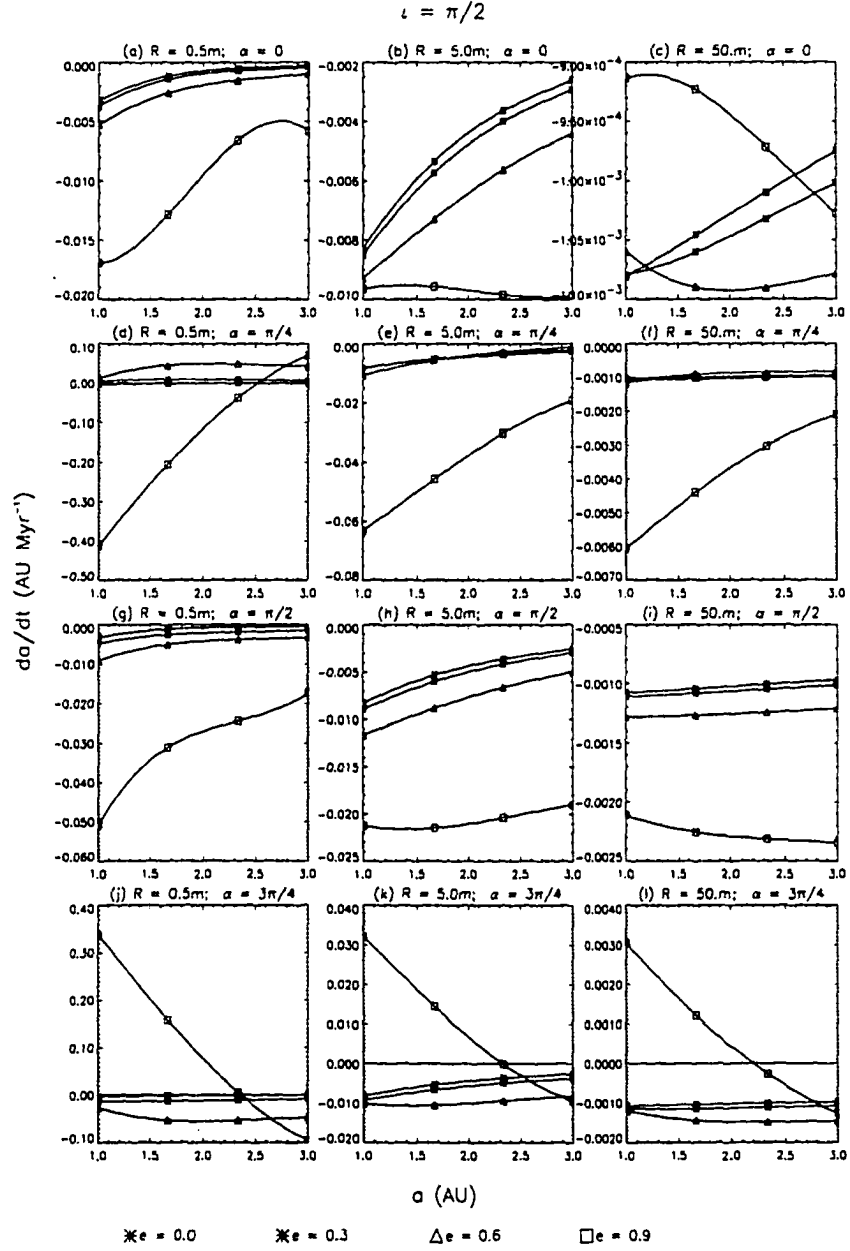
Figure 5.12: da/dt vs. a for $\iota = \pi/2$, $e = 0.1 - 0.9$, rotation period $= 5$ h. Symbols indicate the computed results, solid curves are interpolated. For small e, this configuration essentially yields the pure "seasonal" Yarkovsky effect. However, because the rotation rate is not infinite, the effect is more complicated for larger e. The point in (a) highlighted with a large diamond produced a 9% discrepancy when recomputed using a higher resolution and shorter timestep. This example is the largest discrepancy found in this work.

components should occur near periapse (for infinitely fast rotation), but they are reduced by the effect of the hot spot, allowing prograde forces from other parts of the orbit to dominate the semimajor axis evolution. Note that the magnitude of this effect should depend strongly on the rotation rate of the body. An analogous effect is seen in the $\alpha = \pi/4$ case (plots (d), (e), and (f) of Fig. 5.12).

2) In plots (b) and (c) of Fig. 5.12, $|da/dt|$ begins to decrease at small a for orbits with large e. The behavior is most pronounced for the 100-m body and not apparent for the 1-m body. This result can be explained as follows.

To understand this behavior, first consider a circular orbit. The polar temperatures for a body on such an orbit with $\iota = \pi/2$ oscillate seasonally, reaching maximum values (hottest anywhere on the body ever) and minimum (coldest anywhere on the body ever) twice every orbit (near the times when the rotation axis points directly toward or axay fram the sun). This temperature variation launches seasonal heat pulses into the body. For this $e = 0$ case, one can think of two identical heat pulses with opposite phases, centered near the poles. The magnitude and direction of the Yarkovsky force can be related to the timing of the pulses. For orbits with small a, and hence short orbital periods, the heat pulses do not penetrate deeply, so smaller a (shorter orbital period) leads to a smaller net Yarkovsky force and hence smaller $|da/dt|$. For larger a and hence longer orbital periods, the heat pulses affect the entire body producing a larger net Yarkovsky force whose magnitude does not depend strongly on a. Moreover, for a given thermal inertia, the thermal lag angle increases as the orbital period is shortened, favoring an increase in $|da/dt|$ as a is decreased and more of the Yarkovsky force is directed along the orbital track. Finally, since the solar heating decreases with a, there is a tendency for the magnitude of the force also to be smaller with increasing a.

Now consider what happens for larger e (with $\alpha = 0$). As e is increased, one seasonal heat pulse becomes stronger and the other becomes weaker. Furthermore,

the strong pulse becomes narrower (i.e., it becomes more concentrated around periapse) and the weak pulse becomes wider. For a given a, e can be increased to such a value that, although the body at this a with $e = 0$ would have a large Yarkovsky force vector because it is completely affected by the seasonal heat pulse, the strong heat pulse is too short to significantly penetrate the body so the magnitude of the force decreases. In other words, for a given a at which the body is penetrated by the $e = 0$ seasonal heat pulses, a value of e exists, above which the strong solar heating at periapse only affects a surface layer. This threshold value of e should increase with a and decrease with the size of the body, consistent with the trends in the figure.

3) The curious behavior (non-monotonic dependence of da/dt on a) in plots (g), (h), and (i) of Fig. 5.12 is difficult to explain, but given the various effects that contribute to the semimajor axis evolution in a complicated way, it is not surprising that they would conspire to produce the observed trends.

5.3   Cases of the General Yarkovsky Effect: $e \neq 0$, $\iota = 3\pi/4$

In the previous section, it was seen that, for $\iota = \pi/2$, the finite rotation rate produced effects that are more general than those produced in the case of infinitely-fast rotation. In this section I examine cases with finite rotation rate ($p = 5$ h) and an intermediate obliquity ($\iota = 3\pi/4$). The body properties are the same as in the previous sections. Figure 5.13 summarizes the results for da/dt. Four orientations for α (0, $\pi/4$, $\pi/2$, $3\pi/4$) were investigated. The other orientations, α, and opposite obliquity ($\iota = \pi/4$) were not investigated, but are expected to give qualitatively similar results (with a change of sign for the opposite obliquity cases).
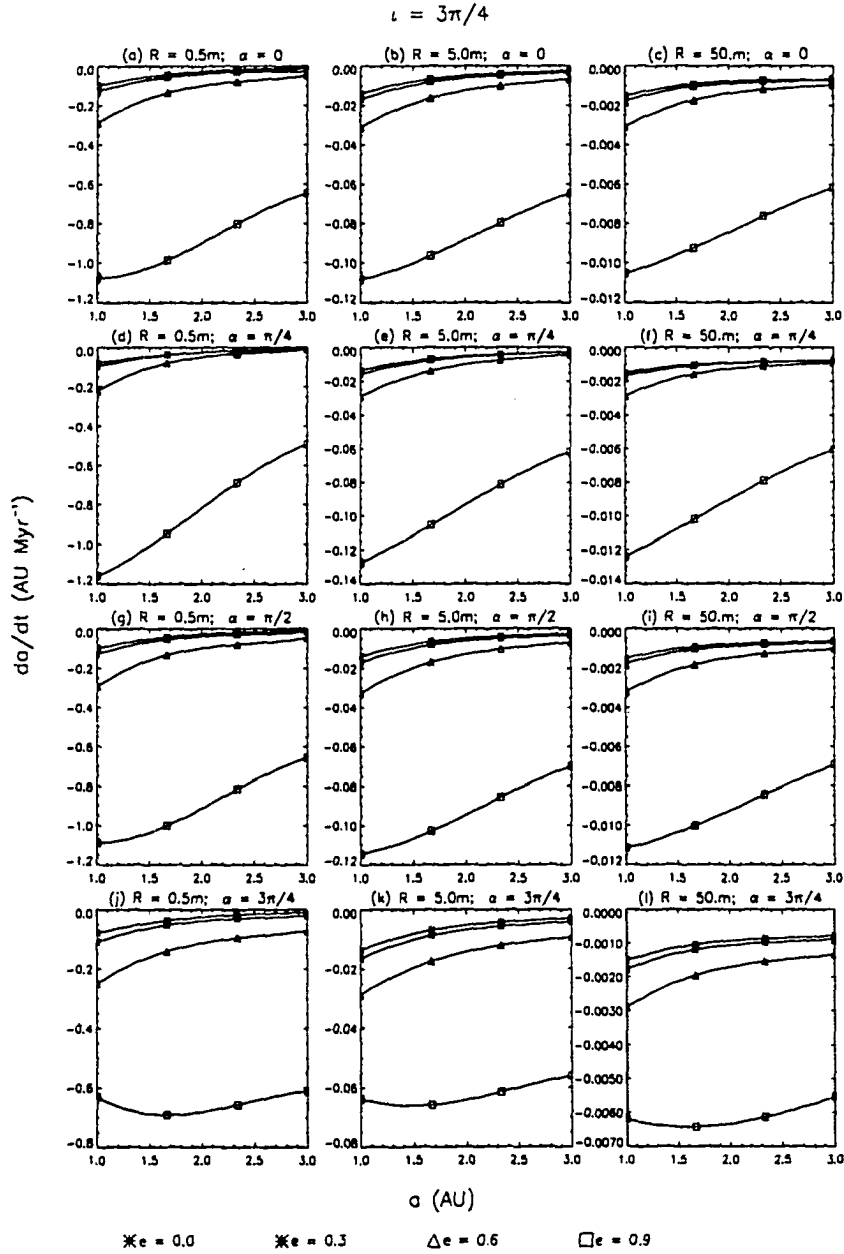
Figure 5.13: da/dt vs. a for $\iota = 3\pi/4$, $e = 0.1 - 0.9$, rotation period = 5 h. Symbols indicate the computed results, solid curves are interpolated. This configuration corresponds to neither the pure diurnal nor the pure seasonal approximation, but the results are roughly consistent with a suitable linear combination of the $\iota = 0$ or π and $\iota = \pi/2$ results from previous figures (see Fig. 5.14).

Figure 5.14: (following page) The linear superposition of "diurnal" and "seasonal" endmember components can approximate the results of the general calculations. For a range of body sizes (D), semimajor axes (a), and eccentricities (e), the results of the general calculations (solid curves) are compareded with results obtained using Eq. 5.122 (dotted curves), where the diurnal approximation (Fig. 5.11 (d), (e), and (f); $\iota = \pi$) is combined with the seasonal approximation (Fig. 5.12 (j), (k), and (l); $\iota = \pi/2$, $\alpha = 3\pi/4$). Symbols indicate the computed results, curves are interpolated. Agreement is close for smaller bodies with larger a and smaller e. The superposition approximation is worst for cases of large e and small a because temperature excursions in the body are the most severe for those cases.

(a) D = 1.0m

(b) D = 10.m

(c) D = 100m

a (AU)

∗e = 0.1   ◇e = 0.3   △e = 0.5   □e = 0.7   ×e = 0.9

———— Computed   ·············· Linear Combination
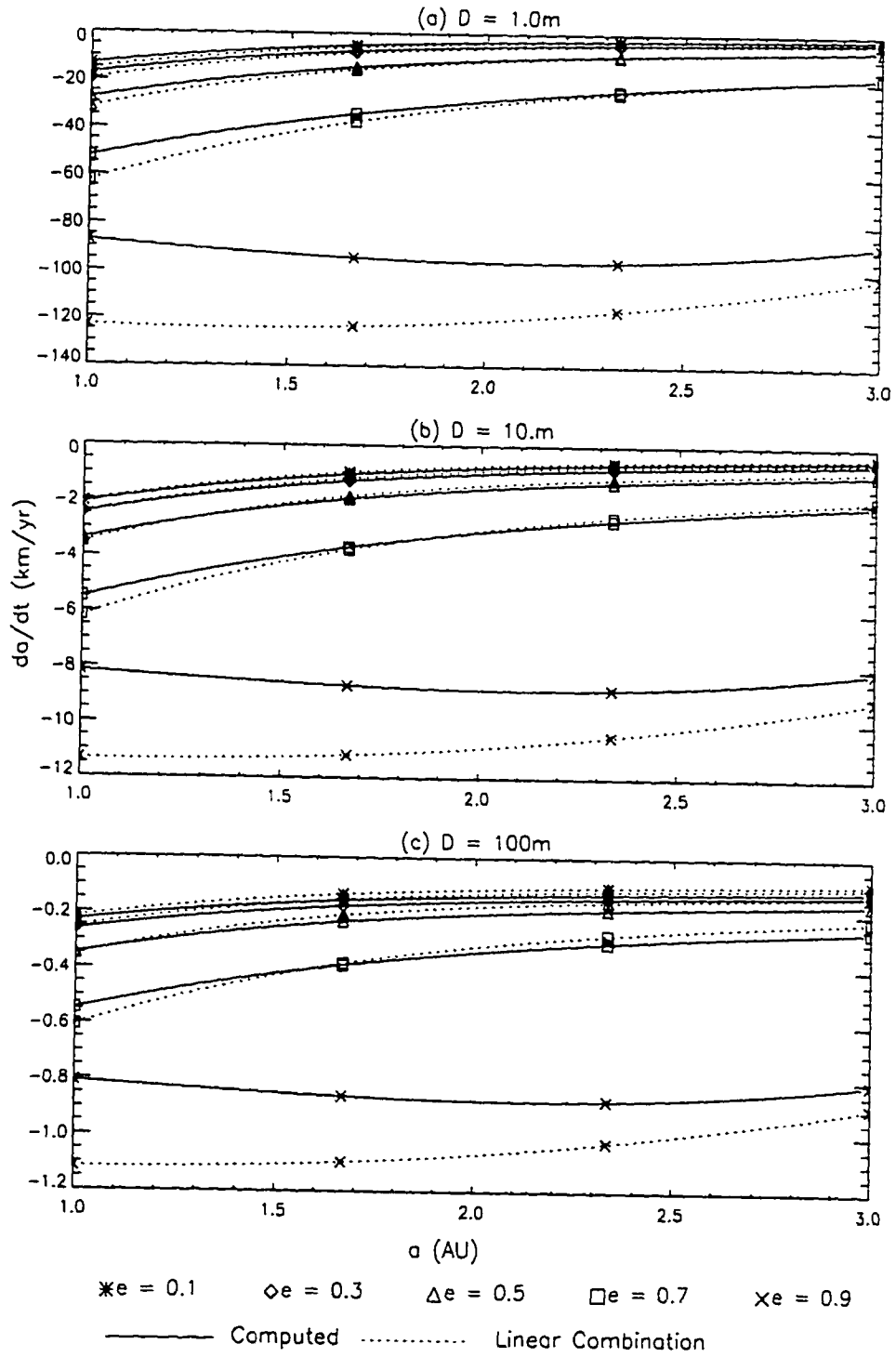
The results in Fig. 5.13 are roughly consistent with what one would obtain from a linear combination of my results for the pure diurnal and pure seasonal extremes (from Sec. 5.1 and 5.2, respectively) using coefficients that are consistent with the theories of Öpik (1951) and Rubincam (1987); i.e.,

$$\frac{da}{dt} = \cos\iota \left.\frac{da}{dt}\right|_{diurnal} + \sin^2\iota \left.\frac{da}{dt}\right|_{seasonal}. \tag{5.122}$$

Such a linear superposition is not strictly valid however, because the radiative term in the boundary condition makes the problem nonlinear. The nonlinear effects become significant for cases where temperature excursions in the body are large. That condition occurs for highly noncircular orbits and slowly rotating bodies. To demonstrate that effect, Fig. 5.14 shows a comparison between the direct general calculations and the linear superposition (Eq. 5.122) where the diurnal contribution is from Fig. 5.11 (d), (e), and (f) and the seasonal contribution is from Fig. 5.12 (j), (k), and (l). As expected, the linear combination works well for small e, where temperature excursions are small, but not as well for larger e and small a, where temperature excursions are large.

5.4 Discussion

Using the numerical approach developed in Chapter 4, I have presented the results of a fairly coarse survey of the Yarkovsky effect on small stony bodies throughout a parameter space spanning ranges of values for semimajor axis, eccentricity, spin axis direction, and size. da/dt is the strongest effect, but de/dt can also be fairly strong. $d\varpi/dt$ is a smaller effect, which may be important only on timescales longer than that for collisional reorientation of the spin vector. In this chapter, I have presented the results for da/dt. The next chapter will focus on changes in other orbital elements.

In this chapter, only homogeneous bodies were considered and it was assumed that the dependence of thermal diffusivity on temperature is not important.

These assumptions may be valid for small (1- to 10 m) bodies, but larger bodies are likely to possess a regolith and possibly even a porous interior. The finite-difference code is designed to handle a realistic calculation of the Yarkovsky effect on inhomogeneous bodies, in which two or more layers with differing thermal properties and a temperature-dependent thermal diffusivity are treated. Such a study is the topic of Chapter 7.

CHAPTER 6

ECCENTRICITY AND PERICENTER PERTURBATIONS

In this chapter, results are presented for de/dt and $d\varpi/dt$ caused by the Yarkovsky effect in a survey of a parameter space spanning ranges of values for a body's radius R, semimajor axis a, and eccentricity e. Inclination changes were not studied in this survey because orbital precession caused by secular perturbations from the planets would likely prevent the accumulation of significant long-term changes. Secular perturbations should also be considered when applying the orbitally-averaged eccentricity changes computed here to the solar system, but long-term eccentricity changes may still accumulate in the presence of such perturbations so it is worthwhile to address those changes here.

As in Chapter 5, test bodies are assumed to be spherical with a rotation period of 5 h and the thermal properties are identical to those used by Rubincam (1998) for stony material: density $\rho = 3500$ kg m^{-3}, thermal conductivity $k = 2.4$ W m^{-1} K^{-1}, heat capacity $c_p = 750$ J kg^{-1} K^{-1}, emissivity $\epsilon = 1$, bond albedo $\Lambda = 0$. The orbital inclination is zero in all cases. This survey differs from that of the previous chapter in that it covers a broader range of eccentricities – 0.0001 to 0.9001. This range is appropriate for most asteroids. For orbits with smaller eccentricity, a different set of variables would be required (see Appendix D).

6.1 Cases with $\iota = 0$ or π

Figures 6.15 and 6.16 summarize the results for the pure "diurnal" case: prograde and retrograde rotation states with the spin axis perpendicular to the orbit

plane ($\iota = 0$ or π, respectively). For $e = 0.0001$, large changes in ϖ corresepond to negligible variation in the actual orbit so $d\varpi/dt$ is thus not useful. Therefore results for cases with $e = 0.0001$ are not included in any of the plots for $d\varpi/dt$ (e.g. Fig. 6.16).

For very small e, de/dt is also very small, as shown in Fig. 6.15. This result can be understood from the following physical considerations. If e is very small, the Yarkovsky acceleration components (tangential and radial) are nearly constant throughout the orbit, yet the effects of those accelerations are are opposite on opposite sides of the orbit. For example, a prograde tangential acceleration at pericenter increases e, while such a force at apocenter decreases e. This behavior is represented by the $F_t(\cos E + \cos f)$ term in Eq. (D.228). Therefore the net effect on e is small.

For larger e, the trends can also be interpreted physically. Because the Yarkovsky acceleration is strongly dependent on distance from the sun (Peterson, 1976), what happens near pericenter is most important. Also, at pericenter, de/dt depends only on the tangential component of the disturbing acceleration. If the obliquity is near zero, the tangential component is prograde yielding positive de/dt, in agreement with Fig. 6.15. Similarly, for retrograde rotation ($\iota = \pi$), $de/dt < 0$, as shown. This discussion shows why the eccentricity evolution is faster for higher eccentricity orbits (see also Vokrouhlický (1998)).

Rates of change of e can be fast. For a meter-scale body, de/dt can be about 0.1 per million years. Note however that Δe can only accumulate at such rates as long as the rotation remains appropriate. This issue is addressed further in Chapter 10.

For given e, a, and ι, de/dt and $d\varpi/dt$ are found to scale roughly inversely with the radius of the body, according to Figs. 6.15 and 6.16. The explanation for this behavior is the following (see also Chapter 5): The diurnal thermal pulse affects a surface layer of characteristic depth $l \sim \sqrt{\kappa p}$, where κ is the thermal diffusivity

and p is the rotation period. For the thermal properties and rotation period used in this study, l is about 13 cm, so even for the smallest bodies ($R = 0.5$ m), the thermal pulse penetrates only a fraction of the radius during the relevant forcing period. Therefore, lateral thermal gradients are small and the temperature solution behaves as if it were a plane-parallel surface. That is, lateral heat conduction is not important and the problem could have been adequately treated in one-dimension, where the heat equation is solved independently as a function of depth below each location on the surface. In that approximation, the surface temperature distribution (i.e., $T(\theta, \phi)$) would be independent of body size. Integrating over the surface, the net Yarkovsky acceleration is given by the total force (which scales with the surface area, $\propto R^2$) divided by the total mass, (which scales with the volume, $\propto R^3$), yielding a dependence net dependence on $1/R$. The orbital element rates of change given by Eq. (D.227) – (D.230) inherit the $1/R$ dependence because they are linear in the Yarkovsky acceleration components.

As shown in Fig. 6.15, de/dt is nearly independent of a reversal of the spin; only the sign of de/dt changes. This result follows from the fact that reversing the rotation results in a nearly identical surface temperature distribution, except that it is reflected about the radial line. The tangential acceleration component is reversed while the radial component remains essentially unchanged. For this configuration, the radial and tangential acceleration components throughout the orbit are symmetric about the major axis for all e. Radially outward acceleration components cause an instantaneous increase in e during the outbound period of the orbit and an instantaneous decrease in e during the inbound portion, as represented by the $F_r \sin f$ term in Eq. (D.228). Hence, because of the symmetry, any instantaneous Δe during the outbound portion of the orbit is cancelled by an equal and opposite Δe imparted during an equal Δt on the inbound portion of the orbit, so the effect of radial acceleration components on e averages to zero and they are not important in changing the eccentricity. On the other hand, referring to the $F_t(\cos E + \cos f)$ term in Eq. (D.228), prograde(retrograde) tangential accelerations tend to cause an instantaneous increase(decrease) in e near periapse(apoapse), but an instantaneous

decrease(increase) in e near apoapse(periapse). Because of the symmetry, any given Δe during the outbound portion of the orbit is reinforced by an equal Δe imparted during an equal Δt on the inbound portion of the orbit. Therefore, the sign of de/dt is controlled by the sign of the tangential acceleration and reversing the rotation rate reverses the sign of de/dt.

Similarly, as shown in Fig. 6.16, $d\varpi/dt$ is invariant with respect to a reversal of the spin. The explanation is analogous to that given in the previous paragraph, except that instantaneous changes in ϖ produced by tangential accelerations average to zero over an orbit, while changes produced by radial accelerations tend to reinforce (notice in Eq. (D.230) that F_r is multiplied by $\cos f$ and that F_t is multiplied by $\sin f$ instead of visa versa as was the case for de/dt). Since the radial acceleration components remain essentially unchanged under a reversal of the spin direction, $d\varpi/dt$ remains essentially unchanged as well.
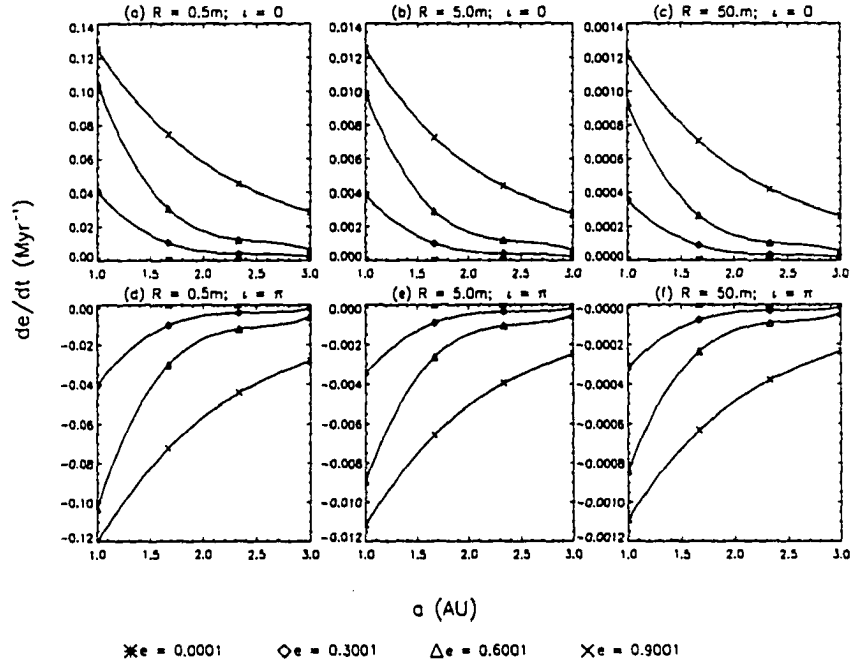
Figure 6.15: Rate of change of orbital eccentricity, de/dt vs. a for cases with the spin axis normal to the orbital plane. Six graphs are shown, for three radii ($R = 0.5, 5.0, 50.0$ m) and two obliquities ($\iota = 0$ top row, π bottom row). With these obliquities, this is a pure "diurnal" Yarkovsky effect. On each graph, four curves represent cases with $e = 0.0001, 0.3001, 0.6001,$ and 0.9001. In all cases, $i = 0$ and rotation period $= 5$ h. Symbols indicate computed results; solid curves are interpolated. As expected, the de/dt curves for retrograde rotation ($\iota = \pi$) are nearly identical to those for prograde rotation ($\iota = 0$) except for a change in sign. Note de/dt is roughly inversely proportional to R if other parameters are held constant.
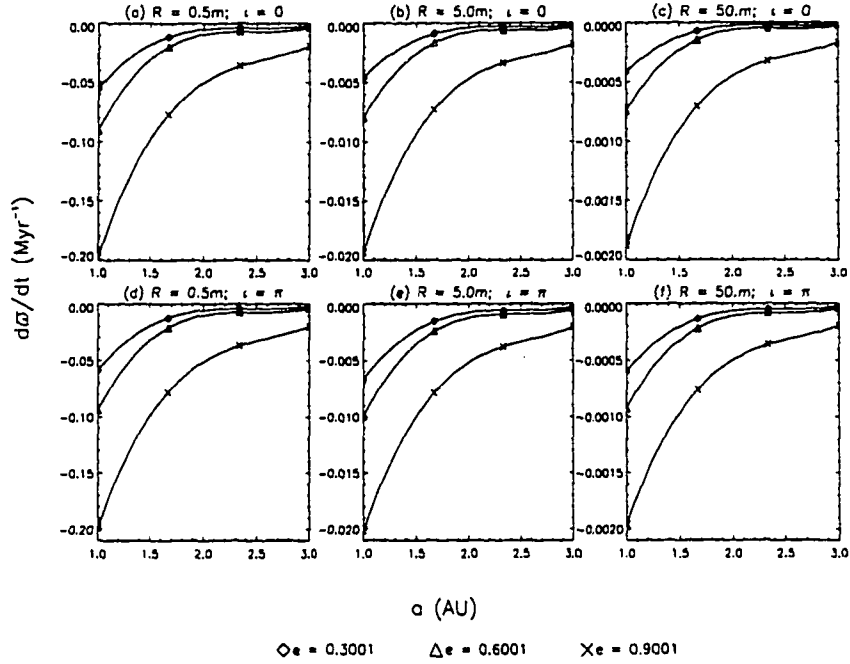
Figure 6.16: Rate of change of pericenter longitude, $d\varpi/dt$ vs. a for the cases shown in Fig. 6.15, all a pure diurnal Yarkovsky effect. Note that the $d\varpi/dt$ curves for retrograde rotation ($\iota = \pi$) are nearly identical to those for prograde rotation ($\iota = 0$), and that $d\varpi/dt$ has a $1/R$ dependence, as explained in the text.

Figure 6.17: (following page) de/dt vs. a for cases with $\iota = \pi/2$. Twelve graphs are shown, for three radii ($R = 0.5, 5.0, 50.0$ m) and four spin axis orientations ($\alpha = 0$ top row, $\pi/4$ second row from top, $\pi/2$ third row from top, $3\pi/4$ bottom row). Four other spin axis orientations, α, correspond to reversing the rotation and were not studied, but, as described in the text, those results are expected to be identical to the those presented here. On each graph, four curves represent cases with $e = 0.0001, 0.3001, 0.6001$, and 0.9001. In all cases, $i = 0$ and rotation period $= 5$ h. Symbols indicate the computed results, solid curves are interpolated. For small e, this configuration essentially yields a pure "seasonal" Yarkovsky effect. However, because the rotation rate is not infinite, the effect is more complicated for larger e.

$\iota = \pi/2$

(a) R = 0.5m; α = 0   (b) R = 5.0m; α = 0   (c) R = 50.m; α = 0

(d) R = 0.5m; α = π/4   (e) R = 5.0m; α = π/4   (f) R = 50.m; α = π/4

(g) R = 0.5m; α = π/2   (h) R = 5.0m; α = π/2   (i) R = 50.m; α = π/2

(j) R = 0.5m; α = 3π/4   (k) R = 5.0m; α = 3π/4   (l) R = 50.m; α = 3π/4

de/dt (Myr^{-1})

a (AU)

✳ e = 0.0001   ◇ e = 0.3001   △ e = 0.6001   ✕ e = 0.9001
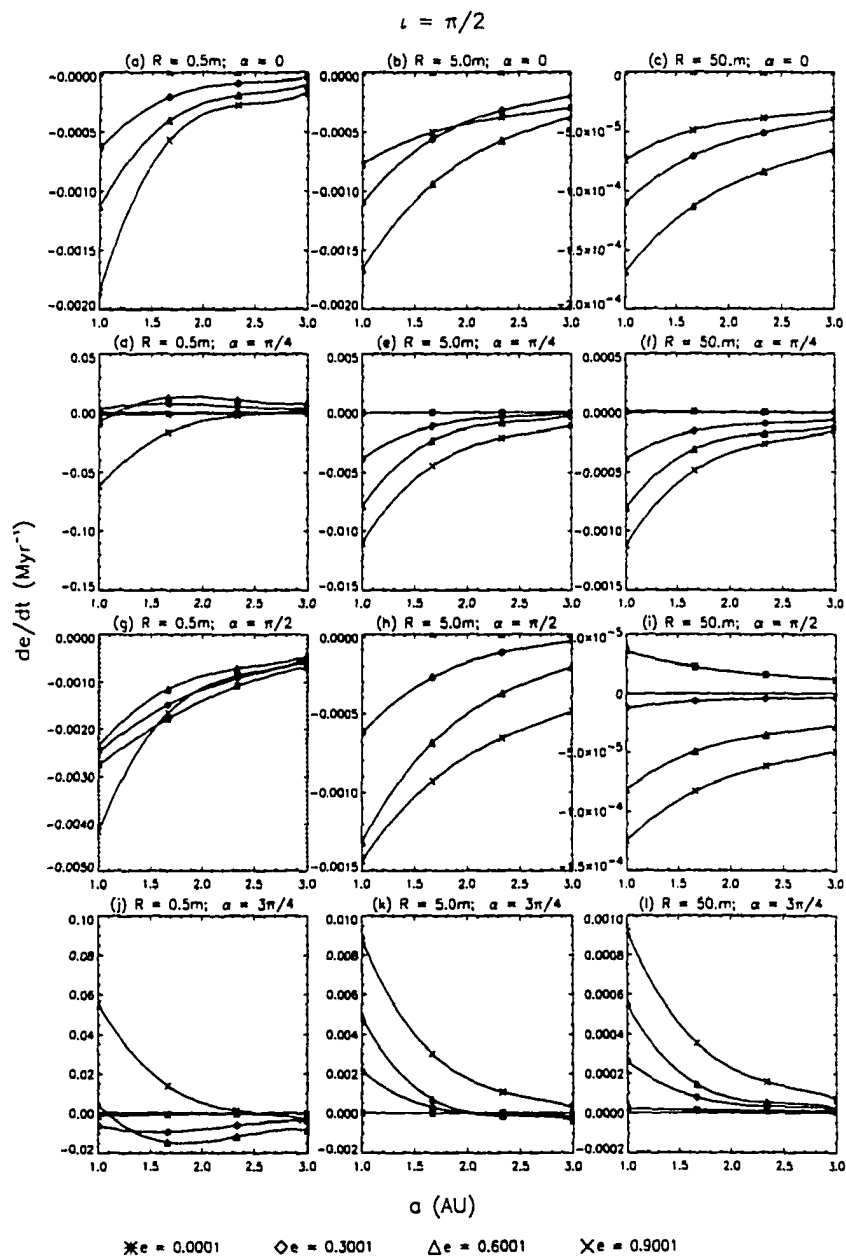
6.2 Cases with $\iota = \pi/2$

Figures 6.17 and 6.18 summarize the results for cases with $\iota = \pi/2$, i.e., where the spin axis lies in the orbit plane. Four orientations α (see Fig. 5.10) were examined: $\alpha = 0, \pi/4, \pi/2, 3\pi/4$.

If the rotation rate were infinite, cases with $\iota = \pi/2$ would correspond to conditions for a pure "seasonal" Yarkovsky effect. However, because here the rotation rate is finite, surface temperatures are not so completely smeared out as to be perfectly longitude-independent, so there is some diurnal component to the temperature distribution. Thus, having $\iota = \pi/2$ is not formally equivalent to the pure seasonal extreme.

Nevertheless, in some of the cases presented here, the diurnal contribution to changes in the in-plane elements is negligible, and the result is effectively seasonal. Those cases are the ones where the rotation rate is everywhere fast compared to the instantaneous motion of the sun in the sky. Such cases have small e and larger a. Thus, for examples in Figs. 6.17, and 6.18, for $e = 0.0001$ and a near maximum, the effect is essentially purely seasonal so an increase in the rotation rate should have little effect on the results. For larger e, near periapse, the orbital motion is relatively fast, so there the Yarkovsky acceleration is considerably different than one would obtain using the assumption of infinitely fast rotation. Therefore, as e increases, the results for changes in the in-plane elements (Figs. 6.17 and 6.18) diverge from those for the pure seasonal case, particularly for the cases in the survey with smaller a.

For this obliquity, reversing the spin should have no effect on the seasonal contribution. For the diurnal contribution, reversing the spin should change the sign of the out-of-plane acceleration, leaving the in-plane acceleration unchanged. Therefore, rates of change of the in-plane elements, e and ϖ should not be affected. Thus, there was no need to compute the cases corresponding to a spin reversal (i.e., $\alpha = \pi, 5\pi/4, 3\pi/2, 7\pi/4$). The results would be identical to those for $\alpha =$
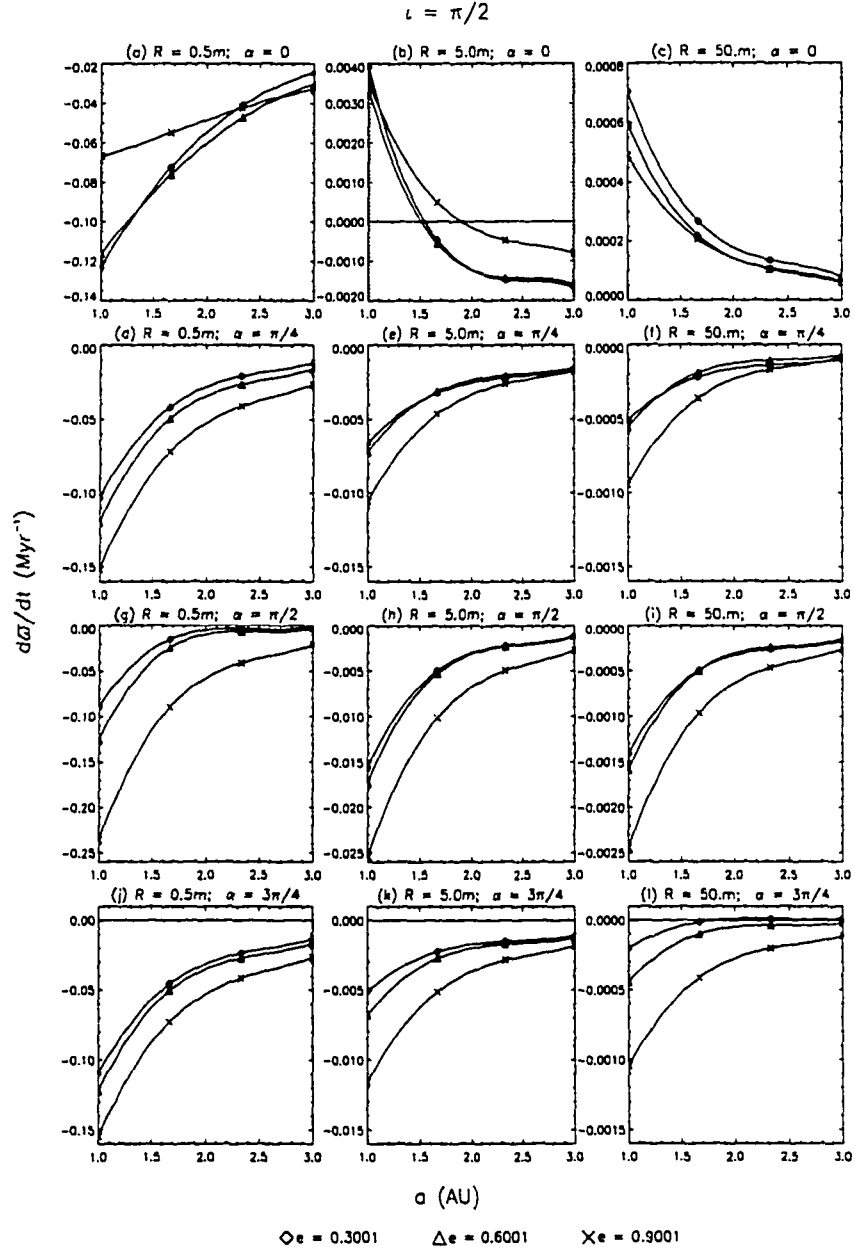
Figure 6.18: $d\varpi/dt$ vs. a for the cases shown in Fig. 6.17. For cases with small e, these results should approximate those caused by the pure seasonal Yarkovsky effect fairly well. For the cases $\alpha = \pi, 5\pi/4, 3\pi/2, 7\pi/4$, corresponding to a reversal of rotation and not computed in this study, but the results should be the same.

$0, \pi/4, \pi/2$, and $3\pi/4$, respectively.

Except where $\alpha = 0$, de/dt and $d\varpi/dt$ each show a dependence on size of $\sim 1/R$ (see Figs. 6.17 and 6.18). For de/dt and $d\varpi/dt$ (Figs. 6.17 and 6.18), the relation is least apparent for the 1-m bodies because they are most thoroughly affected by the seasonal thermal wave (which penetrates to a characteristic depth of about 5 m for $a = 1$ AU for the thermal properties used in this study), causing their surface temperatures to deviate most substantially from those that would be obtained using the plane-parallel approximation. For the cases with $\alpha = 0$, the two intervals of the orbit during which the pole is pointed directly toward or away from the sun are extreme relative to the $\alpha \neq 0$ cases, being long near apoapse and short near periapse. The highly-asymmetric thermal wave penetrates deeply near apoapse and shallowly near periapse relative to the somewhat more symmetric wave experienced by the bodies with $\alpha \neq 0$, so significantly different behavior is not surprising.

Figure 6.19: (following page) de/dt vs. a for cases with $\iota = 3\pi/4$. Twelve graphs are shown, for three radii ($R = 0.5, 5.0, 50.0$ m) and four spin axis orientations ($\alpha = 0$ top row, $\pi/4$ second row from top, $\pi/2$ third row from top, $3\pi/4$ bottom row). On each graph, four curves represent cases with $e = 0.0001, 0.3001, 0.6001$, and 0.9001. In all cases, $i = 0$ and rotation period = 5 h. Symbols indicate the computed results, solid curves are interpolated. This configuration corresponds to neither the pure diurnal nor the pure seasonal approximation, but the results are roughly consistent with a suitable linear combination of the $\iota = 0$ or π and $\iota = \pi/2$ results from Figs. 6.15 and 6.17 respectively. For the cases $\alpha = \pi, 5\pi/4, 3\pi/2, 7\pi/4$, corresponding to a reversal of rotation and not computed in this study, reasonable approximations may be obtained using the above linear combination procedure and substituting the diurnal component corresponding to $\iota = 0$.

$\iota = 3\pi/4$

(a) R = 0.5m; α = 0   (b) R = 5.0m; α = 0   (c) R = 50.m; α = 0

(d) R = 0.5m; α = $\pi/4$ (e) R = 5.0m; α = $\pi/4$ (f) R = 50.m; α = $\pi/4$

(g) R = 0.5m; α = $\pi/2$ (h) R = 5.0m; α = $\pi/2$ (i) R = 50.m; α = $\pi/2$

(j) R = 0.5m; α = $3\pi/4$ (k) R = 5.0m; α = $3\pi/4$ (l) R = 50.m; α = $3\pi/4$

de/dt (Myr^{-1})

a (AU)

✳e = 0.0001   ◇e = 0.3001   △e = 0.6001   ✕e = 0.9001
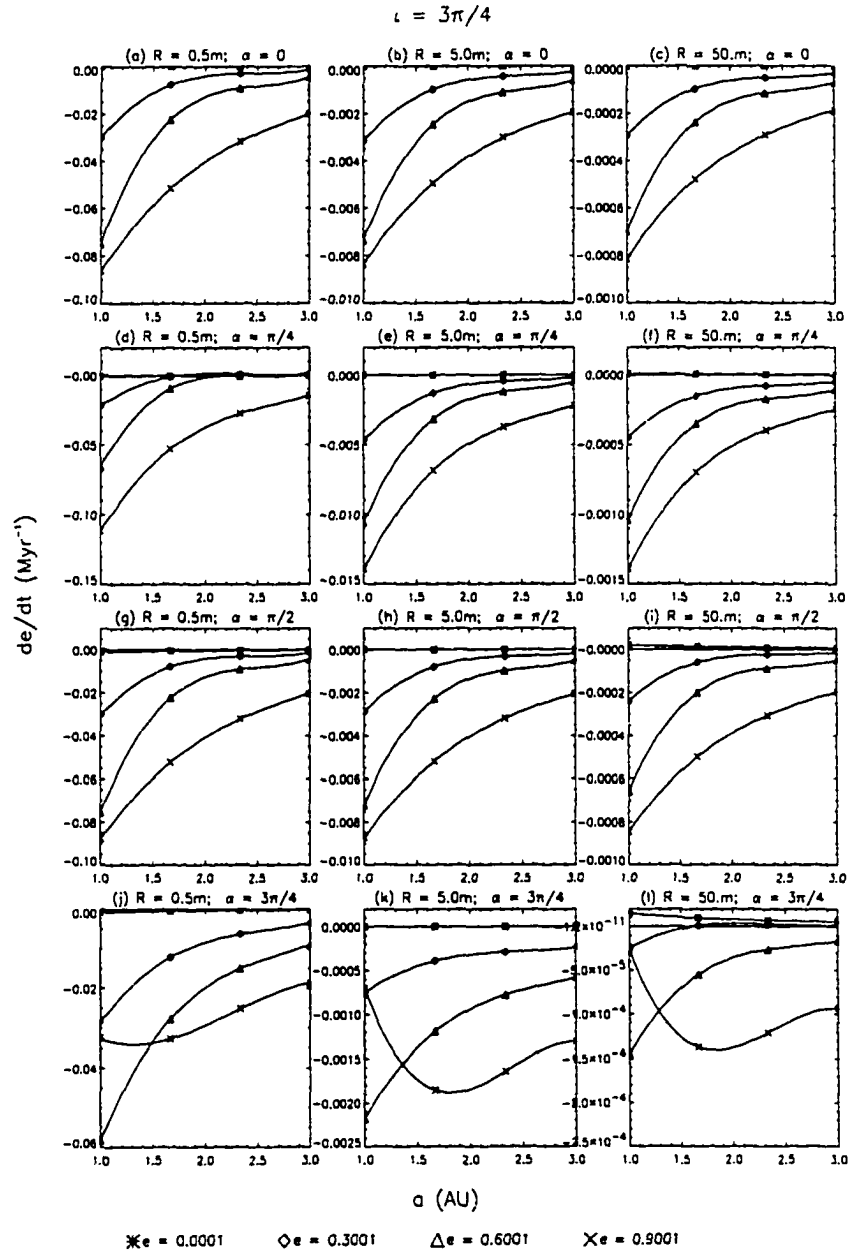
6.3 Cases with $\iota = 3\pi/4$

Rates of change of e, i, and ϖ are shown in figures 6.19 and 6.20 for cases with $\iota = 3\pi/4$, that is, retrograde rotation with the spin axis 45° below the orbital plane. These cases span a range of spin axis orientation, α, relative to the pericenter longitude ($\alpha = 0, \pi/4, \pi/2, 3\pi/2$).

The results for the in-plane elements de/dt and $d\varpi/dt$ (Figs. 6.19 and 6.20) are well approximated by linearly combining results for $\iota = \pi$ from Sec. 6.1 and $\iota = \pi/2$ from Sec. 7.3 using coefficients of $\cos\iota$ and $\sin^2\iota$ respectively (recall from Chapter 5 that these coefficients were derived by Öpik (1951) and Rubincam (1987), respectively). This procedure works for the in-plane elements because good approximations to the pure diurnal and seasonal extremes can be isolated for the right parameter choices (i.e. $\iota = 0$ or π yields a pure diurnal effect and $\iota = \pi/2$ approximates a pure seasonal effect for small e, being best for larger a) as long as one disregards the out-of-plane acceleration components associated with the Yarkovsky effect at $\iota = \pi/2$, which have no effect on the in-plane elements. Because the case $\iota = \pi/2$ does not approximate the pure seasonal case as well for large e and because the nonlinearity of the boundary condition is more important at large e, this procedure is most valid for orbits with small e.

For high-eccentricity orbits, the above procedure is useful, though less accurate. Cases corresponding to reversing the spin vector (i.e., $\alpha = \pi, 5\pi/4, 3\pi/2, 7\pi/4$), were not examined, but those results should be reasonably approximated using the above linear combination procedure and substituting the diurnal component corresponding to $\iota = 0$.

6.4 Discussion

In this chapter, I have presented results for changes in eccentricity and longitude of periapse caused by the general Yarkovsky effect over a wide range of parameters.
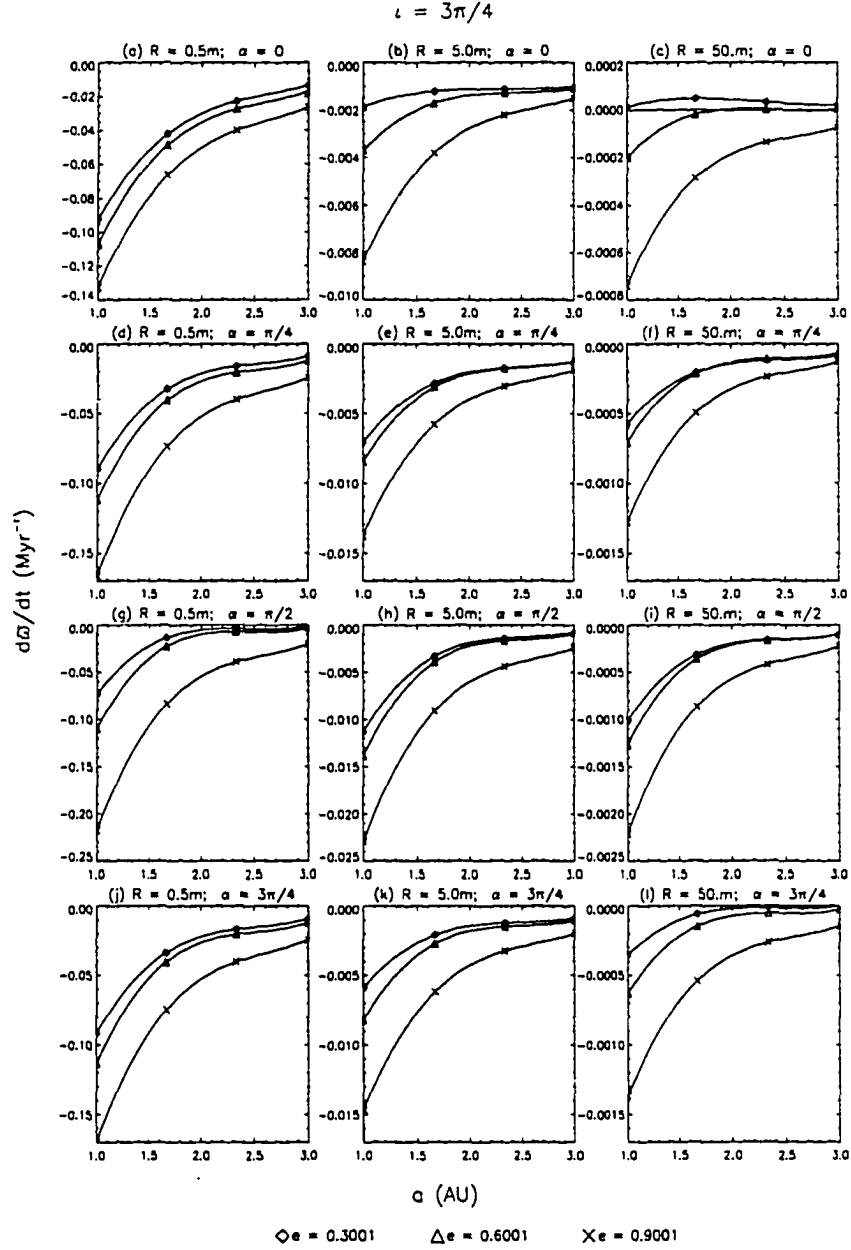
Figure 6.20: $d\varpi/dt$ vs. a for for the cases shown in Fig. 6.19. These results are roughly consistent with a suitable linear combination of the $\iota = 0$ or π and $\iota = \pi/2$ results from Figs. 6.16 and 6.18. For the cases $\alpha = \pi, 5\pi/4, 3\pi/2, 7\pi/4$, reasonable approximations may be obtained using the above linear combination procedure and substituting the diurnal component corresponding to $\iota = 0$.

These results complement the rates of change in semimajor axis reported in Chapter 5. For certain configurations, orbitally-averaged rates of change can be remarkably fast. For example, with $\iota = 0$ or π, de/dt can be as fast as 0.1 per million years for a 1-m body. Recall that, for large e, cases were found in Chapter 5 where da/dt can be 1 AU per million years.

Inclination changes were not studied here because orbital precession due to gravitational perturbations from the planets would likely prevent the accumulation of significant long-term inclination changes. Indeed, direct numerical integrations of a large number of asteroid orbits (e.g. Bottke et $al.$ 2000) have shown that precession tends to prevent significant long-term inclination changes for all the examples they have considered with the Yarkovsky model they used.

For eccentricities, the cases in this chapter where changes were found to be rapid are not affected by either apsidal or rotational precession because in all of these cases the spin axis is normal to the orbital plane. Nodal precession could diminish such changes, but as long as inclinations are small, I see no reason why those eccentricity changes could not accumulate over long timescales, given an appropriate rotation state.

Many of the results obtained here can be readily scaled to larger bodies. For example, the graphs in Fig. 6.15(a, b and c) are virtually identical, except for a $1/R$ dependence, which is due to the fact that the temperature variations are limited to a near-surface zone that is thin compared to the radius of even the smallest of the three bodies. Such results can, in principle, be scaled to larger sizes, as long as the thermal model remains applicable (e.g. these results would not be valid for a body with an atmosphere) and as long as the body has uniform density (e.q. it is not substantially internally compressed). Thus, for example, a 1-km body (which, according to Eq. (10.138), should rotate with a 5-h period as assumed in this work) could change its eccentricity by 0.05 during its collisional lifetime of about 4.5×10^8 yr.

CHAPTER 7

EFFECTS OF AN INSULATING REGOLITH

Some asteroids may possess a relatively thin, highly-insulating surface layer. For example, some authors (Langevin and Maurette, 1980; Housen et al., 1979) suggest that, depending on its size, the outer 1% of an asteroid's radius could be a porous regolith. Surface temperatures, and hence Yarkovsky mobilities, for bodies with a highly-insulating regolith are likely to be vastly different than for homogeneous bodies. Therefore, the results presented in Chapters 5 and 6 may not tell the entire story.

The effect of regolith on Yarkovsky mobility has been discussed previously in the literature, but much work remains to be done. Rubincam (1995) simulated an insulating regolith using his linearized treatment of the pure seasonal Yarkovsky effect by simply substituting a much smaller value for his uniform thermal conductivity, effectively assuming that the regolith was thick enough that only the regolith is affected by the seasonal wave. That calculation suggested that the pure seasonal effect should be significantly inhibited for bodies with such a thick regolith. Vokrouhlický and Brož (1999) performed a more general, though linearized, calculation of the seasonal effect for regolith-covered bodies by including an additional boundary condition to account for the interface at the bottom of the regolith, allowing them to investigate thinner regoliths. They also found that the seasonal effect is inhibited by the addition of a highly insulating surface layer, though for bodies of radius 10 m and larger the effect was not nearly as severe. Because both of those studies were based on a linearized treatment of the heat equation, they were applicable only to bodies on orbits with small eccentricity.

In this chapter, the finite-difference approach, which is valid for any eccentricity and arbitrary internal structure, is used to investigate 10- and 100-m bodies possessing insulating layers (density $\rho = 1500$ kg m^{-3}, thermal conductivity $k = 0.0024$ W m^{-1} K^{-1}) with thicknesses of 0.01 and 0.001 body diameters. These sizes and regolith thicknesses were chosen to include reasonable expected regolith thicknesses (Langevin and Maurette, 1980; Housen et al., 1979), as well as for practical reasons (for regoliths thinner than about 1 cm, the timestep must be reduced, making the approach far less practical, hence the exclusion of 1-m bodies), and because those thicknesses (1 cm to 1 m) encompass three interesting thermal scenarios: (1) pure diurnal Yarkovsky effect with "thick" regolith, that is, where diurnal thermal wave does not substantially penetrate the regolith, (2) ~pure seasonal Yarkovsky effect with thick regolith, where the seasonal thermal wave does not substantially penetrate the regolith, and (3) ~pure seasonal Yarkovsky effect with "thin" regolith, that is, where the diurnal thermal wave does penetrate the regolith. As mentioned above, the pure diurnal case with thin regolith is excluded because it would require an extremely short timestep.

7.1 Results

In this section, I present results for rates of change of semimajor axis, eccentricity and longitude of periapse caused by the Yarkovsky effect on bodies with varying thicknesses of a highly insulating surface layer. These calculations span a range of values for radius R, semimajor axis a, eccentricity e, obliquity ι, and regolith thickness L, which is expressed in terms of the regolith fraction $f_r = L/R$. In all cases, $i = 0$ and $p = 5$ h.

For brevity, the bodies in this study were constructed by adding insulating layers to a only subset of the 10- and 100-m cases studied in Chapters 5 and 6. For example, only obliquities of π and $\pi/2$ were examined because it was seen in previous chapters that the results for cases with intermediate obliquities may

be reasonably approximated using a suitable linear combination of the $\iota = \pi$ and $\iota = \pi/2$ results. However, despite its reduced breadth compared to the previous chapters, this survey samples parameters that have not been accessible to previous approaches.

7.2 Cases with $\iota = \pi$

The cases examined in this section, cases with retrograde rotation and spin axis perpendicular to the orbit plane, correspond to a nearly pure diurnal Yarkovsky effect. Only "thick" regolith is considered here because even the thinnest regolith layer that was practical to use in this study was too thick to be substantially penetrated by the relatively shallow diurnal thermal wave.

Because of its low thermal conductivity, heat deposited into the regolith on diurnal timescales should be retained near the surface, rather than being conducted into the interior, as in the bare-rock case. Moreover, surface temperatures should respond more quickly to the heating cycle. Therefore, surface temperature excursions should be larger and the thermal lag smaller than for the homogeneous cases of Chapters 5 and 6. Hence, the net diurnal Yarkovsky acceleration should be larger in magnitude (favoring a larger instantaneous change in semimajor axis) but directed more radially outward (favoring a smaller instantaneous change in semimajor axis), than in the homogeneous case. As will be seen in this section, the net effect of an insulating regolith on Yarkovsky orbital changes caused by purely diurnal heating depends on the specific orbital elements and spin properties of an asteroid.

Figures 7.21, 7.22, and 7.23 summarize results for these nearly pure-diurnal cases. Note, as in Chapter 6, that the spin axis is not exactly perpendicular to the orbital plane, although the difference is negligible. Also, for $e = 0.0001$, $d\varpi/dt$ can be large with little actual change in the orbit and is thus not useful. Hence, results for cases with $e = 0.0001$ are not included in any of the plots for $d\varpi/dt$ (e.g. Figs. 7.23 and 7.26).

Figure 7.21: Rate of change of semimajor axis da/dt, vs. a. Six graphs are shown, for three regolith thicknesses (from left to right, f_r =0, 0.001, and 0.01) and two radii ($R = 5$ m top row, 10 m bottom row). On each graph, four curves represent cases with $e = 0.0001$, 0.3001, 0.6001, and 0.9001. In all cases, $\iota = \pi$, $i = 0$ and rotation period $= 5$ h. Symbols indicate computed results; solid curves are interpolated.

As mentioned above, with respect to the diurnal thermal wave, all of the cases in this section are in the regime of "thick" regolith. The diurnal thermal wave penetrates a characteristic distance of about 0.6 cm in the low-conductivity regolith, while the thinnest regolith in the study has a thickness of 1 cm. Hence, in frames (b), (c), (e), and (f) of Fig. 7.21 (1 cm, 10 cm , 10 cm , and 100 cm of regolith respectively), the interface at the bottom of the regolith layer is not sensed by the thermal wave so increasing the regolith thickness further does not change the result. Consequently, frames (b) and (c) of Fig. 7.21 are virtually identical to one another. Similarly, frames (e) and (f) are virtually identical to one another, and they differ from frames (b) and (c) by factor of almost exactly 10, which is due to their size
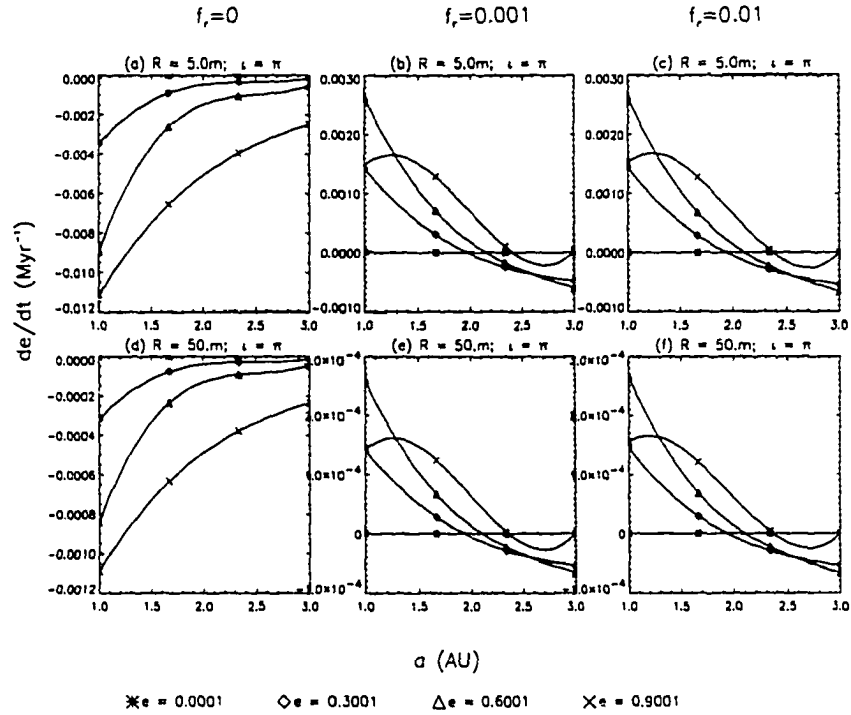
Figure 7.22: Rate of change of eccentricity de/dt, vs. a for the same cases shown in Fig. 7.21.

difference. Analogous behavior is seen for de/dt (Fig. 7.22) and $d\varpi/dt$ (Fig. 7.23). None of these observations are surprising, however, and no insight was gained by performing calculations for both the pure-diurnal $f_r = 0.001$ and $f_r = 0.01$ cases. However, the fact that the results corroborate our expectations gives us additional confidence in the validity of the less-intuitive results presented later in this chapter.

The following observations are worthy of comment:

1) Except for the $e = 0.9001$ curves in Fig. 7.21, da/dt caused by the pure diurnal Yarkovsky effect can be nearly tripled by the addition of regolith, suggesting that, at least for this rotation rate and these thermal properties, the more pronounced temperature asymmetry wins out over the decreased lag angle.

2) For cases with regolith, de/dt changes sign relative to the bare-rock case. It is actually positive for the purely-diurnal cases with smaller a and larger e, despite
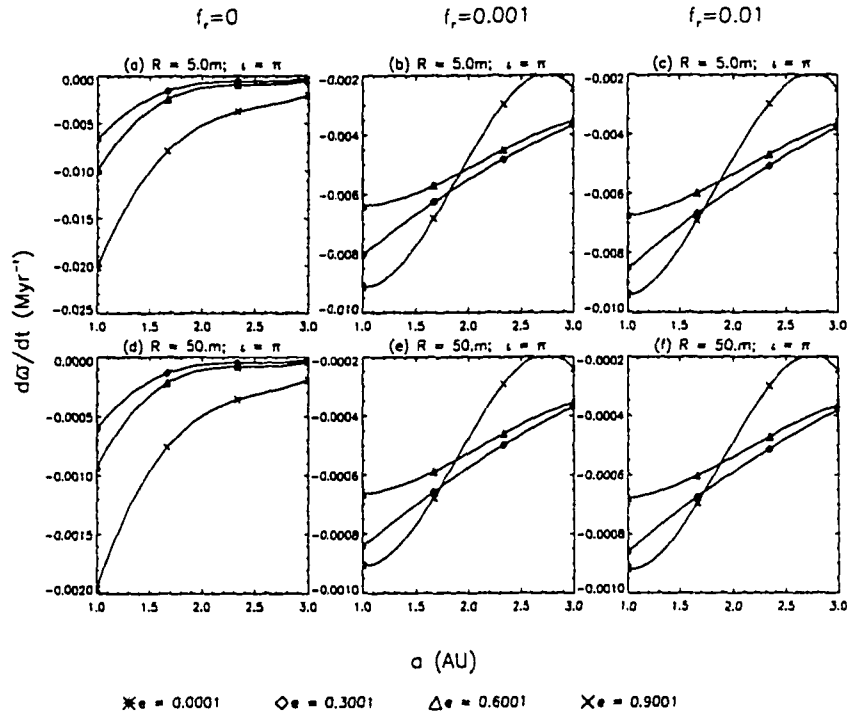
Figure 7.23: Rate of change of pericenter longitude $d\varpi/dt$, vs. a for the same cases shown in Fig. 7.21.

their retrograde rotation, which usually implies negative de/dt. This result can be understood in physical terms: In these cases, relative to the bare-rock case, the lag angle tends to be considerably larger (more negative in these retrograde-rotation cases) near apoapse (where kicks in the retrograde direction tend to cause an instantaneous increase in eccentricity) than near periapse (where kicks in the retrograde direction tend to cause an instantaneous decrease in eccentricity). This effect, and the fact that the body spends more time near apoapse than near periapse appear to dominate the evolution, despite the considerably larger acceleration vectors near periapse compared to those near apoapse. For larger a, the contrast between accelerations near periapse and those near apoapse becomes more extreme and this effect wins out, producing a net decrease in eccentricity.

3) For most cases with $a > 1$ AU, the periapse longitude can regress up to a few times more quickly for the purely-diurnal cases with regolith than for those

without and the effect becomes greater with increasing a. It is not surprising that the magnitude of $d\varpi/dt$ should increase with increasing a because the contrast between the magnitudes of the radial components near periapse (which cause the periapse to regress) and those near apoapse (which cause the periapse to advance) becomes more extreme (i.e., radial accelerations near periapse grow more quickly with increasing a than do those near apoapse).

4) Despite the fact that the contrast between the magnitudes of the radial components near periapse and those near apoapse increases with eccentricity, $d\varpi/dt$ is not a strong function of e for any of the purely-diurnal cases shown, probably because the contrast between the durations spent near apoapse compared to periapse also becomes more extreme with increasing e. Those two effects would tend to cancel one another.

7.3   Cases with $\iota = \pi/2$

In addition to a diurnal effect, the cases examined in this section, cases with the spin axis in the orbital plane, experience a substantial seasonal Yarkovsky effect. For cases with low eccentricity, particularly those on the larger end of the semimajor axis range used here, diurnal effects are relatively unimportant in changing in the in-plane elements $(da/dt, de/dt,$ and $d\varpi/dt)$, so the results obtained are approximately the same as would be obtained for the pure-seasonal Yarkovsky effect. As ϵ is increased, diurnal effects near periapse become important so the results for those cases diverge from those that would be obtained in the pure-seasonal extreme, particularly for cases with smaller a.

For the cases in this section, two possibilities are considered, distinguished by the characteristic thermal penetration depth, $l = \sqrt{\kappa P}$, where κ is the thermal diffusivity: (1) the "thick" regolith case where the regolith is thick enough that the seasonal thermal wave does not substantially penetrate it $(l > L)$ and (2) the "thin" regolith case, where the regolith is thin enough that the seasonal thermal wave does

penetrate it $(l > L)$. In the thick-regolith case, the surface temperature excursions should be larger, and the lag angle smaller than for the bare-rock case. For thin regolith, the surface temperature distribution should have components corresponding to (1) a low-thermal-inertia seasonal solution caused by recent heating and (2) a high-thermal-inertia seasonal solution representing heat that was deposited much earlier in the seasonal cycle and that was conducted into the interior. For this thin-regolith case, the average thermal lag should be larger than for the thick regolith case, but possibly smaller than for the bare-rock case. Surface temperature excursions should be less extreme than for the thick-regolith case, but more extreme than in the bare-rock case. The net effect will depend on the specific properties of the body and its orbital configuration.

Figures 7.24, 7.25, and 7.26 summarize the results for cases with $\iota = \pi/2$, where the spin axis lies in the orbit plane.

The seasonal thermal wave permeates the low-conductivity regolith material to about 26 cm at $a = 1$ AU and about 59 cm at $a = 3$ AU. Hence the cases in frames (b), (c), (e), and (f) of Figs. 7.24, 7.25, and 7.26 span a range in a where the seasonal thermal wave penetrates the regolith by a substantial margin (frames (b), where $L = 1$ cm) to cases where the seasonal thermal pulse is not able to significantly penetrate the regolith (frames (f), where $L = 100$ cm).

The following observations are noteworthy:

1) In frames (c), (e), and (f) of Figs. 7.24, 7.25 and 7.26, depending on the size and semimajor axis, the thermal wave, at most, only slightly affects the subregolith during the orbital period, so it is not surprising that those results are similar to one another, except for factors associated with the size difference. On the other hand, the results in frames (b) of those figures differ completely from the others because in those cases, most of the seasonal thermal wave reaches the subregolith.

2) For most of the cases with $\iota = \pi/2$, the addition of the insulating regolith inhibits Yarkovsky semimajor axis mobility. This observation might be accounted
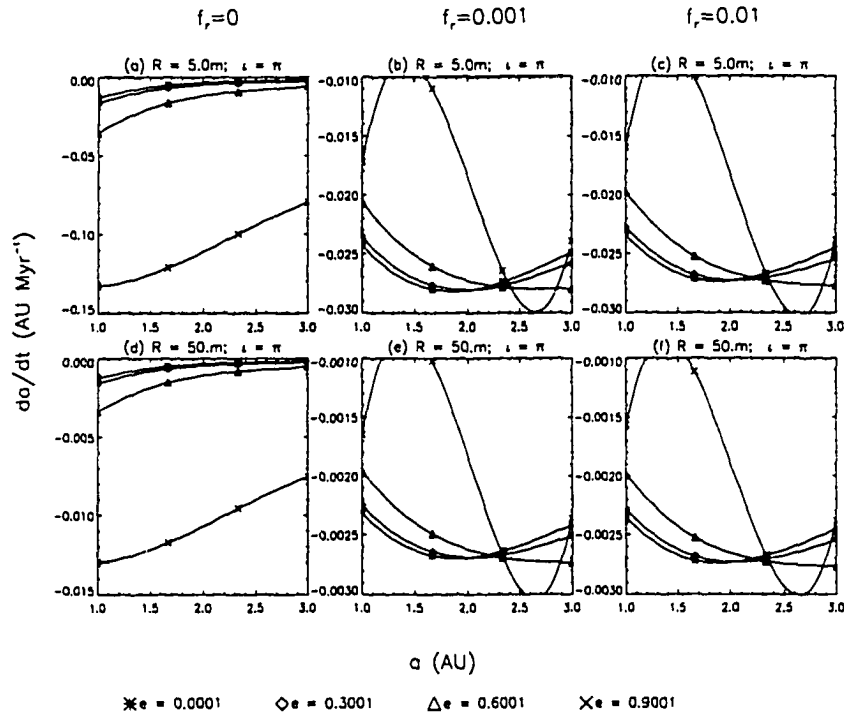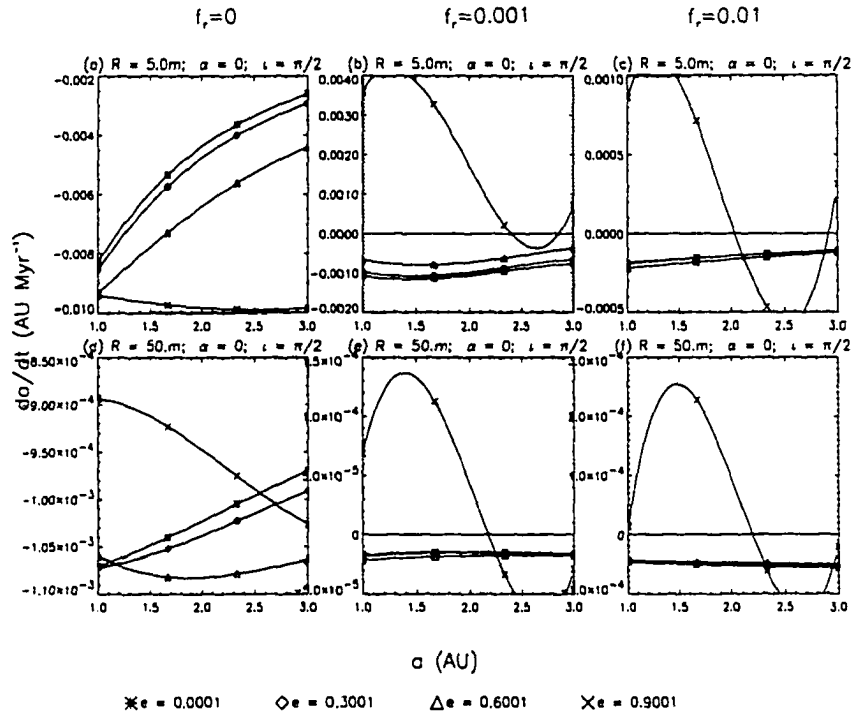
Figure 7.24: Rate of change of semimajor axis da/dt, vs. a. Six graphs are shown, for three regolith thicknesses (from left to right, f_r =0, 0.001, and 0.01) and two radii ($R = 5$ m top row, 10 m bottom row). On each graph, four curves represent cases with $e = 0.0001$, 0.3001, 0.6001, and 0.9001. In all cases, $\iota = \pi/2$, $i = 0$ and rotation period = 5 h. Symbols indicate computed results; solid curves are interpolated.

for partially by the smaller seasonal lag associated with the low thermal inertia relative to the bare-rock case. However, because of the finite rotation rate used in this calculation, there is a substantial diurnal component resulting in acceleration vectors that are larger than in the pure-seasonal case, but nearly radial everywhere in the orbit instead of being directed along the spin axis as is the case for the pure-seasonal effect. Thus, the along-track acceleration components are considerably smaller for the regolith-covered body than for the bare-rock body. This effect also favors a smaller da/dt than in the bare-rock case.

3) The two effects discussed in the previous paragraph also favor smaller de/dt than for the bare-rock case, as observed in Fig. 7.25, frames (c), (e), and (f). It is not
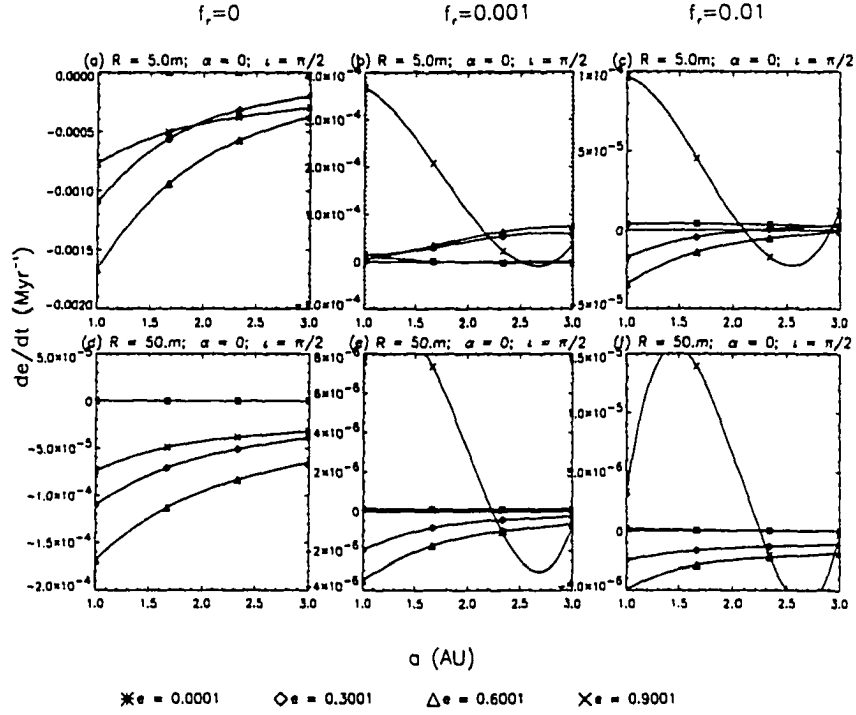
Figure 7.25: Rate of change of eccentricity de/dt, vs. a for the same cases shown in Fig. 7.24.

clear, however, why de/dt should be positive for most of the cases in frame (b).

7.4 Discussion

Asteroid orbital evolution caused by the Yarkovsky effect can be significantly modified by the addition of an insulating regolith. The actual behavior (as a function of a and f_r) is difficult to summarize in terms of simple generalities, but for cases with low- to moderate eccentricity, semimajor-axis mobility caused by the pure diurnal effect (cases with $\iota = \pi$) can be enhanced by perhaps a factor of three (depending on a and e) by the addition of a "thick" regolith (thick enough the the diurnal thermal wave does not penetrate to the interior), while da/dt caused by the pure seasonal effect (approximated in this paper by cases with $\iota = \pi/2$ and low- to moderate e) may be substantially inhibited by the addition of regolith. For cases with higher
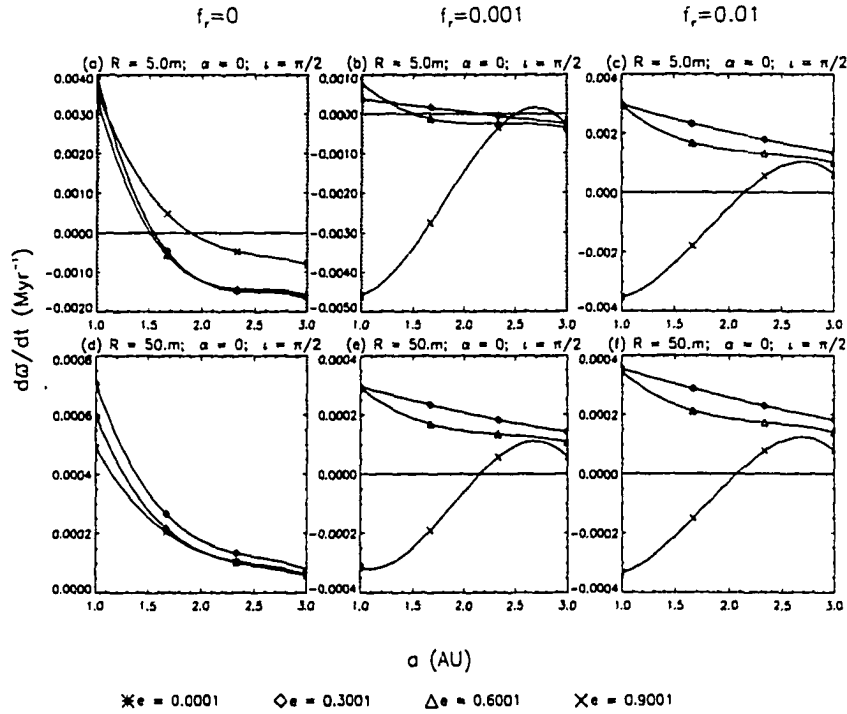
Figure 7.26: Rate of change of pericenter longitude $d\varpi/dt$, vs. a for the same cases shown in Fig. 7.24.

e, the behavior is more complicated and almost certainly undersampled in semi-major axis. Insofar as these studies can be compared, the above result regarding the seasonal effect is generally consistent with the qualitative trends calculated by Rubincam (1995) and Vokrouhlický and Brož (1999).

As in the previous chapters, some of the results presented here may be scaled to larger sizes. As long as the regolith is considerably thicker than the characteristic thermal penetration depth corresponding to the forcing period of interest, the results scale as $1/R$. In other words, frames (f) and (l) of Figs. 7.21, 7.22, and 7.24 and frame (f) of fig 7.23 may be readily scaled to larger sizes. This restriction to "thick" regolith is limiting, but such an extrapolation still allows one immediately to have an idea of how the Yarkovsky effect modifies the orbital elements of large bodies on highly-eccentric orbits. Such cases have not been accessible to previous approaches.

Although thermal properties were assumed to be independent of temperature in this chapter, radiative transfer is probably important in a loosely consolidated regolith so in reality, the bulk thermal conductivity in the regolith is likely to be strongly temperature-dependent. In the course of this study, I experimented with temperature-dependent thermal properties for the regolith of the form

$$k(T) = A + BT^3. \tag{7.123}$$

For reasonable (stony) material coefficients A and B (e.g. Linsky (1973)), the results were not changed by more than about 10% for the cases that tested. Hence, the temperature dependence was neglected in the full survey in order to save time. Nevertheless, this effect should be investigated in more depth in the future. In particular, temperature-dependent thermal properties may be important for highly porous bodies where much of the internal heat transport is radiative rather than conductive.

CHAPTER 8

APPLICATION TO SPECIFIC NEAR-EARTH ASTEROIDS

8.1 Motivation

While theoretically well-established, the Yarkovsky effect has yet to be seriously considered by the entire asteroid community. This lack of universal recognition is largely due to the complexity of the Yarkovsky effect. Unlike purely gravitational perturbations, which have effects that are essentially independent of the specific characteristics of a small body, the precise magnitude and sense of the Yarkovsky effect depend sensitively on many poorly-known details of a given asteroid. Among these poorly-known parameters are the surface thermal conductivity, internal arrangement, density, shape, porosity, and reflectance properties. Therefore, it is often suggested that one may obtain any answer one desires by manipulating the free parameters accordingly. In fact, Yarkovsky calculations (by myself and others in the field) are generally performed using the most plausible physical characteristics that are practical for a given calculation. The results of such calculations demonstrate that the Yarkovsky effect is important, even if the precise rates are still uncertain. Nevertheless, a direct observation of the Yarkovsky effect operating on a real solar system body would add to its credibility as an important dynamical process.

In fact, the Yarkovsky effect has been directly observed. Rubincam (1987) discovered the seasonal variant of the Yarkovsky effect as an explanation for the anomalous semimajor axis decay of the LAGEOS satellite. The physical characteristics of that satellite were well-known and a convincing case could be made that

the seasonal Yarkovsky effect was responsible for its orbital decay. However, the same is not currently true for natural bodies.

Besides enhancing the credibility of the Yarkovsky effect, precise measurements of the drift experienced by real solar system bodies may provide information about those poorly-known parameters, particularly the surface thermal conductivity. The most precise tool available for measuring the position and velocity of a body in space, and thus Yarkovsky perturbations, is radar.

Pioneering work on the prediction of Yarkovsky perturbations on specific near Earth asteroid orbits has been done by Vokrouhlický et al. (2000). I have examined some cases with my numerical approach to test their results. The results of the two approaches agree to within an order of magnitude. The objective of this chapter is to examine the dependence of those results on shape, and to place them in the context of upcoming radar observations of these asteroids.

8.2 Radar astrometry

Since the first radar observation of an asteroid, 1566 Icarus (Goldstein, 1969), radar has been a powerful tool for studying the physical characteristics of asteroids. Radar observations constrain an asteroid's shape, size, spin vector, and surface properties, including roughness, porosity, and metal abundance. Given sufficient signal-to-noise, an "image" of the body may even be extracted. However, of primary interest in this chapter are the precise orbital corrections that may be obtained using radar measurements of time delay and doppler. Such corrections provide much more precise orbital constraints than optical observations alone, and can substantially increase the probability of recovering an object on a future apparition.

8.3 Observable Yarkovsky perturbations

Assuming the Yarkovsky-induced rates of orbital change are constant over the relatively short time intervals (decades) that we are interested in, I examine the displacements caused by changing each orbital element independently of the others. Here, the term *displacement* refers to the difference between the predicted position of the body neglecting the Yarkovsky effect and that with the Yarkovsky effect included. This usage is consistent with that of Vokrouhlický et al. (2000).

8.3.1 Eccentricity perturbation

A drift in eccentricity caused by the Yarkovsky effect would be observed as a displacement in the perihelion or aphelion distance and in the true anomaly. Because the mean motion is unchanged, the discrepancy in the true anomaly would oscillate, but would not grow with time. Changes in perihelion and aphelion distances, q_+ and q_- respectively, would grow with time:

$$
\begin{aligned}
q_\pm &= a(1 \pm e) \\
\delta q_\pm &= a(1 \pm \Delta e) \\
&= a(1 \pm \dot{e}\Delta t),
\end{aligned}
\tag{8.124}
$$

but only linearly, so the Yarkovsky de/dt would have to be extremely fast in order to produce an observable perihelion or aphelion displacement during a useful timescale.

8.3.2 Inclination perturbation

The largest displacement caused by an inclination change would be the elevation at aphelion, Δz, of the body relative to the invariable plane:

$$
\begin{aligned}
\Delta z &= q_+ \Delta i \\
&= q_+ \dot{i} \Delta t,
\end{aligned}
\tag{8.125}
$$

which also accumulates only linearly with time.

8.3.3 Yarkovsky-Induced Precession

Perihelion and nodal precession, $d\varpi/dt$ and $d\Omega/dt$, might be most observable as a displacement in the position of some feature of the orbit, such as aphelion. However, as any such feature will simply precess at the uniform rate $d\varpi/dt$ or $d\Omega/dt$, it will change only linearly with time.

8.3.4 Semimajor axis perturbation

A semimajor axis perturbation would produce a displacement in the periapse or apoapse distances, q_+ and q_- respectively, of a body. Such displacements would grow with time:

$$
\begin{aligned}
q_\pm &= a(1 \pm e) \\
\delta q_\pm &= \Delta a(1 \pm e) \\
&= \dot{a}\Delta t(1 \pm e),
\end{aligned}
\tag{8.126}
$$

but only linearly, similar to the case for de/dt.

However, the semimajor axis perturbation will also cause the mean motion to change and this would be observed as a discrepancy in the mean anomaly, $\mathcal{M}$. The mean anomaly is defined as

$$
\mathcal{M} = n(t - \tau),
\tag{8.127}
$$

where n is the mean motion, t is time, and τ is the time of last perihelion passage. Remembering that n varies with time, the mean anomaly at some later time $t + \delta t$ is $\mathcal{M} + \delta\mathcal{M}$, with

$$
\delta\mathcal{M} = n\delta t + (t - \tau)\Delta n,
\tag{8.128}
$$

where Δn is the change in mean motion during the time interval δt. Since $n^2 a^3 = \mu$, we have

$$
\begin{aligned}
n^2 &= \mu a^{-3} \\
2n\Delta n &= -3\mu a^{-4}\Delta a \\
\Delta n &= -\frac{3}{2}\frac{\mu a^{-4}}{n}\Delta a \\
&= -\frac{3}{2}\frac{n}{a}\Delta a.
\end{aligned}
\tag{8.129}
$$

Therefore,

$$
\begin{aligned}
\Delta \mathcal{M} &= (t - \tau)\left(-\frac{3}{2}\frac{n}{a}\Delta a\right) \\
&= -\frac{3}{2}\frac{n}{a}\frac{da}{dt}\Delta t(t - \tau).
\end{aligned}
\tag{8.130}
$$

If t_0 is the time at which a discrepancy in mean anomaly begins to accumulate, then we can approximate

$$
\begin{aligned}
t - \tau &= (t - t_0) - (t_0 - \tau) \\
&= \Delta t - (t_0 - \tau).
\end{aligned}
\tag{8.131}
$$

$\Delta \mathcal{M}$ will contain terms linear and quadratic in time, but will be dominated by the quadratic term, so we write

$$
\Delta \mathcal{M} \simeq -\frac{3}{2}\frac{n}{a}\frac{da}{dt}(\Delta t)^2.
\tag{8.132}
$$

The observable quantity associated with $\Delta \mathcal{M}$ will be a transverse displacement, Δr, which will increase quadratically with time:

$$
\Delta r \simeq -\frac{3}{2}\mu^{1/2}a^{-3/2}\frac{da}{dt}(\Delta t)^2.
\tag{8.133}
$$

Because of this time-dependence, the transverse displacement associated with the semimajor axis drift dominates the other observables, which grow only linearly with time. Therefore, I will concentrate on the semimajor axis drift rate for the rest of this chapter.

8.4 Potential targets

What bodies are most likely to exhibit fast Yarkovsky drift rates? As mentioned previously (Chapter 2), a stony body of a given size would be expected to experience a much stronger Yarkovsky effect than a metallic body of the same size, both because of its lower density and because of its lower thermal conductivity.

Also, smaller bodies tend to drift faster than larger ones because of their typically lower mass. However, very small bodies isothermalize quickly and the Yarkovsky effect becomes less effective as the size is decreased. For stones, the drift rates peak at diameters of around 0.1- to 1 m.

Finally, it was demonstrated in Chapter 5 that slow rotators may experience a fast Yarkovsky drift if their spin axis is nearly perpendicular to their orbital plane. It is more precise to say that, for bodies with such a spin axis orientation, the Yarkovsky effect tends to be maximized when the rotation period is similar to the time it takes the diurnal thermal wave to penetrate to the center (see Chapter 3). This rotation period tends to be much longer than "typical" (i.e. predicted by Farinella et al. (1998)) rotation periods for bodies of that size. Indeed, for stony material, the size at which that typical rotation period and the penetration time are equal (using the Farinella et al. (1998) formula) is around one micron. Of course, Farinella's estimate is not applicable to bodies of that size, but one can conclude that, for any size at which the Farinella scaling does apply, the optimum diurnal Yarkovsky effect occurs at a rotation period that is much longer than Farinella's typical rotation period.

To summarize the above paragraphs, the bodies that would be expected to exhibit the strongest Yarkovsky effects are meter-scale, stony, slow rotators with low obliquities.

What observational biases affect the assessment of potential targets? Size, of course, is one consideration. Meter-scale bodies like those mentioned above are

too small to be observed using current radar technology, but currently objects with diameters somewhat smaller than 50 m are routinely observed with radar. Also, bodies that make close approaches to Earth are obviously more likely to be detected than bodies that do not. Finally, bodies that have been observed on one or more previous apparitions have two advantages: (1) their orbits are already fairly well-determined, and (2) the Yarkovsky displacement may already be evident in the existing data on such objects, or it may be detectable in the near future.

One final observational issue concerns the reacquisition of a target. It might be possible for the Yarkovsky perturbation on the orbit of an object to be so strong that it is impossible to predict its ephemeris precisely enough to identify it the next time it appears. It may be subsequently detected, but its orbit will have evolved sufficiently under the Yarkovsky effect that it would be mistakenly classified as a new object. Therefore, bodies that exhibit extremely strong Yarkovsky effects may in fact be poor candidates for the direct measurement of Yarkovsky displacements.

Using the finite-difference approach, I have computed orbital changes for model asteroids whose characteristics are intended to simulate those of three NEAs that were also studied by Vokrouhlický et al. (2000). 1620 Geographos is a stony Earth crosser with a moderate obliquity and a roughly typical rotation period. Assuming a bulk density of 2 g cm^{-3}, a sphere whose volume is equivalent to that estimated for Geographos has a diameter of about 2500 m. This asteroid has been observed with radar during two apparitions since 1983. 1566 Icarus is a stony Earth crosser with high obliquity and a fairly typical rotation period for its size. Its equivalent sphere has a diameter of about 1000 m. It has been observed with radar during two apparitions since 1968. The third asteroid, 6489 Golevka, is a stony, relatively slowly rotating NEA with a periapse distance somewhat larger than 1 AU, and a fairly small obliquity. Its equivalent sphere has a diameter of about 300 m. It has been observed using radar during two apparitions since 1991.

All of the above bodies have characteristics that make them good candidates for Yarkovsky effect observations. Because of Golevka's small size, small

obliquity, and slower-than-typical rotation rate, it would be expected exhibit a larger Yarkovsky da/dt than Icarus and Geographos. On the other hand, it has been observed for less than ten years, so it has not had as much time as the others to accumulate an observable Yarkovsky displacement. Icarus is intermediate in size, but has the advantage of a 30-yr observational baseline during which to accumulate a Yarkovsky displacement. However, because of its high obliquity, its Yarkovsky displacements could still be fairly small. Geographos is large, but its moderate obliquity and longer observational history still make it a good candidate for Yarkovsky effect observations. All three of these bodies have been observed during two apparitions, so the problem of reacquisition is not a concern.

8.5 Results

Figures 8.27, 8.28, and 8.29 present results for model asteroids whose characteristics resemble those of the near Earth asteroids 6489 Golevka, 1566 Icarus, and 1620 Geographos. For each body, I show two curves of da/dt as a function of surface thermal conductivity k_s. For one curve, the model parameters are identical to those used by Vokrouhlický et al. (2000). For the other curve, the model parameters are identical to those of the first, except that each body is modeled as an ellipsoid whose volume is the same as that of the corresponding spherical model. As in Vokrouhlický et al. (2000), to account for porosity, the surface density ρ_s is varied with surface thermal conductivity as follows:

$$\rho_s = \left[1500 + \frac{500}{3}(\log(k_s \ W^{-1} \ m \ K^4) + 3)\right] \ kg \ m^{-3}, \qquad (8.134)$$

while the density of the interior of each model is varied so as to maintain a bulk density of 2 g cm^{-3} for each run.

There should be some difference in Yarkovsky da/dt between the spherical and the ellipsoidal models simply due to the fact that, while the volumes are kept equal, the surface areas are not. That effect should be no larger than a few percent
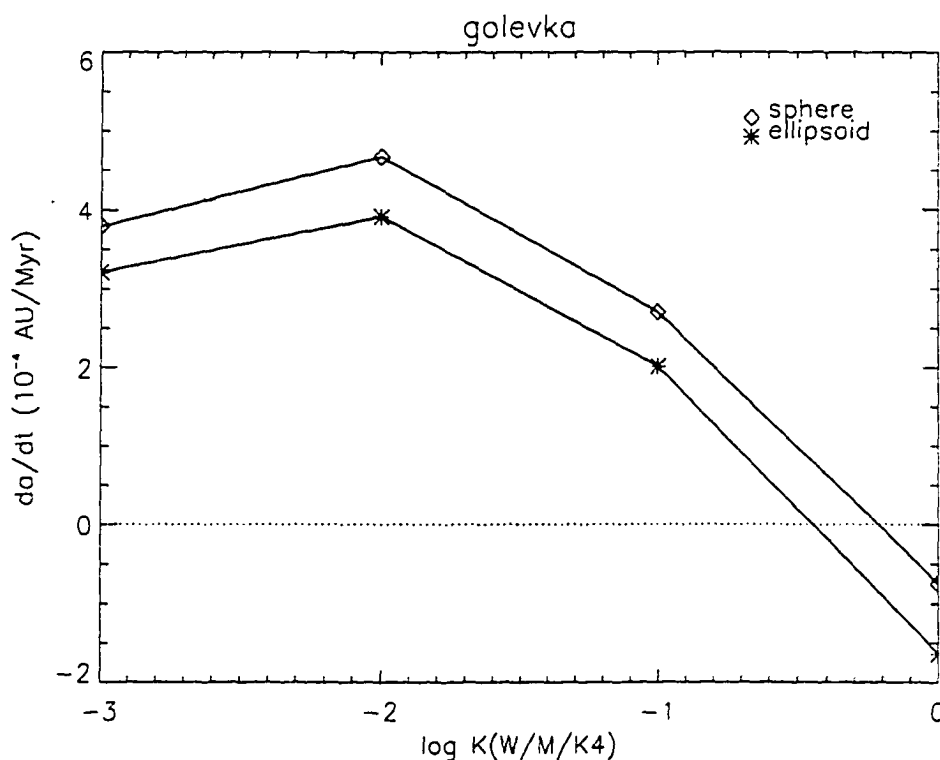
Figure 8.27: Rate of change of semimajor axis da/dt, caused by the Yarkovsky effect as a function of surface thermal conductivity k for two models of 6489 Golevka. Diamonds indicate results for a spherical body of radius 140 m. Asterices indicate results for an ellipsoid model with axes 157-, 111-, and 111 m.

and for a given model all of the points will be affected in the same sense. Therefore, differences of a few percent or less between the spherical and ellipsoidal cases for a given model should be not considered significant.

Yarkovsky da/dt rates for Golevka and Geographos do not appear to be very sensitive to shape, at least at this level of approximation. On the other hand, Icarus' semimajor axis evolution is apparently strongly shape dependent. That shape dependence may be due to the large eccentricity of Icarus' orbit, but Icarus also has a high obliquity, unlike Golevka and Geographos. These results provide only a vague idea of the shape dependence of da/dt as function of various other
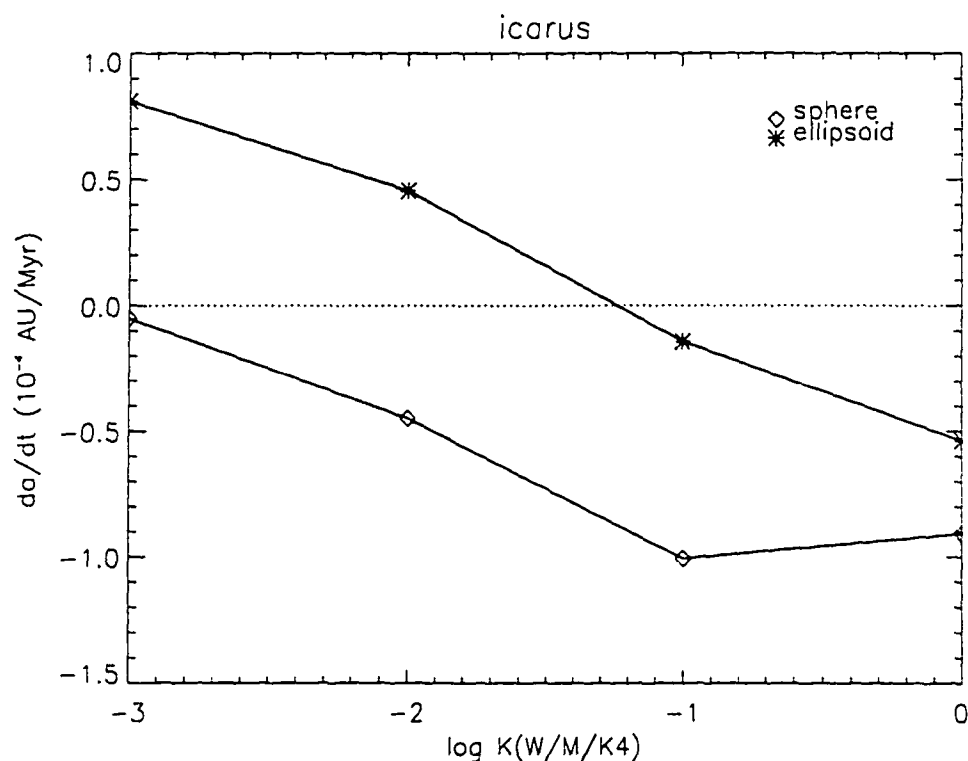
Figure 8.28: Rate of change of semimajor axis da/dt, caused by the Yarkovsky effect as a function of surface thermal conductivity k for two models of 1566 Icarus. Diamonds indicate results for a spherical body of radius 450 m. Asterices indicate results for an ellipsoid model with axes 578-, 470-, and 336 m.

parameters like spin axis direction, rotation period, and orbital elements and a more comprehensive survey would be necessary to map the parameter space adequately. Nevertheless, these results do strongly suggest that precise prediction of Yarkovsky perturbations for specific asteroids probably requires a thermal model that can take account of fairly complex shapes.

Although the results in Figs. 8.27, 8.28, and 8.29 produced using the finite-difference calculation are of a similar order of magnitude to those of Vokrouhlický

Figure 8.29: Rate of change of semimajor axis da/dt, caused by the Yarkovsky effect as a function of surface thermal conductivity k for two models of 1620 Geographos. Diamonds indicate results for a spherical body of radius 1210 m. Asterices indicate results for an ellipsoid model with axes 2381-, 2381-, and 863 m.

et al. (2000)[1], there are obvious discrepancies, suggesting again that a fairly sophisticated thermal model is required to predict the Yarkovsky effect on specific asteroids. In Chapter 11, I discuss the modifications required for the numerical approach to handle bodies with arbitrary shapes.

---

[1]Actually, the Golevka model used in this chapter does not correspond to that used in the published form of Vokrouhlický et al. (2000) because a more accurate spin axis was pointed out to them by a reviewer. Nevertheless, the results of the two models using the original spin axis agreed to order of magnitude.

CHAPTER 9

NEA HAZARDS – THE ROLE OF THE YARKOVSKY EFFECT

Sooner or later, our planet will be faced with the likelihood of a catastrophic impact. Indeed, not long ago, the roughly 1-km asteroid 1997 XF11 drew a considerable amount of attention when the suggestion was made (Marsden, 1999) that it could collide with the Earth in 2028. Although that particular warning turned out to be a false alarm, we know from the geologic record that several objects with diameters of several km have probably impacted the Earth during the past several hundred Myr. Such events may have been partially or completely responsible for the mass extinctions occurring at the Permian-Triassic (Erwin, 1994; Bowring et al., 1998) and Cretaceous-Tertiary boundaries (Kring, 1993). More recently, the Tunguska region of Siberia was impacted by a relatively small body whose physical characteristics remain unclear, but which caused a considerable amount of devastation.

In this chapter, I propose that radiation effects like the Yarkovsky effect may be exploited for the purpose of modifying the orbit of a potentially hazardous body so as to prevent it from colliding with the Earth.

9.1 Hazard Detection

The first step in avoiding an impact is to identify the danger as early as possible. Such advance warning requires an efficient survey of the sky to locate NEAs, measurement of a body's current orbit, and a prediction of its future orbit. The more precisely we know the current orbit and how it will evolve, the further into the future we can predict an impact, and the easier it will be to avoid.

Potential hazards are initially detected in sky surveys using telescopic observations. An example of such a survey is the Spacewatch program. Such optical observations provide relatively imprecise astrometry, but broad sky coverage, so they are useful in scanning the sky for NEAs. Spacewatch observations can be followed up using radar to refine the orbit determination. Radar measures a body's position and radial velocity with particularly high precision, typically ± 10 m in range and $\pm 10^{-4}$ m/s in radial velocity (Ostro, 2001).

Given precise knowledge of the current orbit, it is necessary to understand the gravitational and nongravitational perturbations to the orbit in order to predict the position of an asteroid at some time in the future. Gravitational perturbations are caused by the presence of other massive bodies in the solar system, nonsphericity of the sun, and general relativity corrections. These perturbations are quantitatively well understood and may be accounted for with high precision.

The nongravitational perturbations are caused by not only the Yarkovsky effect, but also by direct solar radiation pressure, Poynting-Robertson drag (anisotropic emission caused by the doppler effect), and the YORP effect (torque caused by anisotropic thermal radiation). The physical principles behind these radiation pressure effects are well understood, but their precise orbital perturbations are difficult to calculate because they may depend on an asteroid's shape, spin vector, composition, and details of its surface character.

Because the above nongravitational perturbations depend on many poorly-known parameters, our ability to predict future Earth hazards is currently limited by our understanding of these radiation pressure effects. For example, asteroid 1950 DA has one of the best-known orbits among NEAs and it is predicted to make a dangerously close approach to the Earth in 2880 (Giorgini, 2001). However, that prediction neglects the above radiation effects, thus a different outcome is possible if those effects are included.

9.2 Hazard Mitigation via the Yarkovsky effect

9.2.1 Theoretical speculation

Given the ability to compute radiative orbital element perturbations with the precision necessary for accurate forecasting of terrestrial impacts perhaps centuries into the future, such effects may provide a means of modifying the orbit of the projectile enough to avoid the collision.

In this chapter, I treat only the Yarkovsky effect quantitatively, both because it is probably the most important nongravitational perturbation for asteroids with diameters ranging from about a meter to several tens of kilometers, and because it is simpler to treat because it can be investigated for spherical bodies. Indeed, for such idealized spherical-asteroid calculations, direct solar radiation pressure does not cause secular orbit changes and the YORP effect does not operate at all. For asteroids with real shapes, these other effects may be important and deserve further attention, but a discussion of the Yarkovsky effect alone is sufficient for the purposes of this chapter.

Because the Yarkovsky effect arises from the surface temperatures on a body, it can be sensitive to various surface characteristics such as albedo, thermal conductivity, roughness, etc. Therefore, the body's Yarkovsky mobility may be drastically changed by modifying only the upper few centimeters of the surface.

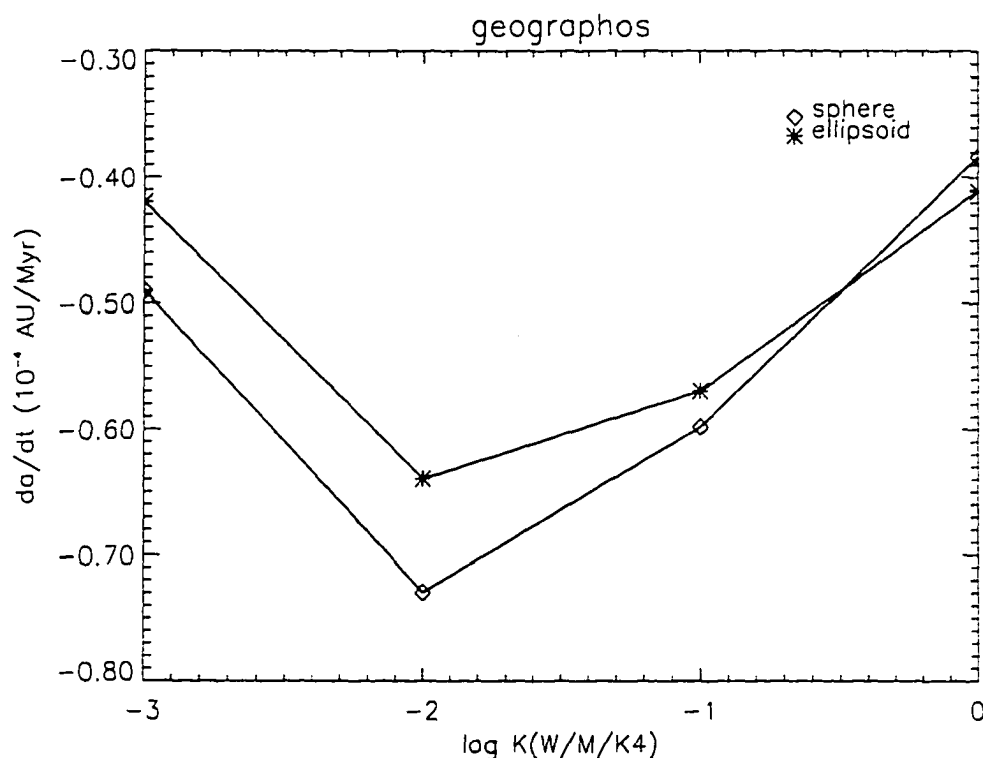For example, Fig. 9.30 shows the rate of change of semimajor axis da/dt caused by the Yarkovsky effect as a function of surface thermal conductivity k for model asteroids whose characteristics resemble those of the stony near-Earth asteroids 6489 Golevka, 1566 Icarus, and 1620 Geographos, with diameters of roughly 300 m, 1 km, and 2.5 km, respectively. These results were computed using the finite-difference method of Chapter 4. A thermal conductivity of $k = 10^{-3}$ W m^{-1} K^{-4} is roughly appropriate for loosely-consolidated regolith, while $k = 1$ W m^{-1} K^{-4} is more appropriate for a bare rock surface. To account for surface porosity,
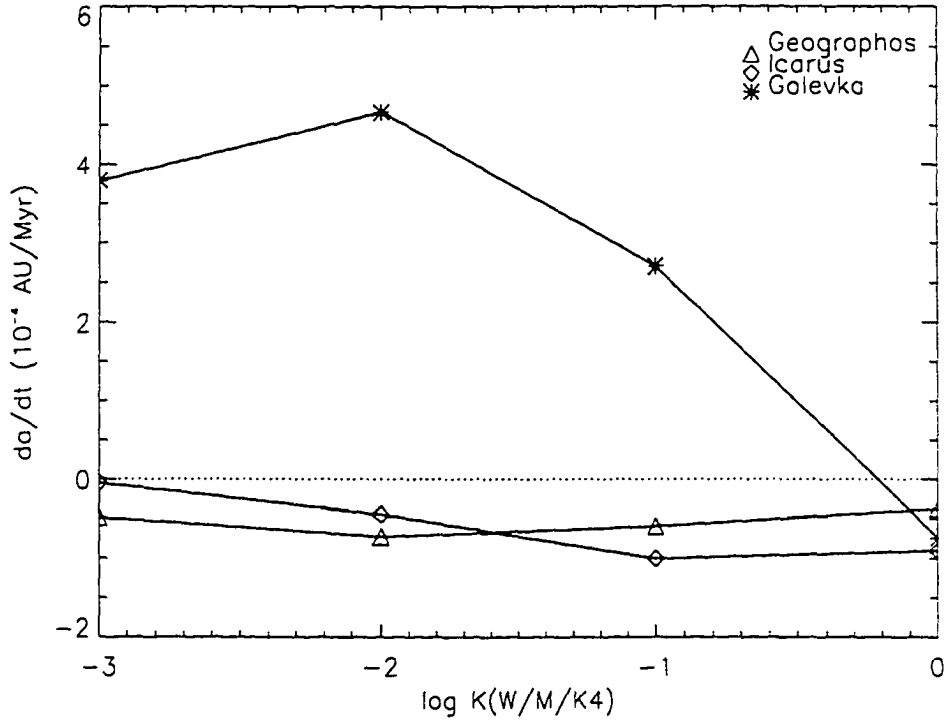
Figure 9.30: Rate of change of semimajor axis da/dt, caused by the Yarkovsky effect as a function of surface thermal conductivity k for models three different near Earth asteroids. Asterices indicate results for a spherical model of 6489 Golevka with radius 140 m. Diamonds indicate results for a spherical model of 1566 Icarus with radius 450 m. Triangles indicate results for a spherical model of 1620 Geographos with radius 1210 m. These results are replotted from Figs. 8.27, 8.28 and 8.29.

the surface density ρ_s is scaled with surface thermal conductivity as

$$\rho_s = \left[1500 + \frac{500}{3}(\log(k_s \ W^{-1} \ m \ K^4) + 3)\right] \ kg \ m^{-3}, \qquad (9.135)$$

while the density of the interior is varied so as to maintain a bulk density of 2000 kg m^{-3}, consistent with the approach of Vokrouhlický et al. (2000). Figure 9.30 shows that by changing the surface porosity, da/dt can be changed by 10^{-4} AU Myr^{-1} or more, depending on the body.

Assuming the Yarkovsky effect causes a to change at a constant rate da/dt during the period Δt, a body experiences a *displacement* Δr relative to its predicted

position on an unperturbed (by the Yarkovsky effect) orbit of approximately

$$\Delta r \simeq -\frac{3}{2}\mu^{1/2}a^{-3/2}\frac{da}{dt}(\Delta t)^2, \qquad (9.136)$$

where μ is the gravitational constant times the mass of the sun. Displacements associated with changes in all of the other orbital elements either oscillate or accumulate only linearly with time, so only the semimajor axis effect is important, as discussed in Chapter 8. By changing the surface thermal conductivity, one may change da/dt, producing an *offset* $\delta\Delta r$ relative to its predicted position assuming the original surface thermal conductivity given by

$$\delta\Delta r \simeq -\frac{3}{2}\mu^{1/2}a^{-3/2}\delta\left(\frac{da}{dt}\right)(\Delta t)^2. \qquad (9.137)$$

For the 1566 Icarus model of Fig. 9.30, the difference in da/dt between the bare-rock and porous regolith cases corresponds to an offset of about 1400 km in 100 yr, a substantial fraction of the Earth's radius. Because of the quadratic time-dependence in (9.136), that asteroid may be moved nearly ten times as far in 300 yr, virtually assuring a near miss instead of a collision. Conversely, because Yarkovsky da/dt scales roughly with the inverse of diameter, a 10-km body with similar characteristics could be moved over 1000 km during 300 yr. A Golevka-like body could be moved even further during those periods, mainly because of its smaller size. On the other hand, Geographos' mobility is not strongly dependent on k, so other means would need to be found to divert such a body.

What about metallic bodies? A bare metallic body in this size range would experience a considerably slower Yarkovsky da/dt than a stony body of similar size for several reasons. First, its greater thermal conductivity makes it more efficient at equalizing its surface temperatures, resulting in a smaller Yarkovsky force. Its higher thermal inertia does cause a larger component of that force to be tangential, favoring greater semimajor axis mobility, but the smaller overall force magnitude is the dominant effect. Second, its greater density results in smaller accelerations for the same force.

Despite the fact that metallic bodies tend to have smaller Yarkovsky mobilities than stony bodies, a substantial Yarkovsky effect might be induced/eliminated by the addition/removal of a thin ($\sim$ 1 cm) surface layer of insulating material. In that way, during similar periods, it may be possible to achieve offsets as great as perhaps a factor of two or three (corresponding to roughly a factor of two or three greater density for metals than for stones) smaller than for the stony bodies discussed above.

Another way to alter a body's Yarkovsky mobility is by changing its albedo. Since the Yarkovsky acceleration is roughly proportional to $1 - \Lambda$, where Λ is the bond albedo (see Chapter 3), changing the albedo from a fairly high value of 0.3 to, say, 0.05 would alter the Yarkovsky mobility by about 35%, for example. Larger effects might be attainable as well, and in some cases (Geographos, for example), this might be the optimum approach.

9.2.2 Implementation

I have demonstrated that it is possible in principle to change Yarkovsky mobilities of some hazardous asteroids enough to avoid potentially catastrophic impacts by altering their surface characteristics, but how can those surface alterations be implemented in practice? A detailed answer to that question is beyond the scope of this chapter, but I offer the following conjectures.

For a bare-rock or bare-metal body, one might blanket the asteroid with a 1-cm layer of highly-insulating material, a depth comparable to the penetration depth of the diurnal thermal wave. To blanket the surface of a 1-km body with such a layer would require about 250000 tons of dirt, the mass of roughly 90 fully-loaded Saturn V's. The cost of launching that much of material would be high and it would be difficult to deposit uniformly in the complex gravitational field of a small asteroid.

Blanketing would also be one way to modify a body's albedo. Such a change

could be achieved using much less material (say 1/10 as much) than required to change the conductivity to the depth of the diurnal thermal wave. Still, it would be difficult to deposit the material uniformly.

Perhaps instead, at least for a stony body, one might shatter the surface to a depth of a few centimeters by saturating the surface with conventional explosives, producing a porous regolith. However, such a small body may not retain much of that regolith. If, on the other hand, the hazardous body already possesses such a thin surface veneer (this would be more likely for a metallic body than for a stony body), it may be removed using explosives, thereby exposing a bare surface with considerably different thermal properties than the original. One ton of TNT could remove a 1-cm layer of loose material from the surface of a 1-km body if properly delivered.

Obviously, the solution must be taylored to the body in question and should not be undertaken without the ability to accurately predict the effect of such modifications.

9.3   Summary and Conclusions

Precise calculation of the Yarkovsky effect for a specific body requires (1) a mathematical formulation and (2) data regarding the relevant characteristics of the asteroid in question. Calculations of the Yarkovsky effect are currently performed by a number of authors (Rubincam, 1998; Vokrouhlický and Farinella, 1999), but those models are probably not yet sophisticated enough to yield precise mobilities for specific bodies. However, the numerical approach of Chapter 4 may soon approach the necessary level of sophistication. Currently, this finite-difference approach solves the full nonlinear, three-dimensional problem for bodies with ellipsoidal shapes and arbitrary structure. In the near future, this approach should have the ability to treat bodies of arbitrary shape. In principle, this type of approach can eventually be used solve the mathematical side of the problem very precisely.

I focused on the Yarkovsky effect in this chapter because it is generally the most important nongravitational perturbation for the bodies modeled here. However, except for Poynting-Robertson drag (which is only important for much smaller particles than discussed here) the other radiation effects mentioned here are not negligible. Fortunately, those effects can be studied using methods similar to those used to model the Yarkovsky effect on nonspherical bodies.

The problem of NEA hazard mitigation is in reality highly nonlinear. The calculations presented here do not account for the fact that small perturbations to an orbit can in fact cause large changes in the probability of a collision with the Earth at a given time in the future. There may be sets of initial conditions that yield high collision probabilities surrounded closely by regions that yield extremely small collision probabilities. It may require only a small velocity change to remove a body from such a parameter-space "keyhole" (Chodas, 1999). Therefore, it may in some cases be much easier to mitigate a hazard than I have suggested using the principles discussed simple-mindedly here.

A combined effort of theory and observation would help to test and constrain Yarkovsky calculations. The impending 2003 apparition of 6489 Golevka may provide such an opportunity. Vokrouhlický et al. (2000) estimate that, with the help of radar astrometry from earlier apparitions, that body may display a detectable Yarkovsky displacement.

In this chapter, I have demonstrated that the Yarkovsky effect may be useful for diverting some hazardous near-Earth asteroids and I have hazarded some conjectures as to how such measures may be implemented. However, regardless of whether such ideas are ever put into practice, without the ability to calculate the Yarkovsky effect precisely for specific bodies, our ability to predict Earth impacts will remain limited to the relatively near future.

CHAPTER 10

DISCUSSION AND CONCLUSIONS

In the work described in previous chapters, a fully-numerical, three-dimensional solution to the heat equation for an orbiting body in the solar radiation field was developed. This approach makes it possible to investigate the general Yarkovsky effect for parameters that have not been accessible to previous methods. This calculation has been validated against those of previous workers where results are available for comparison. I have validated this calculation with respect to timestep, spatial resolution and warmup period. I conclude that the results presented in this dissertation should generally be reliable to within a few percent.

10.1 Yarkovsky-assisted resonance escape

The results in Chapters 5 and 6 demonstrate that, for high eccentricity orbits, the Yarkovsky effect can produce very rapid changes in a and e. For example, in Fig. 5.13, a 1-m stony body with $a = 2.5$ and $e = 0.9$ experiences an Yarkovsky drift rate of about 1 AU in about 1.5 Myr. Given the uncertainties in thermal properties, it is plausible that the semimajor axis could change as fast 1 AU or more per million years for stony bodies with diameters of 1 m or so. It also appears that the rates could be substantially faster if e is increased beyond 0.9. Similarly, de/dt can be as fast as 0.1 per million years for such a body.

This high-e region of parameter space is relevant to the fate of small stony bodies trapped in the strong main-belt resonances. As discussed in Chapter 2, in the absence of the Yarkovsky effect, bodies trapped the strong main-belt resonances

have been shown to undergo rapid stochastic changes in e, approaching 1, causing most to become either sun-grazers or Jupiter-crossers on timescales of a few Myr (Farinella et al., 1994; Gladman et al., 1997). The only known removal mechanism is a planetary close encounter, but Gladman et al. (1997) showed that such encounters are not very efficient at removing bodies from such resonances. The results in Chapter 5 suggest the Yarkovsky effect as an alternative possible removal mechanism. Such a mechanism is most plausible for removal of bodies from secular resonances like the ν_6 because, unlike mean-motion resonances, secular resonances do not perturb the body's semimajor axis. As a body's eccentricity increases in the resonance, the Yarkovsky semimajor axis perturbation may become quite strong, depending on its spin axis orientation. In order for the body to escape from the resonance, its Yarkovsky da/dt must simply be fast enough for it to drift out of the resonance before it can be removed from the solar system. Moreover, very fast negative Yarkovsky de/dt could assist a particle in escaping the resonance by delaying its eventual high-eccentricity demise, while very fast positive Yarkovsky de/dt could hinder such an escape by hastening that demise.

10.1.1 Results as a function of rotation period

A major problem with the idea of Yarkovsky-assisted resonance escape is that the above rates of semimajor axis and eccentricity evolution were computed using a 5-h rotation period, which may be implausibly slow to be typical of such small bodies. Farinella et al. (1998) estimate that for asteroids the typical rotation period is:

$$p \sim 5\text{hr} \left(\frac{2\text{R}}{1\text{km}} \right). \qquad (10.138)$$

According to that estimate, for $R = 0.5, 5, 50$ m, typical periods should be ~ 18 s, 180 s and 30 min, respectively. Therefore, because the fast rates of change obtained in those surveys were all associated with strong diurnal effects, which depend on rotation rate, those rates might not be typical for real asteroids of such sizes.

Figure 10.31: (following page) (a) Magnitude F of the Yarkovsky acceleration vs. rotation period p for three radii R, with $a = 1$ AU, $e = 0$, $i = 0$, and $\iota = 0$. (b) Thermal lag angle δ vs. rotation period. (c) Transverse component of the Yarkovsky acceleration $F \sin \delta$ vs. rotation period; see text for a physical explanation of the various trends. For rotation periods estimated by Farinella (1998) (Eq. 10.138), the transverse acceleration (and hence da/dt and de/dt) is much smaller than with $p = 5$ h, the value used in our numerical simulations.

(a) F (m/s2) vs p (hr): R = 0.5 m, R = 5 m, R = 50 m

(b) sin δ vs p (hr): R = 0.5 m, R = 50 m, R = 5 m

(c) F sin δ (m/s2) vs p (hr): R = 0.5 m, R = 5 m, R = 50 m
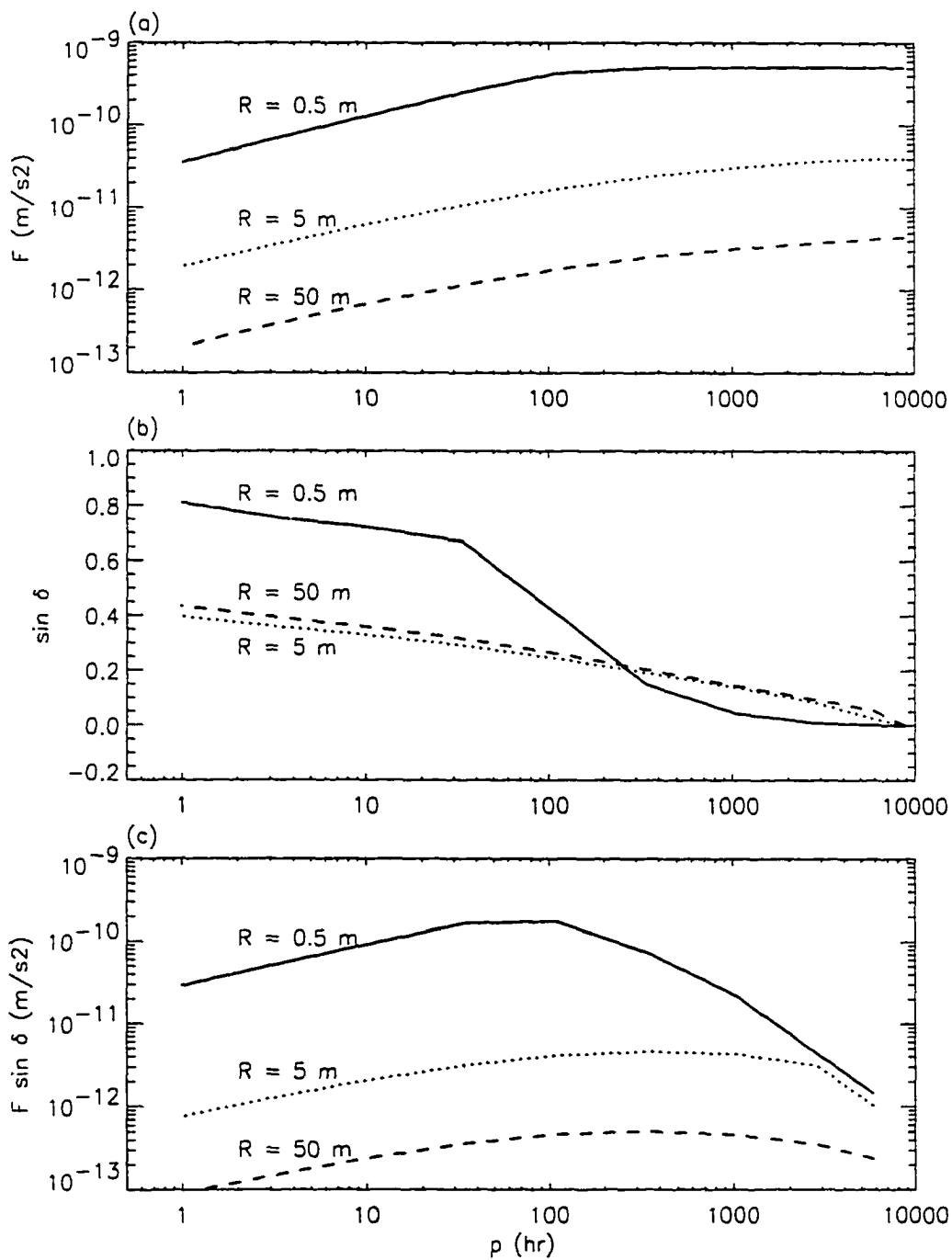
To demonstrate the dependence of the diurnal Yarkovsky effect on rotation rate, consider da/dt as a function of p with $e = 0$. In this case, only the transverse Yarkovsky acceleration contributes to da/dt. Fig. 10.31 shows the magnitude F of the instantaneous Yarkovsky acceleration and the instantaneous thermal lag angle δ as a function of rotation period for various size bodies with $e = 0$ and $a = 1$ AU. For fast rotation (e.g. $p < 100$ h), as the period becomes shorter, F becomes smaller because surface temperatures become smeared, and $\sin \delta$ becomes larger because the body rotates through a larger angle during the characteristic thermal response time. For slow rotation (e.g. $p > 100$ h), as the period becomes longer, F increases because the temperature distribution becomes more asymmetric, leveling off for the largest periods because the entire body becomes affected by the diurnal thermal wave, and $\sin \delta$ decreases to near zero. Therefore, the transverse acceleration component, $F \sin \delta$ (Fig. 10.31c), has a maximum at a period that depends on the size of the body. Since, for the $e = 0$ case, da/dt is proportional to $F \sin \delta$, Fig. 10.31c shows that da/dt could be an order of magnitude or more slower for bodies rotating at rates given by (10.138) than for bodies rotating with a 5-h period.

Now consider cases with $e > 0$, which are more relevant to the very fast rates (da/dt and de/dt) we are interested in. For the diurnal effect, the contributions to da/dt and de/dt due to the radial acceleration average to zero for any e, so (as in the case $e = 0$) only the transverse acceleration matters. Moreover, because for the diurnal effect, the results are dominated by what happens near pericenter (see Appendix C), Fig. 10.31 is still qualitatively useful. As with the $e = 0$ case, Fig. 10.31 implies that da/dt and de/dt would be about an order of magnitude or more slower for rotation rates given by Eq. (10.138). On the other hand, there is some reason to expect for some bodies that spin would be slower than Farinella et al. (1998) estimated. The so-called YORP effect (the effect of thermal reradiation forces in spin) may systematically decrease rotation rates for small bodies (Rubincam (2000), Vokrouhlický (in prep)).

The bottom line is this: If typical rotation rates really do follow the Farinella

et al. (1998) scaling, then bare-rock bodies are not likely to be removed from strong secular resonances by the Yarkovsky affect. However, such escape may be possible for bodies with insulated surfaces.

10.1.2 Bodies with an insulating regolith

Chapter 7 addressed changes in orbital elements for 10- and 100-m bodies covered by various thicknesses of a highly-insulating regolith. Because of the considerable time involved performing the calculations for the previous studies, this survey was more restricted. Nevertheless, many of the parameters investigated had never previously been addressed. Although the actual behavior (as a function of a and regolith fraction f_r) is difficult to summarize, for cases with low- to moderate eccentricity, semimajor-axis mobility caused by the pure diurnal effect (cases with $\iota = \pi$) can be enhanced by perhaps a factor of three (depending on a and e) by the addition of a "thick" regolith (thick enough the the diurnal thermal wave does not penetrate to the interior), while da/dt caused by the pure seasonal effect (approximated in that chapter by cases with $\iota = \pi/2$ and low- to moderate e) may be substantially inhibited by the addition of regolith.

The enhanced diurnal effect associated with the insulating regolith suggests that the above discussion regarding Yarkovsky-assisted resonance escape may be applicable to low-conductivity bodies a few times larger than 1 m. Such bodies would be expected to have rotation periods a few times longer than 1-m bodies, so the arguments regarding rotation rate are not as prohibitive. Moreover, because of the much lower thermal inertia of the insulating layer, such bodies would need to rotate much faster than similar bare-rock bodies in order to smear out their longitudinal temperature variations enough to eliminate their diurnal effect. Therefore, a Yarkovsky-assisted escape mechanism may work for small bodies with low-conductivity surfaces. However, as bodies of this size are unlikely to retain much loose surface material, it is still difficult to see how such a process could be

common.

Nevertheless, even given favorable rotation states and thermal properties, the question of whether the Yarkovsky effect can be important in the orbital evolution of small bodies in the strong main-belt resonances requires a detailed study of the orbital evolution of such bodies subject to the simultaneous influence of the Yarkovsky effect and gravitational perturbations. Such a studies is a topic for the future and will be discussed in more detail in the next chapter.

A final interesting comment regarding secular resonances concerns their semimajor axis positions. Results in Chapter 6 show that $d\varpi/dt$ caused by the Yarkovsky effect could be of order 0.1 per Myr, about 5% that associated with the ν_6 resonance. Therefore, under the influence of the Yarkovsky effect, the precise semimajor axis at which a body encounters such a resonance could depend on its thermal and spin properties. Again, however, a more detailed study is called for.

10.2 Non-principle-axis rotation

Another assumption (in addition to the slow spin rate) in the calculations used to generate the results in this dissertation that may be unrealistic for most small, real asteroids is that they spin about their principal axis of moment of inertia. Real asteroids, which are probably irregularly shaped, may wobble rather than rotate about the principal axis. For bodies with such irregular rotation states, the systematic effect that gives rise to cumulative Yarkovsky forces would be considerably reduced (Vokrouhlický (1998) made a preliminary attempt to address this issue).

According to Burns and Safronov (1973), stony, non-porous asteroids damp their free-precession in characteristic time

$$\tau_{\text{damp}} \sim \frac{5 \times 10^{10} \text{yr}}{K_3^2} \left(\frac{p}{1\text{hr}}\right)^3 \left(\frac{R}{1\text{m}}\right)^{-2}, \tag{10.139}$$

where K_3 is a shape factor varying from 10^{-2} for nearly spherical bodies to 10^{-1} for very oblate bodies. This damping could be fast compared to the age of the solar

system, but that alone does not mean that such bodies spend most of their time in principal-axis rotation. The problem is that they are continually impacted by other small bodies. The timescale for collisions to randomize the spin axis of a typical main-belt body is (Farinella et al., 1998)

$$\tau_{\text{reset}} \sim 7.24 \times 10^4 \text{yr} \left(\frac{p}{1\text{hr}}\right)^{-5/6} \left(\frac{R}{1\text{m}}\right)^{4/3}. \tag{10.140}$$

Only if $\tau_{\text{damp}} < \tau_{\text{reset}}$ can principal-axis rotation be common, so a rough indicator of principle-axis rotation for typical main-belt bodies of radius R spinning with period p is the value of the ratio ξ:

$$\xi \equiv \frac{\tau_{\text{damp}}}{\tau_{\text{reset}}} \simeq \frac{6.91 \times 10^5}{K_3^2} \left(\frac{p}{1\text{hr}}\right)^{23/6} \left(\frac{R}{1\text{m}}\right)^{-10/3}. \tag{10.141}$$

$\xi \ll 1$ suggests that most such bodies will be rotating about their principal axis, while $\xi \gg 1$ indicates that most are not. The rotational motion of asteroids with large ξ should be complex (Harris (1994) uses the term "tumbling"), while asteroids with ξ near unity are more likely to spend substantial time with roughly constant angular velocity about a fairly fixed axis, in which case calculations like the one presented in this chapter can be relevant.

Evaluating ξ (from Eq. (10.141)) for asteroids with rotation periods as given by Eq. (10.138) yields

$$\xi \simeq \frac{1.49 \times 10^{-2} \text{yr}}{K_3^2} \left(\frac{R}{1\text{m}}\right)^{1/2}. \tag{10.142}$$

For $R = 0.5$ to 50 m, ξ ranges from about 1 to 10 for highly oblate bodies or about 10^2 to 10^3 for nearly spherical bodies. Hence, among small main-belt asteroids, only the smallest non-spherical ones would be likely to spend much time in regular rotation. For bodies with 5-h rotation periods, as assumed in our calculations, ξ is extremely large, so these bodies generally tumble. For these bodies to rotate approximately about their principal axis, they must be placed directly in that state by a lucky impact.

In such a rare event, where a main-belt body finds itself in a state of slow, principal-axis rotation, that state would last for only

$$\tau_{\text{reset}} \sim 1.89 \times 10^4 \text{yr} \left(\frac{R}{1m} \right)^{4/3}, \qquad (10.143)$$

or $\sim 10^4$, 10^5 and 3×10^6 yr for 1-, 10-, and 100-m bodies respectively. Given the maximum de/dt in each of these cases, the change in e would be at most about 10^{-3} during the time τ_{reset}. In other words, such a favorable rotation state would be unlikely to persist long enough for the body to undergo significant orbital evolution.

For bodies not in the main belt, τ_{reset} should be much longer. According to Morbidelli and Gladman (1998), bodies with orbits completely interior to the main belt (aphelion < 2 AU) should not be uncommon. Such bodies are decoupled from the main-belt collisional environment so they might survive long enough to accumulate substantial Δa or Δe during a relatively improbable phase of slow, near-principal axis rotation. For example, a body with $a = 1.25$ AU and $e \sim 0.5$ would have its eccentricity damped away in a few Myr, or pumped back to the main belt in much less than 1 Myr. Note that the orbital change accumulated during such an unlikely period of favorable rotation would dominate the random walk associated with the diurnal Yarkovsky effect because more typical rotation states are not favorable for fast orbital change.

Even in the main belt, τ_{reset} could be longer than given by Eq. 10.143. The derivation of Eq. 10.143, from Farinella et al. (1998), assumed a particular size distribution for projectiles that is very uncertain in the size range (extremely small particles) that can reorient the spin axis of bodies discussed here. For example, for bodies with $R = 0.5$ m, the spin-resetting projectiles would be ~ 1 mm in radius. Such particles are influenced by forces that are not important for the larger main-belt asteroids, introducing considerable uncertainty into their size distribution. For example, bodies of this size should have their orbits circularized by Poynting-Robertson drag, reducing the relative velocity (and hence the ability to reset spin axes) of the impactors. Poynting-Robertson drag may also preferentially remove the

tiny projectiles through semimajor axis decay. Both of those considerations favor a larger value for τ_{reset} than that given in (10.140). On the other hand, if the typical grain size for stony bodies is of order 1 mm (Durda and Flynn, 1999), collisions may lead to an overabundance of mm-scale projectiles. That effect would reduce τ_{reset}. Thus, there is considerable uncertainty in the value of τ_{reset}. It is possible (e.g. for bodies with $R = 0.5$ m and $p = 5$ h), that τ_{reset} could be substantially longer than the estimate given by Farinella et al. (1998), so significant orbital evolution is not entirely ruled out, even in the main belt.

Moreover, there is considerable disagreement regarding the rotational damping timescale. For example, Efroimsky and Lazarian (2000) argue that the damping timescale given by Burns and Safronov (1973) is 10 – 100 times too long, but Burns and Sharma (2000) argue that the longer times are correct. If the shorter times are correct, then principal axis rotation should be much more common in the main belt than suggested by (10.141) so the relatively unlikely rotation states favorable to significant semimajor axis and eccentricity evolution as discussed above may not be so rare.

10.3 Models of specific near-Earth asteroids

The finite-difference approach is ideally suited to computing Yarkovsky perturbations for models of specific asteroids. As discussed in Chapters 8 and 9, such calculations are essential for generating extremely precise ephemerides, which are needed for a number of reasons. First, high-resolution radar imaging requires a prediction of a body's position and speed in order to track it adequately. Second, precise knowledge of a body's orbit and how it will evolve in the future allows prediction of near-earth asteroid hazards far enough into the future to have a chance of avoiding a catastrophic impact. Also, the Yarkovsky effect or similar a radiative reaction effect could conceivably be used to mitigate that hazard. Finally, precise Yarkovsky calculations can be compared with high-precision astrometric observations of NEAs

in order to possibly detect the effect directly. Such a detection may be possible during the 2003 radar observations of Golevka.

10.4 Concluding remarks

Changes in orbital elements due to the Yarkovsky effect depend sensitively on numerous poorly known parameters. What are typical thermal parameters? How is angular momentum distributed among small bodies? How are small bodies arranged internally? How sensitive is the Yarkovsky effect to the shape of a body? What are the effects of shadowing and self-heating by reradiation? What happens with nonprinciple-axis rotation? All of these are open questions.

Most of these outstanding questions could, in principle, be addressed using the numerical approach presented in this dissertation. Vokrouhlický and Farinella (1998) have considered ellipsoidal bodies with their plane-parallel treatment, a model that is valid only for large bodies. Vokrouhlický (1998) made a preliminary attempt to include non-principal-axis rotation in his linearized model. The finite-difference approach (with appropriate modifications) may form a basis for characterizing the Yarkovsky effect for these various more complex situations. Indeed, my approach is the only one available with the potential to treat bodies of arbitrary shape rigorously.

Through the surveys presented in this dissertation, the Yarkovsky effect on spherical bodies has now been investigated over a wide range orbital, spin, and thermal parameters. This investigation has contributed a broader understanding of the consequences of the Yarkovsky effect in many situations that had not previously been studied. Under certain circumstances, the Yarkovsky effect has been shown to be stronger than had been previously demonstrated. Extended studies may reveal additional circumstances under which the Yarkovsky effect is strong enough to play a role in the transport of small bodies in the solar system.

CHAPTER 11

FUTURE WORK

The power of the finite-difference approach for computing Yarkovsky perturbations has been demonstrated throughout this dissertation. Its validity is strongly supported by comparisons with previous studies in the limited cases where those simplified methods apply. Its validity is further supported by the qualitative physical explanations for various more complicated cases that could not have been treated using the simplified methods. In this chapter, I outline a number of projects that could build on this work.

11.1 Orbital integrations including Yarkovsky perturbations

Recall that all of the results in this dissertation were calculated using only two bodies – the sun and the asteroid – and that the calculation of orbital element changes caused by the Yarkovsky effect was performed in a purely perturbative manner. That is, the body's motion was influenced by only solar gravity and orbital elements changes were computed by simply averaging the Gauss equations over an orbit. However, because the code is really little more than the coupling of a general orbital integrator and a general thermal model, it is capable of operating in a more general mode than that used to generate the results presented throughout this dissertation. It is perfectly valid for one to include as many planets as desired and to allow the Yarkovsky accelerations to be included directly in the orbital integration at each timestep. The code could be allowed to run for millions of years and could, in principle, be used to investigate the consequences of the Yarkovsky effect along

virtually any phase space trajectory. Unfortunately, because the thermal model is computationally very expensive, such brute-force calculations are completely impractical because they would require enormous amounts of CPU time.

Instead, one might imagine using the results of these Yarkovsky effect surveys as a database from which orbital elements rates of change could be interpolated occasionally (say, every hundred years of simulation time) during an orbital integration. Such an approach is feasible in principle, but it requires a database that encompasses the entire range of parameters that a body is likely to encounter during the integration. The surveys presented in this dissertation are perhaps broad enough to be of limited use for such a procedure, but they are quite coarse in some dimensions. For example, all of the runs were performed at or near zero inclination. Of course, a zero-obliquity body on an inclined orbit is the same as a body with some obliquity on a zero-inclination orbit, so the information does exist in the survey. However, the range of possible spin directions is very coarsely sampled and all of the runs were performed with only a single rotation period. Extrapolation to other periods may be possible, but any such procedure would introduce model-dependencies and would diminish the generality of the approach. Therefore, a more comprehensive survey of the parameter space than even that contained in this dissertation would be required to make this a useful procedure.

Therefore, in my opinion, there are two applications for the general Yarkovsky calculation that would make it useful in the problem of direct orbital integrations that include Yarkovsky perturbations. The first application is simply as a tool for validation of the simplified models that are currently being used directly in orbital integrators (e.g. Bottke et al. (2000)). In this dissertation, I have directly compared the results of my finite-difference calculation to those of some simplified techniques and I have discussed the similarities and differences. This type of validation could be taken a step further by using the general calculation to verify the simplified Yarkovsky forces used throughout a particular run of interest. In other words, with no prior knowledge of how a body might wander in the

parameter space, one would perform a long-term orbital integration including simplified Yarkovsky forces and afterwards choose a number of points throughout the integration at which to validate the simplified Yarkovsky forces using the general calculation.

The second way in which the general calculation may be useful for direct orbital integrations is by using it to investigate narrow regions of parameter space throughout which some simple parametrizations of the general results are valid. For example, it may be interesting to study the evolution of a particle in a strong main-belt mean-motion or secular resonance with Yarkovsky perturbations included. Such resonances are quite narrow in semimajor axis, so Yarkovsky perturbations throughout the run could be assumed independent of a. Moreover, for sufficiently short integration times, one might neglect spin-axis reorientation effects and nodal and apsidal precession as well, parameterizing the Yarkovsky-induced orbital element rates of change as functions of only e or perhaps just e and i. Since particle orbits have already been investigated in the vicinity of strong resonances using a simplified Yarkovsky formulation (Bottke et al., 2000) which is not valid for eccentricities larger than about 0.5, integrations using the general calculation could be started with fairly large e, keeping integration times as short as possible.

11.2 Generalizing the thermal model

A number of problems exist that could be addressed using a more general thermal model – one that can treat bodies of any shape. As seen in Chapter 8, Yarkovsky perturbations on a body can be changed completely by simply changing from a spherical to an ellipsoidal model. Given precise information about all of the other characteristics of a body, there is no reason to expect that the Yarkovsky perturbations can be approximated accurately assuming such simple shapes. Moreover, For nonspherical bodies, other radiative effects – direct solar radiation pressure and

the YORP effect – become important and there is no reason to expect the ellipsoidal model to yield accurate estimates of those effects either. Therefore, in order to accurately compute the Yarkovsky effect for real bodies, the numerical model should be generalized to treat arbitrary shapes. As seen in previous chapters, such a capability is important for predicting future close approaches by asteroids to the Earth and for directly observing Yarkovsky displacements.

11.2.1 Additional thermal physics

A thermal model to treat arbitrary shapes must account for the effects of shadows and reradiation. These effects do not exist in the spherical and ellipsoidal models because those surfaces are everywhere convex. Fortunately, both of these effects can be treated using the same algorithm. At the beginning of a run, a list should be constructed for each surface cell. That list for a given surface cell keeps track of which other surface cells are above that cell's horizon. Obviously, those lists won't change, so this step only needs to be performed once. Also, the total solid angle subtended by the remaining visible sky should be computed and stored.

When the surface boundary condition is evaluated for a given surface cell, each cell above the horizon contributes thermal radiation and if any of those cells blocks the sun, then no solar radiation is absorbed. In order to maintain the proper radiative balance, thermal radiation is emitted only into the visible sky. The rest of the thermal radiation from this cell will have been accounted for as reradiation onto other surface cells once the boundary condition has been evaluated over the entire surface.

11.2.2 Zoning an arbitrary shape

In addition to new physics, the code will require a new zoning routine, one with the ability to create an appropriate spatial mesh for any given surface shape model.

Similar to the spherical and ellipsoidal cases, this mesh must have surface cells whose thicknesses are roughly uniform, being very thin at the surface (thin enough to resolve the surface temperature profile) and gradually increasing in thickness with depth. Obviously, for an irregular shape, it is not possible for the thicknesses of the interior cells at arbitrary depth to be uniform, but it should be sufficient for the cell thicknesses to gradually become less uniform with depth.

There is no simple way to zone such a mesh for an arbitrary shape. A simple spherical-coordinate zoning with uniform spacing in longitude and latitude like that used for the spherical case will not work because the vertices corresponding to uniform surface cell thicknesses cannot in general be made to fall on lines of constant θ and ϕ. Adherence to those radial lines is not strictly required, but it makes the problem of zoning an entire three-dimensional body much more tractable. For example, it would be possible, in principle, to implement a scheme whereby one adds uniformly-thick layers to an appropriately-shaped core without regard to those radial lines. However, in such a scheme it would be difficult to determine an appropriate core shape and radial vertex spacing (as a function of θ and ϕ) that would yield the desired shape at the surface. Another possibility would be to start at the surface and work inward, adding some specified number layers of uniformly thick cells. The problem with this scheme is that it may produce cells for which the volume calculation (which divides a cell into tetrahedra) would not be applicable.

Figure 11.32 shows one possible compromise. There are two steps to zoning this mesh. First, a simple spherical mesh (bounded by the darker surface in the figure) is constructed with surface cell thicknesses as uniform as possible. Next, a thin zone of cells, each layer of uniform thickness, whose vertices are not required to fall on the lines of constant θ and ϕ, is added to the outside of the model. If this surface zone is very thin compared to the radius of the body, then the final shape will not be substantially altered by its addition.
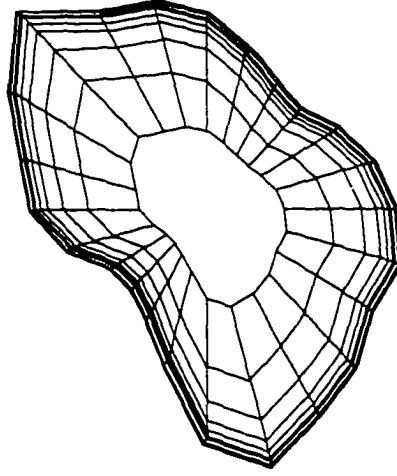
Figure 11.32: Cross section (about a plane of constant ϕ) through the spatial mesh corresponding to one possible way of zoning an irregularly-shaped body. In order to obtain the desired shape, most of the mesh (bounded by the dark surface) is constructed along lines of constant θ and ϕ. In order to achieve uniform surface cell thicknesses, a thin outer layer is zoned with uniform cell thicknesses.

11.3 Nonhomogeneous bodies

In this dissertation, I have examined homogeneous bodies and bodies with a highly-insulating surface layer. Other internal structures might also be interesting to study. For example, some asteroids might be porous throughout their interior. Radiative heat transfer would probably be important in the interiors of such bodies. Such transfer can be modeled using a temperature-dependent thermal conductivity of the form

$$k(T) = A + BT^3. \tag{11.144}$$

where the coefficients A and B are material-dependent. Cases with nonuniform surface albedo might also be interesting to study. The finite-difference code currently has the ability to model both of these configurations.

11.4 Modeling Infrared emission from small bodies

The finite-difference thermal model presented in this dissertation may be viewed as the latest in a series of progressively more sophisticated thermal models developed to treat specific applications. Spencer et al. (1989) generalized the then-current standard thermal model to include the effects of rotation, thereby producing more accurate models of asteroid infrared emission. That model relied on an assumption of plane-parallel heat flow, which is valid only for bodies larger than a few hundred meters. As smaller bodies were beyond the abilities of current observational methods, that model was adequate for its time. The analytical models currently used to compute Yarkovsky orbital perturbations (Rubincam, 1995; Vokrouhlický and Farinella, 1998), like the one presented in chapter 3, are yet more general because they include the effects of sphericity and can thus treat bodies the size of meteorite precursors, which are small enough that the plane-parallel heat-flow assumption is invalid. Now that decameter-scale bodies are being observed, the finite-difference thermal model presented in chapter 4, modified to treat arbitrary shapes, may be useful for computing infrared emission from such small bodies even if their shapes are highly nonspherical.

11.5 Development of a more accurate analytical insolation function

Recall from Chapter 3, that in the development of the linearized theory of the Yarkovsky effect, it is common to use a simplified form for the insolation function whereby one ignores its piecewise nature. In other words, integral (3.37) is simplified such that it is evaluated over the entire sphere instead of over only the sunlit hemisphere, as in (3.38). Such a simplification may cause substantial errors in the surface temperature asymmetry and thermal lag. If coefficients s_{pq} could be found that correspond to the original integral (3.37), then a more accurate linear theory would result.

APPENDIX A

A SUMMARY OF SYMPLECTIC INTEGRATION

The symplectic orbital integrator has become the standard tool for following the orbits of large numbers of particles for hundreds of Myr. In recent years, various workers have used symplectic integrators to study long-term dynamical behavior in the solar system (Wisdom, 1982; Gladman et al., 1997), illuminating a number of problems with the classical delivery scenario (see Chapter 2).

Those long-term studies have become feasible for a number of reasons. First, The symplectic nature of the integrators allows the to solution remain accurate over long integration times. Second, The codes tend to be very efficient because they are generally based on perturbed Kepler problems. Finally, computer speeds have continued to increase exponentially. The purpose of this appendix is to present a clear demonstration of the development of a number of symplectic integrators.

A.1 Formalism

A.1.1 Background

A symplectic map of order n is one that evolves the dynamical system forward in time an amount Δt according to a "surrogate" Hamiltonian that matches the exact Hamiltonian to order n in the Δt, but for which the dynamical problem is exactly integrable at each timestep. This property insures that the solution will remain valid (at least as a solution to the surrogate problem) over long integration times,

drifting only because of rounding errors. Presumably, solutions to the surrogate problem are similar to those for the actual problem.

The time evolution of a conservative dynamical system can be described by the Hamilton-Jacobi equations of motion (Goldstein, 1980)

$$\dot{q} = \frac{\partial H}{\partial p}$$
$$\dot{p} = -\frac{\partial H}{\partial q},$$
(A.145)

where $H(q,p,t)$ is the Hamiltonian and $q(t)$ and $p(t)$ are the generalized position and momentum, respectively. For the purposes of this discussion, $q(t)$ and $p(t)$ can be regarded as the actual position and momentum, but this need not be the case, as long as they are related by

$$p = \frac{\partial L}{\partial \dot{q}},$$
(A.146)

where $L(q,\dot{q},t)$ is the Lagrangian. For example, if the Hamiltonian is of the familiar form

$$H(q,p) = \frac{p^2}{2m} + V(q),$$
(A.147)

then the equations of motion are

$$\dot{q} = \frac{p}{m}$$
$$\dot{p} = -\frac{\partial V}{\partial q}.$$
(A.148)

As expected, the velocity is p/m and the force is $\partial V/\partial q$. Now introduce the *Poisson bracket*, defined as

$$\{f(q,p), g(q,p)\} = \frac{\partial f}{\partial q}\frac{\partial g}{\partial p} - \frac{\partial f}{\partial p}\frac{\partial g}{\partial q}.$$
(A.149)

Using this definition, the time derivative of a function may be written

$$\frac{df(q,p,t)}{dt} = \frac{\partial f}{\partial t} + \frac{\partial f}{\partial q}\frac{dq}{dt} + \frac{\partial f}{\partial p}\frac{dp}{dt}$$
$$= \frac{\partial f}{\partial t} + \frac{\partial f}{\partial q}\frac{\partial H}{\partial p} - \frac{\partial f}{\partial p}\frac{\partial H}{\partial q}$$
$$= \frac{\partial f}{\partial t} + \{f, H\}.$$
(A.150)

In particular, if $f(q,p,t) = q$ and $g(q,p,t) = p$, then

$$\frac{\partial f}{\partial t} = 0$$
$$\frac{\partial g}{\partial t} = 0, \qquad (A.151)$$

and

$$\dot{q} = \{q, H\}$$
$$\dot{p} = \{p, H\}. \qquad (A.152)$$

(A.152) and (A.145) are equivalent forms of the equations of motion.

A.1.2 Construction of a Symplectic Integrator

In this section, I present a straightforward method that can be used to construct a symplectic map of any order. The method presented here is based on an operator formalism and most closely follows that of Saha and Tremaine (1992). As examples, I derive first- and second-order maps, noting that under certain conditions, they correspond to well-known maps that have been in use for many years. Next I apply the second-order map more generally and discuss the idea of a so-called mixed variable symplectic integrator.

Begin by expanding the solution to the equations of motion in a Taylor series,

$$q(t_0 + \Delta t) = q(t_0) + \dot{q}(t_0)\Delta t + \frac{1}{2!}\ddot{q}(t_0)\Delta t^2 + O(\Delta t^3)$$
$$p(t_0 + \Delta t) = p(t_0) + \dot{p}(t_0)\Delta t + \frac{1}{2!}\ddot{p}(t_0)\Delta t^2 + O(\Delta t^3). \qquad (A.153)$$

Substituting (A.152), we have

$$q(t_0 + \Delta t) = q(t_0) + \{q, H\}|_{t_0} \Delta t + \frac{1}{2!}\{\{q, H\}, H\}|_{t_0} \Delta t^2 + O(\Delta t^3)$$
$$p(t_0 + \Delta t) = p(t_0) + \{p, H\}|_{t_0} \Delta t + \frac{1}{2!}\{\{p, H\}, H\}|_{t_0} \Delta t^2 + O(\Delta t^3) \qquad (A.154)$$

If we define a Poisson bracket operator, $\hat{H}$ as

$$\hat{H}f(q,p) = \{f(q,p), H\}, \qquad (A.155)$$

then expansion (A.154) can be written

$$q(t_0 + \Delta t) = \sum_{n=0}^{\infty} \frac{(\hat{H}\Delta t)^n}{n!} q(t_0) = e^{\hat{H}\Delta t} q(t_0)$$

$$p(t_0 + \Delta t) = \sum_{n=0}^{\infty} \frac{(\hat{H}\Delta t)^n}{n!} p(t_0) = e^{\hat{H}\Delta t} p(t_0). \qquad (A.156)$$

$e^{\hat{H}\Delta t}$ is the *evolution operator* that moves the system forward in time according to the Hamiltonian, H, by an amount Δt. In general however, this operator cannot be explicitly evaluated, and it is necessary to search for an approximate operator that can be explicitly evaluated and which evolves the system according to a Hamiltonian that matches the true Hamiltonian to some order in Δt. In this derivation, I assume that the Hamiltonian can be separated,

$$H = H_0(q,p) + H'(q), \qquad (A.157)$$

such that the equations of motion associated with $H_0(q,p)$ are integrable and $H'(q)$ contains all other perturbations. Note that $H'(q)$ depends only on position and not momentum. The unperturbed evolution operator, $e^{\hat{H}_0\Delta t}$, can, by definition, be explicitly evaluated. The perturbation evolution operator, $e^{\hat{H}'\Delta t}$, can also be evaluated explicitly, as follows. The equations of motion associated with the perturbation Hamiltonian are

$$\dot{q} = \frac{\partial H'}{\partial p} = 0$$

$$\dot{p} = -\frac{\partial H'}{\partial q}. \qquad (A.158)$$

Since q is constant according to the first relation, $\partial H'/\partial q$ is also constant since it is a function of only q. Thus, integration of (A.158) gives for the evolution caused by the perturbation Hamiltonian

$$q(t_0 + \Delta t) = e^{\hat{H}'\Delta t} q(t_0) = q(t_0),$$

$$p(t_0 + \Delta t) = e^{\hat{H}'\Delta t} p(t_0) = p(t_0) - \left. \frac{\partial H'}{\partial q} \right|_{q(t_0)} \Delta t. \qquad (A.159)$$

This result can also be obtained by explicitly evaluating the Poisson brackets in (A.154). Equations (A.159) state that evaluation of $e^{\hat{H}'\Delta t}$ corresponds to computing all of the perturbing forces at some time and applying them as impulses over the interval Δt. Since $e^{\hat{H}_0\Delta t}$ and $e^{\hat{H}'\Delta t}$ can be evaluated separately, we search for some product of these operators to approximate the true evolution operator, such that

$$e^{(\hat{H}_0+\hat{H}')\Delta t + O(\Delta t^n)} = e^{a_1\hat{H}_0\Delta t}e^{b_1\hat{H}'\Delta t}e^{a_2\hat{H}_0\Delta t}e^{b_2\hat{H}'\Delta t}\ldots e^{a_n\hat{H}_0\Delta t}e^{b_n\hat{H}'\Delta t}. \qquad (A.160)$$

The constants (a_i, b_i) can be determined using the *Hausdorf identity*,

$$e^{\hat{A}\tau}e^{\hat{B}\tau} = \exp\left\{(\hat{A}+\hat{B})\tau + \frac{1}{2}[\hat{A},\hat{B}]\tau^2 + O(\tau^3)\right\}, \qquad (A.161)$$

where $\hat{A}$ and $\hat{B}$ are operators and $[\hat{A},\hat{B}]$ denotes their commutator. The preferred solution usually involves the fewest possible nonzero constants, (a_i, b_i). Moreover, since the evaluation of the perturbation Hamiltonian is usually the most computationally expensive operation, it is often desirable to minimize the number of nonzero b_i as opposed to the number of nonzero a_i.

Equations (A.159) describe how a particular evolution operator, $e^{\hat{H}'\Delta t}$, operates on the position and momentum. In the following sections, a more general relation will be needed that describes how to operate on an arbitrary function of the position and momentum with an arbitrary evolution operator. Consider operating on some function $f(q, p)$, of the position and momentum with some evolution operator, $e^{\hat{H}\Delta t}$. Using the definition of the evolution operator,

$$\begin{aligned}
e^{\hat{H}\Delta t}f(q(t_0), p(t_0)) &= f(q(t_0), p(t_0)) + \Delta t\,\{f(q,p), H\}|_{(q(t_0), p(t_0))} + \\
&\quad + \frac{1}{2!}\Delta t^2\,\{\{f(q,p), H\}, H\}|_{(q(t_0), p(t_0))} + O(\Delta t^3) \\
&= f(q(t_0), p(t_0)) + \Delta t\dot{f}(q(t_0), p(t_0)) + \\
&\quad + \frac{1}{2!}\Delta t^2\ddot{f}(q(t_0), p(t_0)) + O(\Delta t^3) \\
&= f(q(t_0 + \Delta t), p(t_0 + \Delta t)) \\
&= f(e^{\hat{H}\Delta t}q(t_0), e^{\hat{H}\Delta t}p(t_0)), \qquad (A.162)
\end{aligned}$$

since $q(t_0 + \Delta t)$ and $p(t_0 + \Delta t)$ refer to the values of q and p after evolving a time Δt according to the Hamiltonian, H. Thus, the effect of the evolution operator on

a function of position and momentum is to cause the function to be evaluated using the evolved values of the position and momentum.

First-Order Integrator

For the first-order integrator, write

$$e^{(\hat{H}_0 + \hat{H}')\Delta t + O(\Delta t^2)} = e^{a_1 \hat{H}_0 \Delta t} e^{b_1 \hat{H}' \Delta t} e^{a_2 \hat{H}_0 \Delta t} e^{b_2 \hat{H}' \Delta t}. \qquad (A.163)$$

It will be seen shortly that more constants have been included in (A.163) than necessary for a first-order integrator. This is because we don't know apriori how many constants to include[1], so we keep our options open by including (hopefully) too many. If we wind up with degenerate solutions, then we have included too many constants, but we know that we have completely explored the parameter space. Using (A.161), and retaining only terms that are first-order in Δt, we obtain

$$(\hat{H}_0 + \hat{H}')\Delta t = [\hat{H}_0(a_1 + a_2) + \hat{H}'(b_1 + b_2)]\Delta t. \qquad (A.164)$$

This requires

$$a_1 + a_2 = 1$$
$$b_1 + b_2 = 1. \qquad (A.165)$$

There are four solutions for which the number of non-zero constants is the minimum, two:

$$(a_1, b_1, a_2, b_2) = (1, 1, 0, 0)$$
$$(a_1, b_1, a_2, b_2) = (1, 0, 0, 1)$$
$$(a_1, b_1, a_2, b_2) = (0, 0, 1, 1)$$
$$(a_1, b_1, a_2, b_2) = (0, 1, 1, 0). \qquad (A.166)$$

The second and third solutions are equivalent to the first, so there are really only two distinct solutions involving only two non-zero constants. Also, note that these

---

[1]There is probably a theorem addressing this.

two distinct solutions could have been obtained by including only three constants instead of four in (A.163). Moreover, if only two constants had been included, then only one of these solutions would have been found. The maps corresponding to the two non-degenerate solutions of (A.166) are

$$q(t_0 + \Delta t) = e^{\hat{H}_0 \Delta t} e^{\hat{H}' \Delta t} q(t_0) = e^{\hat{H}_0 \Delta t} q(t_0)$$

$$p(t_0 + \Delta t) = e^{\hat{H}_0 \Delta t} e^{\hat{H}' \Delta t} p(t_0) = e^{\hat{H}_0 \Delta t} \left\{ p(t_0) - \left. \frac{\partial H'}{\partial q} \right|_{q(t_0)} \Delta t \right\} \quad \text{(A.167)}$$

and

$$q(t_0 + \Delta t) = e^{\hat{H}' \Delta t} e^{\hat{H}_0 \Delta t} q(t_0)$$

$$p(t_0 + \Delta t) = e^{\hat{H}' \Delta t} e^{\hat{H}_0 \Delta t} p(t_0), \quad \text{(A.168)}$$

where equations (A.159) have been used to obtain the final form of (A.167). Thus, a first-order integrator is obtained regardless of the order in which the components of the Hamiltonian are evaluated. If, for H_0, we use a free particle Hamiltonian,

$$H_0 = \frac{p^2}{2m}, \quad \text{(A.169)}$$

then we have,

$$e^{\hat{H}_0 \Delta t} q(t_0) = q(t_0) + \frac{p(t_0)}{m} \Delta t$$

$$e^{\hat{H}_0 \Delta t} p(t_0) = p(t_0). \quad \text{(A.170)}$$

Equation (A.162) implies

$$e^{\hat{H}_0 \Delta t} \left. \frac{\partial H'}{\partial q} \right|_{q(t_0)} = \left. \frac{\partial H'}{\partial q} \right|_{q(t_0) + \frac{p(t_0)}{m} \Delta t}, \quad \text{(A.171)}$$

so the explicit first-order maps associated with the free-particle unperturbed Hamiltonian are

$$q(t_0 + \Delta t) = q(t_0) + \frac{p(t_0)}{m} \Delta t$$

$$p(t_0 + \Delta t) = p(t_0) - \left. \frac{\partial H'}{\partial q} \right|_{q(t_0)} \Delta t \quad \text{(A.172)}$$

.

and

$$
\begin{aligned}
q(t_0 + \Delta t) &= q(t_0) + \frac{p(t_0)}{m}\Delta t \\
p(t_0 + \Delta t) &= p(t_0) - \left.\frac{\partial H'}{\partial q}\right|_{q(t_0)+\frac{p(t_0)}{m}\Delta t} \Delta t.
\end{aligned} \tag{A.173}
$$

Second-Order Integrator

Higher-order maps may be derived in a manner analogous to the first-order integrators of the previous section. For the second-order integrator, just as for the first-order integrator, we write

$$
e^{(\hat{H}_0 + \hat{H}')\Delta t + O(\Delta t^2)} = e^{a_1 \hat{H}_0 \Delta t} e^{b_1 \hat{H}' \Delta t} e^{a_2 \hat{H}_0 \Delta t} e^{b_2 \hat{H}' \Delta t}. \tag{A.174}
$$

It will once again be seen that we have included more constants than necessary for our purposes. Using (A.161), and retaining only first- and second-order terms, the constants (a_1, b_1, a_2, b_2) must satisfy

$$
\begin{aligned}
(\hat{H}_0 + \hat{H}')\Delta t &\doteq \{\hat{H}_0(a_1 + a_2) + \hat{H}'(b_1 + b_2)\}\Delta t + \\
&+ \frac{1}{2}[\hat{H}_0, \hat{H}']\{(a_1 - a_2)b_1 + (a_1 + a_2)b_2\}\Delta t^2.
\end{aligned} \tag{A.175}
$$

This requires

$$
\begin{aligned}
a_1 + a_2 &= 1 \\
b_1 + b_2 &= 1 \\
(a_1 - a_2)b_1 + (a_1 + a_2)b_2 &= 0.
\end{aligned} \tag{A.176}
$$

Equations (A.176) are underconstrained and amount to

$$
a_2 b_1 = \frac{1}{2}. \tag{A.177}
$$

Thus, as in the case of the first-order integrator, there are an infinite number of choices for the constants (a_1, b_1, a_2, b_2). Since the bulk of the computation is usually associated with the perturbation Hamiltonian, H', we would like to set either $b_1 = 0$

or $b_2 = 0$ so that H' will need to be evaluated only once. Equation (A.177) rules out $b_1 = 0$, so we have

$$a_1 = \frac{1}{2}, a_2 = \frac{1}{2}, b_1 = 1, b_2 = 0, \tag{A.178}$$

and the map is

$$
\begin{aligned}
q(t_0 + \Delta t) &= e^{\tilde{H}_0 \Delta t/2} e^{\tilde{H}' \Delta t} e^{\tilde{H}_0 \Delta t/2} q(t_0) \\
p(t_0 + \Delta t) &= e^{\tilde{H}_0 \Delta t/2} e^{\tilde{H}' \Delta t} e^{\tilde{H}_0 \Delta t/2} p(t_0).
\end{aligned}
\tag{A.179}
$$

Using (A.170) and (A.162), the explicit second-order map associated with the free-particle unperturbed Hamiltonian is

$$
\begin{aligned}
q(t_0 + \Delta t) &= q(t_0) + \Delta t \frac{p(t_0)}{m} - \frac{\Delta t^2}{2m} \left. \frac{\partial H'}{\partial q} \right|_{q(t_0) + \frac{1}{2}\frac{p(t_0)}{m}\Delta t} \\
p(t_0 + \Delta t) &= p(t_0) - \Delta t \left. \frac{\partial H'}{\partial q} \right|_{q(t_0) + \frac{1}{2}\frac{p(t_0)}{m}\Delta t}.
\end{aligned}
\tag{A.180}
$$

According to (A.179), the second-order map corresponds to evolving the system 1/2 timestep using the unperturbed Hamiltonian, then kicking it with the perturbation Hamiltonian to change the elements, then evolving to the end of the timestep, again using the unperturbed Hamiltonian. This can be seen more explicitly by noting that (A.180) can be rewritten as

$$
\begin{aligned}
q_{1/2} &= q(t_0) + \frac{1}{2}\frac{p(t_0)}{m}\Delta t \\
p(t_0 + \Delta t) &= p(t_0) - \Delta t \left. \frac{\partial H'}{\partial q} \right|_{q_{1/2}} \\
q(t_0 + \Delta t) &= q_{1/2} + \frac{1}{2}\frac{p(t_0 + \Delta t)}{m}\Delta t.
\end{aligned}
\tag{A.181}
$$

Equations (A.181) comprise a method known by a number of names – *modified Euler, leapfrog*, and *midpoint rule*. It will be referred to as the leapfrog method in this work. Regardless of the name, this method is well-known and is classified as a Runge-Kutta scheme of order two.

Recall that, by construction, this second-order map requires only one evaluation of the perturbation Hamiltonian, just as in the first-order case. Since most of the computation is usually associated with this operation, the second-order map is not much more costly than the first-order map, but is accurate to order $(\Delta t)^2$. Third-order maps are known that require three such evaluations, but none that require any fewer (Wisdom and Holman, 1991). Thus, it is rarely worthwhile to use maps of order greater than two since the gain in accuracy is likely to be accompanied by an increased computational expense. For this reason, the second-order map is the most widely used (Wisdom and Holman, 1991; Yoshida, 1993; Levison and Duncan, 1994), although not in the form of equations (A.181), as discussed in the next section.

Mixed Variable Symplectic Integrator

In the previous section, a second-order map was constructed, equations (A.179), and then specialized for the case of a free-particle unperturbed Hamiltonian, resulting in the leapfrog map, equations (A.181). However, many problems in celestial mechanics involve motion that differs from two-body, Keplerian motion by only a small amount. This motivates the search for a suitable Kepler Hamiltonian for the unperturbed motion instead of the free-particle Hamiltonian used above. For the general N-body problem, the Hamiltonian is

$$H = \sum_{i=0}^{N-1} \frac{p_i^2}{2m_i} - \sum_{i=0}^{N-1} \sum_{j=i+1}^{N-1} \frac{Gm_i m_j}{|\mathbf{r}_i - \mathbf{r}_j|}. \tag{A.182}$$

We seek a separation such that the unperturbed Hamiltonian is of the form

$$H_0 = \sum_{i=0}^{N-1} \left(\frac{p_i'^2}{2m_i'} - \frac{\mu}{r_i'} \right), \tag{A.183}$$

such that the interaction Hamiltonian is small and depends only on the $\mathbf{r}_i'$. The separation is achieved via a canonical transformation to *Jacobi Coordinates* (Wisdom and Holman, 1991). Cartesian position vectors, $\mathbf{r}_i$, are transformed to Jacobi

coordinates, $\mathbf{r}'_i$, as

$$\mathbf{r}'_0 = \frac{1}{\mathcal{M}_{N-1}} \sum_{j=0}^{N-1} m_j \mathbf{r}_j \qquad (A.184)$$

$$\mathbf{r}'_{i>0} = \mathbf{r}_i - \frac{1}{\mathcal{M}_{i-1}} \sum_{j=0}^{i-1} m_j \mathbf{r}_j,$$

where

$$\mathcal{M}_i = \sum_{j=0}^{i} m_j. \qquad (A.185)$$

In other words, $\mathbf{r}'_i$ is the position of body i with respect to the center of mass of all of the bodies $j < i$. To determine the appropriate conjugate momenta, consider the Lagrangian in terms of the transformed variables:

$$L = \sum_{i=0}^{N-1} \frac{1}{2} m'_i (\dot{\mathbf{r}}'_i \cdot \dot{\mathbf{r}}'_i) + f(\mathbf{r}'_i), \qquad (A.186)$$

where the m'_i are the transformed masses and the terms $f(\mathbf{r}'_i)$, which do not depend on $\dot{\mathbf{r}}'_i$, are not of immediate interest. The Jacobi momenta as given by (A.146) are then

$$\mathbf{p}'_i = \nabla_{\dot{\mathbf{r}}'_i} L = m'_i \dot{\mathbf{r}}'_i. \qquad (A.187)$$

Differentiating (A.185) and multiplying by the appropriate transformed mass, we obtain the transformed momenta

$$\mathbf{p}'_0 = \frac{m'_0}{\mathcal{M}_{N-1}} \sum_{j=0}^{N-1} \mathbf{p}_j \qquad (A.188)$$

$$\mathbf{p}'_{i>0} = \frac{m'_i}{m_i} \mathbf{p}_i - \frac{m'_i}{\mathcal{M}_{i-1}} \sum_{j=0}^{i-1} \mathbf{p}_j,$$

where the m'_i will be determined so as to obtain the desired form for the separated Hamiltonian.

To find the form of the separated Hamiltonian, we first invert the transformation. Equations (A.185) can be rewritten as

$$\mathbf{r}'_0 = \frac{1}{\mathcal{M}_{N-1}} \sum_{j=0}^{N-2} m_j \mathbf{r}_j + \frac{m_{N-1}}{\mathcal{M}_{N-1}} \mathbf{r}_{N-1} \qquad (A.189)$$

$$\mathbf{r}'_{i>0} = \mathbf{r}_i - \frac{1}{\mathcal{M}_{i-1}} \sum_{j=0}^{i-2} m_j \mathbf{r}_j - \frac{m_{i-1}}{\mathcal{M}_{i-1}} \mathbf{r}_{i-1}, \qquad (A.190)$$

which can be rearranged,

$$\mathbf{r}_{N-1} = \frac{\mathcal{M}_{N-1}}{m_{N-1}}\mathbf{r}_0' - \frac{1}{m_{N-1}}\sum_{j=0}^{N-2} m_j\mathbf{r}_j \qquad (A.191)$$

$$m_j\mathbf{r}_j = \mathcal{M}_j(\mathbf{r}_{j+1} - \mathbf{r}_{j+1}') - \sum_{k=0}^{j-1} m_k\mathbf{r}_k \quad (j \le N-2). \qquad (A.192)$$

Substituting (A.192) into (A.191),

$$
\begin{aligned}
\mathbf{r}_{N-1} &= \frac{\mathcal{M}_{N-1}}{m_{N-1}}\mathbf{r}_0' - \frac{1}{m_{N-1}}\sum_{j=0}^{N-2}\left[\mathcal{M}_j(\mathbf{r}_{j+1} - \mathbf{r}_{j+1}') - \sum_{k=0}^{j-1} m_k\mathbf{r}_k\right] \\
&= \frac{\mathcal{M}_{N-1}}{m_{N-1}}\mathbf{r}_0' - \frac{1}{m_{N-1}}\sum_{j=0}^{N-3}\left[\mathcal{M}_j(\mathbf{r}_{j+1} - \mathbf{r}_{j+1}') - \sum_{k=0}^{j-1} m_k\mathbf{r}_k\right] \\
&\quad - \frac{1}{m_{N-1}}\left[\mathcal{M}_{N-2}(\mathbf{r}_{N-1} - \mathbf{r}_{N-1}') - \sum_{k=0}^{N-3} m_k\mathbf{r}_k\right].
\end{aligned}
$$

Solving for $\mathbf{r}_{N-1}$,

$$\mathbf{r}_{N-1} = \mathbf{r}_0' + \frac{\mathcal{M}_{N-2}}{\mathcal{M}_{N-1}} - \frac{1}{\mathcal{M}_{N-1}}\sum_{j=0}^{N-3}\left[\mathcal{M}_j(\mathbf{r}_{j+1} - \mathbf{r}_{j+1}') - \sum_{k=0}^{j-1} m_k\mathbf{r}_k - m_j\mathbf{r}_j\right]. \qquad (A.193)$$

According to (A.192), the term in brackets is zero, so

$$\mathbf{r}_{N-1} = \mathbf{r}_0' + \frac{\mathcal{M}_{N-2}}{\mathcal{M}_{N-1}}\mathbf{r}_{N-1}'. \qquad (A.194)$$

Substituting (A.192) into (A.190),

$$
\begin{aligned}
\mathbf{r}_{i>0}' &= \mathbf{r}_i - \frac{1}{\mathcal{M}_{i-1}}\sum_{j=0}^{i-2}\left[\mathcal{M}_j(\mathbf{r}_{j+1} - \mathbf{r}_{j+1}') - \sum_{k=0}^{j-1} m_k\mathbf{r}_k\right] - \frac{m_{i-1}}{\mathcal{M}_{i-1}}\mathbf{r}_{i-1} \\
&= \mathbf{r}_i - \frac{1}{\mathcal{M}_{i-1}}\sum_{j=0}^{i-3}\left[\mathcal{M}_j(\mathbf{r}_{j+1} - \mathbf{r}_{j+1}') - \sum_{k=0}^{j-1} m_k\mathbf{r}_k\right] \\
&\quad - \frac{\mathcal{M}_{i-2}}{\mathcal{M}_{i-1}}(\mathbf{r}_{i-1} - \mathbf{r}_{i-1}') + \sum_{k=0}^{i-3} m_k\mathbf{r}_k - \frac{m_{i-1}}{\mathcal{M}_{i-1}}\mathbf{r}_{i-1} \\
&= \mathbf{r}_i - \frac{1}{\mathcal{M}_{i-1}}\sum_{j=0}^{i-3}\left[\mathcal{M}_j(\mathbf{r}_{j+1} - \mathbf{r}_{j+1}') - \sum_{k=0}^{j-1} m_k\mathbf{r}_k + m_j\mathbf{r}_j\right] \\
&\quad - \mathbf{r}_{i-1}\left[\frac{\mathcal{M}_{i-2}}{\mathcal{M}_{i-1}} - \frac{m_{i-1}}{\mathcal{M}_{i-1}}\right] + \frac{\mathcal{M}_{i-2}}{\mathcal{M}_{i-1}}\mathbf{r}_{i-1}'.
\end{aligned}
$$

The first term in brackets is zero and the second term in brackets is one, so solving for $\mathbf{r}_{i-1}$ and then making the replacement $i - 1 \rightarrow i$ gives the useful relation,

$$\mathbf{r}_i = \mathbf{r}_{i+1} - \mathbf{r}'_{i+1} + \frac{\mathcal{M}_{i-1}}{\mathcal{M}_i}\mathbf{r}'_i \quad (i > 0). \tag{A.195}$$

Using (A.195),

$$\mathbf{r}_{i+1} = \mathbf{r}_{i+2} - \mathbf{r}'_{i+2} + \frac{\mathcal{M}_i}{\mathcal{M}_{i+1}}\mathbf{r}'_{i+1} \tag{A.196}$$

$$\mathbf{r}_{i+2} = \mathbf{r}_{i+3} - \mathbf{r}'_{i+3} + \frac{\mathcal{M}_{i+1}}{\mathcal{M}_{i+2}}\mathbf{r}'_{i+2}$$

$$\vdots$$

$$\mathbf{r}_{N-2} = \mathbf{r}_{N-1} - \mathbf{r}'_{N-1} + \frac{\mathcal{M}_{N-3}}{\mathcal{M}_{N-2}}\mathbf{r}'_{N-2}.$$

Substituting (A.196) into (A.195) and using (A.194),

$$\mathbf{r}_i = \mathbf{r}_{N-1} - \mathbf{r}'_{N-1} + \frac{\mathcal{M}_{N-3}}{\mathcal{M}_{N-2}}\mathbf{r}'_{N-2} - \mathbf{r}'_{N-2} + \dots \tag{A.197}$$

$$+\frac{\mathcal{M}_{i+1}}{\mathcal{M}_{i+2}}\mathbf{r}'_{i+2} - \mathbf{r}'_{i+2} + \frac{\mathcal{M}_i}{\mathcal{M}_{i+1}}\mathbf{r}'_{i+1} - \mathbf{r}'_{i+1} + \frac{\mathcal{M}_{i-1}}{\mathcal{M}_i}\mathbf{r}'_i$$

$$= \mathbf{r}'_0 + \frac{\mathcal{M}_{N-2}}{\mathcal{M}_{N-1}}\mathbf{r}'_{N-1} - \mathbf{r}'_{N-1} + \frac{\mathcal{M}_{N-3}}{\mathcal{M}_{N-2}}\mathbf{r}'_{N-2} - \mathbf{r}'_{N-2} + \dots \tag{A.198}$$

$$+\frac{\mathcal{M}_{i+1}}{\mathcal{M}_{i+2}}\mathbf{r}'_{i+2} - \mathbf{r}'_{i+2} + \frac{\mathcal{M}_i}{\mathcal{M}_{i+1}}\mathbf{r}'_{i+1} - \mathbf{r}'_{i+1} + \frac{\mathcal{M}_{i-1}}{\mathcal{M}_i}\mathbf{r}'_i$$

$$= \mathbf{r}'_0 + \frac{\mathcal{M}_{i-1}}{\mathcal{M}_i}\mathbf{r}'_i + \sum_{j=i+1}^{N-1}\left(\frac{\mathcal{M}_{j-1}}{\mathcal{M}_j} - 1\right)\mathbf{r}'_j.$$

Hence

$$\mathbf{r}_i = \mathbf{r}'_0 + \frac{\mathcal{M}_{i-1}}{\mathcal{M}_i}\mathbf{r}'_i - \sum_{j=i+1}^{N-1}\frac{m_j}{\mathcal{M}_j}\mathbf{r}'_j \quad (i \in [1, N-2]). \tag{A.199}$$

Setting $i = 1$ in (A.185),

$$\mathbf{r}'_1 = \mathbf{r}_1 - \frac{m_0}{\mathcal{M}_0}\mathbf{r}_0$$

$$= \mathbf{r}_1 - \mathbf{r}_0. \tag{A.200}$$

Substituting (A.199) with $i = 1$ into (A.200) and solving for $\mathbf{r}_0$,

$$\mathbf{r}_0 = \mathbf{r}'_0 + \frac{\mathcal{M}_0}{\mathcal{M}_1}\mathbf{r}'_1 - \mathbf{r}'_1 - \sum_{j=2}^{N-1}\frac{m_j}{\mathcal{M}_j}\mathbf{r}'_j$$

$$= \mathbf{r}_0' + \left(\frac{\mathcal{M}_0}{\mathcal{M}_1} - 1\right)\mathbf{r}_1' - \sum_{j=2}^{N-1} \frac{m_j}{\mathcal{M}_j}\mathbf{r}_j'$$

$$= \mathbf{r}_0' + \frac{m_0}{\mathcal{M}_1}\mathbf{r}_1' - \sum_{j=2}^{N-1} \frac{m_j}{\mathcal{M}_j}\mathbf{r}_j'.$$

Hence

$$\mathbf{r}_0 = \mathbf{r}_0' - \sum_{j=1}^{N-1} \frac{m_j}{\mathcal{M}_j}\mathbf{r}_j'. \tag{A.201}$$

The inverse Jacobi transformation for the positions is then

$$\mathbf{r}_0 = \mathbf{r}_0' - \sum_{j=1}^{N-1} \frac{m_j}{\mathcal{M}_j}\mathbf{r}_j' \tag{A.202}$$

$$\mathbf{r}_i = \mathbf{r}_0' + \frac{\mathcal{M}_{i-1}}{\mathcal{M}_i}\mathbf{r}_i' - \sum_{j=i+1}^{N-1} \frac{m_j}{\mathcal{M}_j}\mathbf{r}_j' \quad (i \in [1, N-2])$$

$$\mathbf{r}_{N-1} = \mathbf{r}_0' + \frac{\mathcal{M}_{N-2}}{\mathcal{M}_{N-1}}\mathbf{r}_{N-1}'.$$

Differentiating (A.202) and multiplying by the appropriate m_i, we obtain the inverse momentum transformation:

$$\mathbf{p}_0 = \frac{m_0}{m_0'}\mathbf{p}_0' - \sum_{j=1}^{N-1} \frac{m_0 m_j}{\mathcal{M}_j m_j'}\mathbf{p}_j' \tag{A.203}$$

$$\mathbf{p}_i = \frac{m_i}{m_0'}\mathbf{p}_0' + \frac{m_i \mathcal{M}_{i-1}}{m_i' \mathcal{M}_i}\mathbf{p}_i' - \sum_{j=i+1}^{N-1} \frac{m_i m_j}{\mathcal{M}_j m_j'}\mathbf{p}_j' \quad (i \in [1, N-2])$$

$$\mathbf{p}_{N-1} = \frac{m_{N-1}}{m_0'}\mathbf{p}_0' + \frac{m_{N-1} \mathcal{M}_{N-2}}{m_{N-1}' \mathcal{M}_{N-1}}\mathbf{p}_{N-1}'.$$

Using the inverse Jacobi transformations (A.202) and (A.203), the Hamiltonian is

$$H = \frac{p_0'^2}{2M} + \sum_{i=1}^{N-1} \frac{p_i'^2}{2m_i'} - \sum_{i=0}^{N-2} \sum_{j=i+1}^{N-1} \frac{Gm_i m_j}{|\mathbf{r}_i - \mathbf{r}_j|}, \tag{A.204}$$

where

$$m_0' = \mathcal{M}_{i-1} \tag{A.205}$$

$$m_i' = \frac{\mathcal{M}_{i-1}}{\mathcal{M}_i}m_i.$$

The Hamiltonian (A.204) can be written

$$H = \frac{p_0'^2}{2M} + \sum_{i=1}^{N-1} \left(\frac{p_i'^2}{2m_i'} - \frac{Gm_i m_0}{r_i'}\right) + \sum_{i=1}^{N-1} \frac{Gm_i m_0}{r_i'} - \sum_{i=0}^{N-2} \sum_{j=i+1}^{N-1} \frac{Gm_i m_j}{|\mathbf{r}_i - \mathbf{r}_j|}. \tag{A.206}$$

Neglecting the center-of-mass motion $p_0'^2/2M$ (in other words, assuming the center of mass is stationary), and choosing

$$H_0 = \sum_{i=1}^{N-1} \left(\frac{p_i'^2}{2m_i'} - \frac{Gm_i m_0}{r_i'} \right)$$ (A.207)

and

$$H' = \sum_{i=1}^{N-1} \frac{Gm_i m_0}{r_i'} - \sum_{i=0}^{N-2} \sum_{j=i+1}^{N-1} \frac{Gm_i m_j}{|\mathbf{r}_i - \mathbf{r}_j|},$$ (A.208)

the desired separation is obtained.

The unperturbed Hamiltonian is a sum of Kepler Hamiltonians, each of which can be written

$$H_0^{(i)} = \frac{p_i'^2}{2m_i'} - \frac{Gm_i' M_i'}{r_i'},$$ (A.209)

where $M_i' = (\mathcal{M}_i/\mathcal{M}_{i-1})m_0$. Therefore, evaluation of the unperturbed part of the problem for body i corresponds to evolving that body's Jacobi position $\mathbf{r}_i'$ and momentum $\mathbf{p}_i'$ along a segment of a Keplerian orbit about a central mass M_i'. This step involves the approximate solution of Kepler's equation, for which numerous procedures are given in the literature (see, for example, Danby (1992)).

The effect of the perturbation Hamiltonian H' is to change only the momentum:

$$\mathbf{p}_i'(t_0 + \Delta t) = \mathbf{p}_i'(t_0) - \nabla_{\mathbf{r}_i'} H'|_{t_0} \Delta t,$$ (A.210)

which is analogous to (A.172). Differentiating,

$$\mathbf{p}_i'(t_0 + \Delta t) = \mathbf{p}_i'(t_0) + \frac{Gm_i m_0}{r_i'^3}\mathbf{r}_i' + \sum_{j \neq i}^{N-1} \frac{Gm_i' m_j}{|\mathbf{r}_i - \mathbf{r}_j|^3}(\mathbf{r}_i - \mathbf{r}_j) - \frac{1}{\mathcal{M}_{i-1}} \sum_{j=0}^{i-1} \sum_{k \neq j}^{N-1} \frac{Gm_j m_k}{|\mathbf{r}_j - \mathbf{r}_k|^3}(\mathbf{r}_j - \mathbf{r}_k).$$

(A.211)

Referring to the map (A.179), a second-order mixed-variable symplectic integrator would be implemented as follows:

1) Perform a Jacobi transformation and evolve the $\mathbf{r}_i'$ and $\mathbf{p}_i'$ forward in time by $\Delta t/2$ on the Keplerian orbits corresponding to (A.209).

2) Compute the new the Jacobi momentum using (A.211). Note that an inverse Jacobi transformation is necessary to compute the appropriate $\mathbf{r}_i$.

3) Evolve the resulting coordinates forward in time another $\Delta t/2$ along the Keplerian orbits (A.209) using the new positions and momenta.

Because it is symplectic, this integrator can be used to investigate very long-term orbital evolution and because it exploits the nearly-Keplerian nature of the problem, it is quite fast.

APPENDIX B

LINEARIZED AMPLITUDE AND PHASE

In the linear theory of the Yarkovsky effect derived in Chapter 3, the amplitude and phase of the net diurnal and seasonal accelerations are given by the function

$$\left[\frac{k}{R}\Psi(z) - 4\epsilon\sigma T_0^3\right]^{-1}, \tag{B.212}$$

where

$$\Psi(z) \equiv z\frac{j_1'(z)}{j_1(z)} \tag{B.213}$$

and z is of the form $\alpha\sqrt{\pm i}$ with α real. Here I develop a representation of this function in terms of ordinary functions so that the amplitude and phase of those components may be explicitly evaluated.

First, consider $\Psi(z)$. Using the trigonometric forms of the spherical Bessel functions, we may write

$$\Psi(z) = z\left[\frac{\frac{\sin z}{z} + \frac{\cos z}{z^2} - \frac{\sin z}{z^3}}{\frac{\sin z}{z^2} - \frac{\cos z}{z}}\right] = \frac{(1 - z^2)\sin z + z\cos z}{z\cos z - \sin z}. \tag{B.214}$$

Since $\sqrt{\pm i} = (1 \pm i)/\sqrt{2}$, we define $x \equiv \alpha/\sqrt{2}$ so that $z = x(1 \pm i)$, remembering from Chapter 3 that we are only interested in the positive square root. Using the identities $\sin(\pm ix) = \pm i\sinh x$ and $\cos(\pm ix) = \cosh x$, we may write

$$\sin[x(1 \pm i)] = \sin x\cos(\pm ix) + \cos x\sin(\pm ix)$$

$$= \sin x\cosh x \pm i\cos x\sinh x$$

$$\cos[x(1 \pm i)] = \cos x\cos(\pm ix) - \sin x\sin(\pm ix)$$

$$= \cos x\cosh x \mp i\sin x\sinh x, \tag{B.215}$$

so that (B.214) may be rewritten

$$\Psi(z) = \frac{\mathcal{A} \pm i\mathcal{B}}{\mathcal{C} \pm i\mathcal{D}}, \qquad (\text{B.216})$$

where

$$\begin{aligned}
\mathcal{A} &\equiv 2x^2 \cos x \sinh x + \sin x \cosh x \\
\mathcal{B} &\equiv \cos x \sinh x - 2x^2 \sin x \cosh x \\
\mathcal{C} &\equiv \cos x \cosh x + \sin x \sinh x - \sin x \cosh x \\
\mathcal{D} &\equiv \cos x \cosh x - \sin x \sinh x - \cos x \sinh x.
\end{aligned}$$

$$(\text{B.217})$$

Therefore,

$$\left[\frac{k}{R}\Psi(z) - 4\epsilon\sigma T_0^3\right]^{-1} = \left[\frac{\frac{k}{R}(\mathcal{A} \pm i\mathcal{B}) - 4\epsilon\sigma T_0^3(\mathcal{C} \pm i\mathcal{D})}{\mathcal{C} \pm i\mathcal{D}}\right]^{-1} \equiv \frac{\mathcal{C} \pm i\mathcal{D}}{\mathcal{E} \pm i\mathcal{F}}, \quad (\text{B.218})$$

with

$$\begin{aligned}
\mathcal{E} &\equiv \frac{k}{R}\mathcal{A} - 4\epsilon\sigma T_0^3\mathcal{C} \\
\mathcal{F} &\equiv \frac{k}{R}\mathcal{B} - 4\epsilon\sigma T_0^3\mathcal{D}.
\end{aligned}$$

$$(\text{B.219})$$

Hence,

$$\left[\frac{k}{R}\Psi(z) - 4\epsilon\sigma T_0^3\right]^{-1} = \chi \pm i\psi = Ae^{\pm i\delta}, \qquad (\text{B.220})$$

where

$$\begin{aligned}
\chi &\equiv \frac{\mathcal{E}\mathcal{C} + \mathcal{F}\mathcal{D}}{\mathcal{E}^2 + \mathcal{F}^2} \\
\psi &\equiv \frac{\mathcal{E}\mathcal{D} - \mathcal{F}\mathcal{C}}{\mathcal{E}^2 + \mathcal{F}^2}
\end{aligned}$$

$$(\text{B.221})$$

and

$$\begin{aligned}
\delta &= \tan^{-1}\frac{\psi}{\chi} \\
A &= \sqrt{\chi^2 + \psi^2}.
\end{aligned}$$

$$(\text{B.222})$$
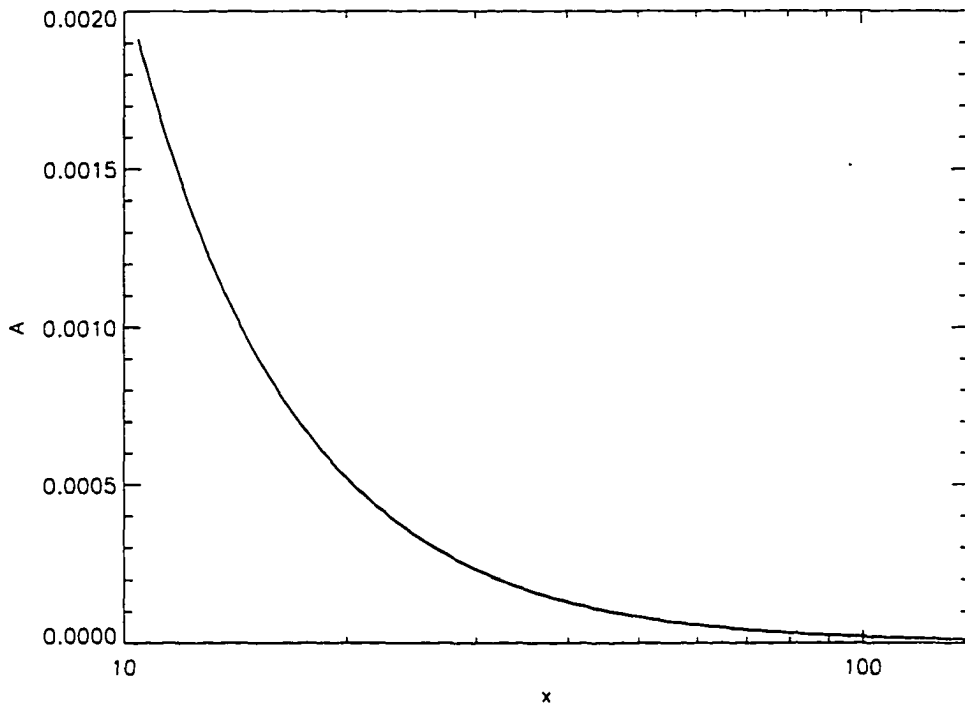
Figure B.33: Amplitude A as a function of x, demonstrating that the amplitude tends toward zero as x becomes large.

In Chapter 3, $\Psi(z)$ is evaluated with $x = r\sqrt{\omega/2\kappa}$, where ω is a either the orbital or the spin frequency. In that chapter, we are interested in the behavior of the amplitude A as the frequency ω becomes large. Fig. B.33 shows the behavior of A as a function of x. Evidently, $A \rightarrow 0$ as x, and therefore ω, become large.

APPENDIX C

DIURNAL EFFECT AT HIGH ECCENTRICITY

In Chapter 5, it was seen (Fig. 5.11) that, for large values of e, da/dt is quite large, and a steep function of e. There, I showed that this behavior is plausible on theoretical grounds, assuming that the function $|\langle B(r)/r \rangle|$ increases monotonically with e and increases more quickly with increasing e. Here I demonstrate that to be the case.

Because $r/a = (1 - e\cos E)$, the average of $B(r)/r$ over an orbit is given by

$$\left\langle \frac{B(r)}{r} \right\rangle = \frac{\psi \sin \delta}{2\pi a} \int_0^{2\pi} (1 - e\cos E)^{-7/2} \, dE, \qquad (C.223)$$

where E is the eccentric anomaly. $(1 - e\cos E)^{7/2}$ can be expanded in a Taylor series about $e = 0$:

$$(1 - e\cos E)^{-7/2} = 1 + \frac{7}{2}e\cos E + \frac{63}{8}e^2\cos^2 E + O(e^3). \qquad (C.224)$$

(C.224) is an infinite series in powers of $e\cos E$ in which all of the coefficients are positive. Substituting (C.224) into (C.223) and integrating,

$$\left\langle \frac{B(r)}{r} \right\rangle = \frac{\psi \sin \delta}{2\pi a} \left[2\pi + \frac{7}{2}e \int_0^{2\pi} \cos E \, dE + \frac{63}{8}e^2 \int_0^{2\pi} \cos^2 E \, dE + O(e^3) \right]. \qquad (C.225)$$

Since all of the coefficients in (C.225) are positive and

$$\int_0^{2\pi} \cos^n E \, dE = \begin{cases} 0 & : \ n \ \text{odd} \\ \text{a positive number} & : \ n \ \text{even}, \end{cases} \qquad (C.226)$$

$|\langle B(r)/r \rangle|$ is a monotically increasing function of e. As e is increased, higher powers of e become significant and since their coefficients are all positive, $|\langle B(r)/r \rangle|$

increases more rapidly with increasing e (this observation is confirmed by taking the second derivative of (C.225) with respect to e).

APPENDIX D

PROBLEMS WITH GAUSS' EQUATIONS

The finite difference calculation determines orbital element rates of change by averaging Gauss' perturbation equations over an orbit. Unfortunately, for certain orbits, this procedure fails. To understand why the procedure fails, consider Gauss' perturbation equations:

$$\frac{da}{dt} = \frac{2}{n\sqrt{1-e^2}}(F_r e \sin f + \mathcal{P}F_t/r) \tag{D.227}$$

$$\frac{de}{dt} = \frac{\sqrt{1-e^2}}{na}[F_r \sin f + F_t(\cos E + \cos f)] \tag{D.228}$$

$$\frac{di}{dt} = \frac{F_n r \cos u}{na^2\sqrt{1-e^2}} \tag{D.229}$$

$$\frac{d\varpi}{dt} = \frac{\sqrt{1-e^2}}{nae}[-F_r \cos f + F_t(1 + r/\mathcal{P})\sin f] + 2\frac{d\Omega}{dt}\sin^2\frac{i}{2} \tag{D.230}$$

$$\frac{d\Omega}{dt} = \frac{F_n r \sin u}{na^2\sqrt{1-e^2}\sin i}, \tag{D.231}$$

where F_r, F_t, and F_n are the radial, tangential, and normal components of the disturbing acceleration, r is the distance between the asteroid and the Sun, $u = \varpi - \Omega + f$, and $\mathcal{P} = a(1 - e^2)$. For the case $e = i = 0$, the perturbation equations become

$$\frac{da}{dt} = \frac{2}{n}F_t \tag{D.232}$$

$$\frac{de}{dt} = \frac{1}{na}[F_r \sin f + 2F_t \cos f] \tag{D.233}$$

$$\frac{di}{dt} = \frac{F_n r}{na^2}\cos u \tag{D.234}$$

$$\frac{d\varpi}{dt} = \text{undefined} \tag{D.235}$$

$$\frac{d\Omega}{dt} = \text{undefined.} \tag{D.236}$$

Obviously, the $d\varpi/dt$ and $d\Omega/dt$ equations are useless in this case. They reflect the problem that the node, apse, and true anomaly are not defined for $e = i = 0$.

Because of this problem, averaged de/dt values are invalid for cases with $e = 0$ and averaged di/dt values are invalid for cases with $i = 0$. To understand why this is true, consider applying a brief impulse to a body on a circular, uninclined orbit. Equation (D.233) actually gives the correct answer for the instantaneous eccentricity change provided one assumes that the kick occurred at periapse. In other words, the periapse direction, which was undefined before the impulse was applied, is defined after the impulse acts, hence the undefined rate of change in (D.235). Similarly, the node, which was undefined before the impulse occurred, is defined after the action of the impulse, passing through the point on the orbit at which the impulse is applied. By averaging such impulses over an entire orbit, the periapse and ascending node take on every possible value, violating the fundamental assumption in the averaging procedure – that all of the elements remain nearly constant during the averaging interval.

Indeed, (D.233) and (D.234) may yield invalid orbital averages even for cases with very small, but nonzero e or i because in those cases $d\varpi/dt$ and $d\Omega/dt$ are extremely sensitive to the perturbing forces. In other words, for cases with very small e or i, even small perturbing forces in (D.230) or (D.231) can cause $d\varpi/dt$ and $d\Omega/dt$ to be large during the averaging interval. Therefore, results for orbits with dangerously small e or i should be validated by verifying that the resulting changes in ϖ or Ω are small. For example, for cases in this dissertation with $e = 0.0001$, the largest changes in ϖ during an orbit where of order 10^{-5}.

The most straightforward way to avoid the above problems with the evaluation of de/dt and di/dt is to choose sufficiently large minimum values for e or i. This solution was sufficient for the investigation in Chapter 6, because asteroids with very small eccentricities are rare. A more elegant way to avoid those problems is to use a different set of variables. Instead of e and ϖ, one may use the eccentricity vector, whose components are $h = e \cos\varpi$ and $k = e \sin\varpi$ to avoid the

de/dt problem. Similarly, the inclination vector with components $p = i \cos \Omega$ and $q = i \sin \Omega$ can be used to avoid the di/dt problem. The equations for the rates of change of these new variables yield valid results even for cases with $e = i = 0$.

REFERENCES

Arnold, J. R. (1965). The origin of meteorites as small bodies: Ii. the model. *Astrophysical Journal* **141**, 1546-1547.

Asphaug, E. (1997). Impact origin of the Vesta family. *Meteoritics and Planetary Science* **32**, 965-980.

Bottke, W. F., D. P. Rubincam, and J. A. Burns (2000). Dynamical evolution of main belt meteoroids: numerical simulations incorporating planetary perturbations and Yarkovsky thermal forces. *Icarus* **145**, 301-331.

Bowring, S. A., D. H. Erwin, Y. G. Jin, M. W. Martin, K. Davidek, and W. Wang (1998). U/pb zircon geochronology and tempo of the end-permian mass extinction. *Science* **280**, 1039+.

Burns, J. A. and V. S. Safronov (1973). Asteroid nutation angles. *Mon. Not. Roy. Astron. Soc.* **165**, 403-411.

Burns, J. A. and I. Sharma (2000). Nutational damping revisited. In *AAS/Division of Planetary Sciences Meeting*, Volume 32, pp. 1301.

Chodas, P. W. (1999, September). Orbit uncertainties, keyholes, and collision probabilities. In *AAS/Division of Planetary Sciences Meeting*, Volume 31, pp. 2804+.

Danby, J. M. A. (1992). *Fundamentals of Celestial Mechanics* (2nd ed.). Willman-Bell, Inc.

Durda, D. D. and G. J. Flynn (1999). Experimental study of the impact disruption of a porous, inhomogeneous target. *Icarus* **142**, 46-55.

Efroimsky, M. and A. Lazarian (2000). Inelastic dissipation in wobbling asteroids and comets. *Mon. Not. Roy. Astron. Soc.* **311**, 269-278.

Erwin, D. H. (1994). The permo-triassic extinction. *Nature* **367**, 231+.

Farinella, P., R. Froeschlé, C. Froeschlé, R. Gonzi, A. Hahn, G. andMorbidelli, and G. B. Valsecchi (1994). Asteroids falling into the sun. *Nature* **371**, 314-315.

Farinella, P. and D. Vokrouhlický (1999, March). Semimajor axis mobility of asteroidal fragments. *Science* **283**, 1507-1510.

Farinella, P., D. Vokrouhlický, and W. K. Hartmann (1998, April). Meteorite delivery via yarkovsky orbital drift. *Icarus* **132**, 378-387.

Giorgini, J. D. (2001, June). Asteroid 1950 da: Long term prediction of its earth close approaches. In *Asteroids III Meeting*, pp. 205.

Gladman, B. J., F. Migliorini, A. Morbidelli, V. Zappala, P. Michel, A. Cellino, C. Froeschle, H. F. Levison, M. Bailey, and M. Duncan (1997). Dynamical lifetimes of objects injected into asteroid belt resonances. *Science* **277**, 197–201.

Goldstein, H. (1980). *Classical Mechanics* (2nd ed.). Addison Wesley.

Goldstein, R. M. (1969). Radar observation s of icarus. *Icarus* **10**, 430–431.

Greenberg, R. and C. R. Chapman (1983). Asteroids and meteorites: Parent bodies and delivered samples. *Icarus* **55**, 455–481.

Harris, A. W. (1979). Asteroid rotation rates II. A theory for the collisional evolution of rotation rates. *Icarus* **40**, 145–153.

Harris, A. W. (1994). Tumbling asteroids. *Icarus* **107**, 209–211.

Housen, K. R., L. L. Wilkening, C. R. Chapman, and R. J. Greenberg (1979). Asteroidal regoliths. *Icarus* **39**, 317–352.

Kring, D. A. (1993). The chicxulub impact event and possible causes of k/t boundary extinctions. In *First annual symposium of Fossils of Arizona*, pp. 63–79.

Langevin, Y. and M. Maurette (1980). A model for small body regolith evolution:the critical parameters. In *Lunar and Planetary Science Conference*, Volume 11, pp. 602–604.

Levison, H. and M. Duncan (1994). The long-term dynamical behavior of short-period comets. *Icarus* **108**, 18–36.

Linsky, J. L. (1973). The moon as a proposed radiometric standard for microwave and infrared observations of extended sources. *Astrophys. J. Supplement series* **25**(216), 163–204.

Marsden, B. G. (1999, September). Asteroid 1997 xf11 could collide with earth. In *AAS/Division of Dynamical Astronomy Meeting*, Volume 31, pp. 0702+.

Meninchella, M., P. Paolicchi, and P. Farinella (1996). The main belt as a source of near-Earth asteroids. *Earth, Moon, and Planets* **72**, 133–149.

Migliorini, F., P. Michel, A. Morbidelli, D. Nesvorný, and V. Zappalà (1998). Origin of multi-kilometer Earth- and Mars-crossing asteroids: quantitative simulation. *Science* **281**, 2022–2024.

Morbidelli, A. (1997). Chaotic diffusion and the origin of comets from the 2/3 resonance in the kuiper belt. *Icarus* **127**, 1–12.

Morbidelli, A. and B. Gladman (1998). Orbital and temporal distribution of

meteorites originating in the asteroid belt. *Meteoritics and Pl. Sci.* **33**, 999–1016.

Öpik, E. J. (1951). Collision probabilities with the planets and the distribution of interplanetary matter. *Proc. Roy. Irish Acad.* **54**, 165–199.

Ostro, S. J. (2001, June). Radar observations of asteroids: progress and perspectives. In *Asteroids III Meeting*, pp. 14.

Peterson, C. (1976, September). A source mechanism for meteorites controlled by the yarkovsky effect. *Icarus* **29**, 91–111.

Pravec, P., C. Hergenrother, R. Whitely, L. Sarounová, K. P., and M. Wolf (2000). Fast rotating asteroids 1999 TY2, 1999 SF10, and 1998 WB2. *Icarus* **147**, 477–486.

Radzievskii, V. V. (1952). A mechanism for the disintegration of asteroids and meteorites. *Astron. Zh.* **29**, 162–170.

Rubincam, D. P. (1987). Lageos orbit decay due to infrared radiation from earth. *JGR* **92**, 1287–1294.

Rubincam, D. P. (1995, January). Asteroid orbit evolution due to thermal drag. *JGR* **100**, 1585–1594.

Rubincam, D. P. (1998, January). Yarkovsky thermal drag on small asteroids and mars-earth delivery. *JGR* **103**, 1725+.

Rubincam, D. P. (2000). Radiative spin-up and spin-down of small asteroids. *Icarus* **148**, 2–11.

Saha, P. and S. Tremaine (1992). Symplectic integrators for solar system dynamics. *Astronomical Journal* **104**, 1633–1640.

Spencer, J., L. A. Lebofsky, and M. V. Sykes (1989). Systematic biases in radiometric diameter determinations. *Icarus* **78**, 337–354.

Uspensky, J. V. (1948). *The Theory of Equations* (1st ed.). McGraw-Hill.

Vokrouhlický, D. (1998). Diurnal Yarkovsky effect as a source of mobility of meter-sized asteroid fragments II. Non-sphericity effects. *Astron. Astrophys.* **338**, 353–363.

Vokrouhlický, D. (1999, April). A complete linear model for the yarkovsky thermal force on spherical asteroid fragments. Astron. Astroph. **344**, 362–366.

Vokrouhlický, D. and W. F. Bottke (2001). The yarkovsky force on small asteroids and their fragments. choosing the right albedo. submitted to Astron. Astroph.

Vokrouhlický, D. and M. Brož (1999, October). An improved model of the seasonal yarkovsky force for regolith-covered asteroid fragments. *AAP* **350**, 1079–1084.

Vokrouhlický, D. and P. Farinella (1998, October). The yarkovsky seasonal effect

on asteroidal fragments: A nonlinearized theory for the plane-parallel case. *AJ* **116**, 2032-2041.

Vokrouhlickỳ, D. and P. Farinella (1999). The yarkovsky seasonal effect on asteroidal fragments: A nonlinearized theory for spherical bodies. submitted to The Astronomical Journal.

Vokrouhlický, D., A. Milani, and S. Chesley (2000). Yarkovsky effect on small near-Earth asteroids: mathematical formulation and examples. *Icarus* **148**, 118-138.

Wetherill, G. W. (1988). Where do the apollo objects come from? *Icarus* **76**, 1-18.

Williams, J. G. (1969). *Secular perturbation in the solar system*. Ph. D. thesis, University of California, Los Angeles.

Wisdom, J. (1982). The origin of the kirkwood gaps: A mapping for asteroidal motion near the 3/1 commesurability. *Astronomical Journal* **87**, 577-593.

Wisdom, J. and M. Holman (1991). Symplectic maps for the n-body problem. *Astronomical Journal* **102**, 1528-1538.

Yoshida, H. (1993). Recent progress in theory and application of symplectic integrators. *Celestial Mechanics and Dynamical Astronomy* **56**, 27-43.

Zappalà, V., A. Cellino, B. J. Gladman, S. Manley, and F. Migliorini (1998). Asteroid showers on Earth after family breakup events. *Icarus* **134**, 176-179.